HIGH DIELECTRIC CONSTANT PVDF BASED NANOCOMPOSITES FOR APPLICATIONS IN LOW THERMAL EMISSIVITY AND FIELD EFFECT DEVICES

A THESIS SUBMITTED TO THE

UNIVERSITY OF PUNE

FOR THE DEGREE OF

DOCTOR OF PHILOSOPHY(Ph.D.)

IN

PHYSICS

BY

CHETAN V. CHANMAL

DR. (MRS.) JYOTI JOG
(RESEARCH GUIDE)

POLYMER SCIENCE AND ENGINEERING DIVISION
CSIR-NATIONAL CHEMICAL LABORATORY
PUNE - 411008 (INDIA)

July 2014

CERTIFICATE

This is to Certify that the work presented in the thesis entitled “**HIGH DIELECTRIC CONSTANT PVDF BASED NANOCOMPOSITES FOR APPLICATIONS IN LOW THERMAL EMISSIVITY AND FIELD EFFECT DEVICES**” by **Mr. Chetan V. Chanmal**, submitted for the degree **Doctor of Philosophy** in **Physics** was carried out under my supervision at the Polymer Science and Engineering Division, National Chemical Laboratory, Pune, 411008, India. Such material as has been obtained from other sources has been duly acknowledged in the thesis.

Dr. (Mrs.) Jyoti P. Jog
(Research Guide)

Date:

Place: NCL, Pune

DECLARATION

I hereby declare that the work presented in the thesis entitled “**HIGH DIELECTRIC CONSTANT PVDF BASED NANOCOMPOSITES FOR APPLICATIONS IN LOW THERMAL EMISSIVITY AND FIELD EFFECT DEVICES”,** submitted for Ph. D. Degree in Physics to the University of Pune, has been carried out under the supervision of Dr. (Mrs.) Jyoti P. Jog at the Polymer Science and Engineering Division, National Chemical Laboratory, Pune. The work is original and has not been submitted in part or in full by me for any degree or diploma to this or any other University.

Chetan V. Chanmal
(**Research Students)**

Date:

Place: NCL, Pune

Dedicated
To
My
Beloved
Family

Acknowledgements

During the course of my thesis work there were many people who were instrumental in helping me. I would like to thank all those people who made this thesis possible and an enjoyable experience for me.

My foremost thanks go to my research advisor Dr. Jyoti P. Jog for her support, guidance, encouragement and for allowing me freedom to pursue my interests and learn how to learn. Under her guidance I not only learned how to conduct research, but also how to communicate my ideas. I have learned a great deal from interacting with her.

I take this opportunity with deep sense of gratitude to record my sincere thanks to Dr. S. B. Ogale for his keen interest, valuable guidance during this work. His passion towards research, never lasting enthusiasm, and pursuit for high impact research has made deep impression on me.

I express my sincere thanks to Dr. S. Sivaram, former Director of National Chemical Laboratory (CSIR-NCL), Dr. Sourav Pal, Director, National Chemical Laboratory (CSIR-NCL) for giving me the opportunity to work in this prestigious research institute. I would like to thank Dr. M. G. Kulkarni, former Head, PSE Division and Dr. A. J. Verma, Head, PSE Division for their cooperation during the work of thesis. I would also like to thank the technical and non-technical staff of the Polymer Science and Engineering division for their help. Many thanks are also due to the staff members of Students Academic Office for their time-to-time help.

I greatly acknowledge the financial assistance from Council of Scientific and Industrial Research (CSIR) for providing a research fellowship for carrying out the doctoral work. I would also like to thank DRDO, Jodhpur for providing financial support.

I take this opportunity to thank Dr.S.I.Patil, Head, Department of Physics, University of Pune for his help in admission process. A special thanks to Prof. S.V. Bhoraskar and Dr. V.L.Mathe for their encouragement and fruitful scientific discussion. Thanks are due to Dr. N. B. Chaure for his help in FET studies.

I am very much thankful to Mr. Vivek Borkar whose help during this course was invaluable. I am thankful to all the staff members of NCL especially, Mr. A. B. Gaikwad (SEM facility), Mrs. Dhoble, Sunita Tombhare, Dr.S.D.Deshpande, and Dr. Harshavardhan Pol. My sincere thanks to Deenanath Bharati for his help.

My heartfelt thanks go to Prashant Patil and M. dhanalaxmi for your friendship and support in all ups and downs during this work. Without your help this work would not be possible. It was a memorable experience and I really enjoyed the time spent together.

I would also like to thank all lab members of JPJ group: Dr. Santosh Wanjale, Dr. Rajendra Kalgaonkar, Dr. Harshada Nagar, Dr. L. Priya, Amol Ridhore, Sachin Punde, Sachin, Usman, MSc. Project students Asha, and Remya for providing The wonderful working environment.

I had wonderful time to work with the members of SBO group, both past and present: Dr. Abhimanyu Rana, Dr. Prasad Yadav, Dr. Meenal Deo, Dr. Lily Mandal, Vishal, Deepti, Rounak, Dr. Parvez, Aniruddha, Anil, and Satish for their help during the work of the thesis.

I take this opportunity to thank Dr.S.K.Vadagbalkar, Principle, D.B.F. Dayanand College, Solapur, and Dr. R. N. Mulik, Head, Department of Physics, Dayanand College, Solapur for their whole-hearted help and constant support from the very first day in the college. Many thanks are due to teaching staff members of Physics department Dayanand College, Solapur: Prof. E.K.Kore, Prof. S.D. Chavan, and Dr.S.G.Pawar. Thanks are also due to the non-teaching staff members of Physics department.

I am grateful to the Jindam family for their support and encouragement during the work of the thesis.

I don’t have words to express my feelings towards my parents, their support and blessings have made me what I am today. Their patience and sacrifice will remain my inspiration throughout my life. The greatest thanks are to my wife, Nileema for being with me in all ups and down in this journey.

Chetan Chanmal

List of Nomenclature

PVDF	Poly (vinylidene) Fluoride
$BaTiO_3$	Barium titanate
MWCNT	Multiwalled Carbon Nanotube
XRD	X-ray Diffraction
DRS	Dielectric Relaxation Spectroscopy
SEM	Scanning Electron Microscopy
TEM	Transmission Electron Microscopy
DMA	Dynamic Mechanical Analysis
DSC	Differential Scanning Calorimetry
PLD	Pulsed Laser Deposition
IR	Infrared
ATR	Attenuated Total Internal Reflection
ITO	Indium Tin Oxide
I-V	Current Voltage
PVP	Poly (4-vinylphenol)
rpm	Revolution per minute

List of symbols

f	- *f*requency
$f_{\max}$	- frequency maximum in loss spectra
ω	- angular frequency
ε	- dielectric permittivity
ε'	- real Part of complex dielectric permittivity
ε''	- imaginary part of complex dielectric permittivity
$\tan \delta$	- dielectric loss tangent
M'	- real part of electric modulus spectra
M''	- imaginary part of electric modulus spectra
σ_{dc}	- dc conductivity
$\Delta\varepsilon$	- dielectric relaxation strength
α, β	- shape parameters describing the symmetric and asymmetric broadening of relaxation, respectively.
E_a	- activation energy
τ	- relaxation time
T	- temperature
Tc	- Curie temperature
MWS	- Maxwell-Wagner-Sillars relaxation
T_g	- glass transition temperature
α_c	- crystalline relaxation
α_a	- co-operative segmental relaxation
μ	- mobility
$I_{on/off}$	- on off current ratio
V_{DS}	- drain source voltage
V_{GS}	- gate source voltage

ABSTRACT

A study of polymer nanocomposites is an emerging area in polymer science where the property improvements are obtained by incorporation of nanofillers in the polymer matrix. There are three types of nanofillers, viz., nanoparticles having three dimensions in the nano scale, two-dimensional fillers like nano tubes, and nano clays with single dimension in the nano scale. Earlier, the research in this field was largely focused on the improvements in the mechanical, thermal and electrical properties of the polymer materials. Now, with the significant understanding of structure-property relations in polymer nanocomposites, research is driven to explore the potential applications of these materials in diverse fields like organic field effect transistors (OFET), photodetectors, sensors and light emitting diodes. It is in this context that the work presented in this thesis has been undertaken to investigate properties and applications of polymer nanocomposites based on Polyvinylidene Fluoride (PVDF) with three different types on nanofillers viz. Clay having one dimension in nanoscale, Carbon nanotubes (MWCNTs) having two dimensions in nanoscale and Barium Titanate ($BaTiO_3$) having three dimensions in the nanoscale. PVDF is chosen as the polymer matrix, as it is one of the important polymer because of its potential application as ferroelectric and pyroelectric material. These properties combined with high elasticity and processing ability provides a variety of technological applications of this polymer.

The main objective of the thesis was to explore the applications of polymer nanocomposites as an alternative material in organic field effect transistor devices and also to understand the effect of nanofiller on the structure and dielectric properties of PVDF. The polymer nanocomposite materials presented in this study are potentially useful as gate insulators and active channel layer in organic field-effect transistors.

Chapter 1 gives basic overview of polymer nanocomposites and properties of materials used in the thesis. This chapter also discusses the various applications of polymer nanocomposites relevant to the thesis.

Chapter 2 gives a general outline of the fabrication techniques used for polymer nanocomposites and basic theory of various techniques used for characterization of polymer nanocomposites.

Chapter 3 describes the effect of $BaTiO_3$ nanoparticles on the dielectric relaxation behavior of PVDF. Three dielectric relaxation processes were identified in PVDF/$BaTiO_3$ nanocomposites, viz. crystalline relaxation (α_c), glass transition relaxation (α_a) and Maxwell-Wagner-Sillars (MWS) relaxation. Further, the PVDF/$BaTiO_3$ nanofibers were prepared by electrospinning technique. The nanofibers show reduction in the thermal emissivity due to non woven porous morphology of the electrospun fiber.

In Chapter 4, we have discussed the interesting dielectric properties of PVDF/MWCNT thin film nanocomposites fabricated by Pulsed Laser Deposition (PLD) technique. The addition of MWCNT shows enhancement in the polar ferroelectric β phase of PVDF along with significant enhancement in the dielectric permittivity near the percolation threshold. We have also fabricated the organic field effect transistor (OFET) with PVDF/MWCNT nanocomposite thin layer as an active channel layer. The device shows strong field effect modulation in the drain current.

In Chapter 5, we discuss the fabrication organic field effect transistor using PVDF/Clay nanocomposites as a gate dielectric layer. The device exhibits excellent transistor performance with p-type of operation. The OFET also exhibits non-volatile memory and Infrared (heat) sensing applications due to the ferroelectric and pyroelectric properties of gate dielectric layer.

The **Chapter 6** summarizes the work described in this thesis by presenting the salient features of the work. Possible avenues for future investigations are also outlined.

Table of Contents

Chapter 1: Introduction and Literature Survey 1 - 30

Chapter 2: Materials and Experimental Techniques 31-56

Chapter 3: Dielectric Relaxation and Low Thermal Emissivity Studies of PVDF/BaTiO$_3$ Nanocomposites 57-85

Section I: Dielectric Relaxation Dynamics in PVDF/BaTiO$_3$ Nanocomposites

Section II: Electrospun PVDF/BaTiO$_3$ Nanofibers for Low Thermal Emissivity

---

Chapter 4: Strong Electric Field Modulation of Transport in PVDF/MWCNT Nanocomposite near the Percolation Threshold 86-111

Chapter 5: Nonvolatile Memory and Infrared (IR) Sensor based on PVDF/Clay Nanocomposites 112-136

Section I: Dielectric Studies of PVDF/Clay Nanocomposites

Section II: PVDF/Clay Nanocomposites as a Gate Dielectric in Organic FET

Chapter 1

Introduction and Literature Survey

This chapter provides the necessary background to the contents of the thesis, the motivation behind this work, as well as the objectives of this work. The overview of PVDF and its properties is also presented in this chapter. The various applications of nanocomposites relevant to thesis are described in this chapter.

1.1 Introduction

Advanced materials science is perhaps the most important field in the modern society catering the solutions for energy and environmental issues. In recent years significant progress has been achieved in understanding the basic principles which determine electric, magnetic and optical properties of the materials [1-3]. In last two decades, nanostructured materials such as polymer nanocomposites are receiving increased attention due to their wide spread potential applications. Polymeric materials reinforced by inorganic nanofillers are expected to exhibit improved mechanical behavior, aging resistance, flame retardancy, and thermal stability [4-7]. Therefore, understanding the unique properties of these materials is very important.

In this context, the work in this thesis was undertaken to prepare the nanocomposites of PVDF. Three different types of nanofillers having different dimensions in the nanoscale were used viz. Clay (1D), Multiwalled Carbon Nanotubes (MWCNT) (2D) and Barium Titanate $BaTiO_3$ (3D). This chapter also describes the necessary background of various applications of polymer nanocomposites relevant to the content of this thesis is provided.

1.2 Polymer Nanocomposites

Since the discovery of plastics in the first half of the twentieth century, many traditional materials (wood, steel, etc) are replaced by plastics due to their lightness, their processability, low density, good mechanical properties and other important properties like thermal, optical, electrical, etc. However, it was realized that the engineering application of polymers are often limited by major problems due to their low stiffness, low strength and low thermal stability. Therefore, a new technology needs to be developed which can answer new requirements, such as enhanced mechanical, thermal properties, reduced flammability etc.

This led to development of new field called polymer composites. By definition, a composite material is formed by the combination of different phases, which have distinct structural and chemical compositions, leading to a synergy of physical, chemical and/or mechanical properties compared to each component taken separately. Historically, micron sized fillers (talk, alumina, calcium carbonate…) were introduced to reinforce polymeric materials at reduced cost. From a practical point of view, this family of materials has been widely used in diverse areas including transportation, construction, electronics and consumer products [8-10]. Some examples of composites can be found in common applications, such as in the building trade (reinforcing concrete), flake jacket (Kevlar fibers), Carpentry (Plywood), Carbon and glass fibers are often used as reinforcing agents in aerospace and aviation applications [11-14].

The advent of nanotechnology has further provided impetus pushing for the development of materials with enhanced properties. Polymer nanocomposites represent a new class of materials based on reinforcement of polymeric materials using organo–inorganic nanofillers in which one of the components (filler) at least is in the nanometer scale. Polymer nanocomposites have attracted great interest, both in academia and industry, as they often exhibit remarkable improvement in the properties as compared to the pristine polymer or conventional micro-composites. In general, these improvements can include high modulus, high breakdown strength, heat resistance and flammability. These improvements in the properties are influenced by size, shape, dispersion and aspect ratio of nanofiller. In polymer nanocomposites, very small amount (5% by weight) of nanofiller inclusion is required to achieve the enhancement in the properties.

Nanoparticles are categorized in three groups. First one is the nanoparticles in which all three dimensions are in nano scale e.g., semiconductor, metal nanoparticles, etc [15, 16]. Second one is the two dimensional nanomaterials where in two dimensions of the filler are in nanoscale. Examples are nanotubes and cellulose whiskers that have the third dimension larger, forming elongated structures [17]. The third variety comprises of the nano clays, which are platelet shaped, with one dimension (thickness) in nanoscale. This family of nanocomposites can be called as the polymer/clay nanocomposites.

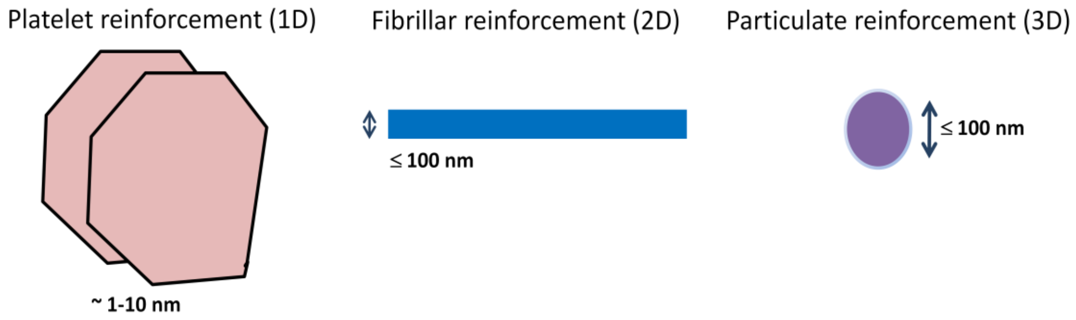

Figure 1.1: Schematic of Nanofillers having three different dimensions in nanoscale.

1.3 Poly (vinylidene Fluoride) (PVDF)

Polyvinylidene fluoride, abbreviated as PVDF or PVF$_2$, is a semi-crystalline polymer, which exhibits interesting physical and electrical properties depending on chain confirmations, crystalline form and molecular weight distribution [18, 19]. PVDF also shows excellent chemical properties, weather resistance, durability and biocompatibility [20-23]. Most importantly, PVDF possess ferroelectric, piezoelectric and pyroelectric properties [24-26]. These properties together are very useful for device applications such as transducers, medical diagnosis, electromechanical systems, nanogenerators and large scale integration of electronic circuits [27-29].

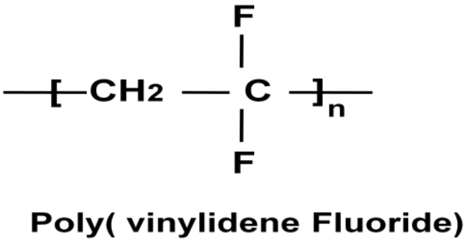

$$-\left[CH_2 - \overset{F}{\underset{F}{C}}\right]_n-$$

Figure 1.2: Molecular structure of PVDF.

Polymorphism in PVDF

The most fascinating characteristic of PVDF is its polymorphism. PVDF exhibits five crystalline forms, denoted by α, β, γ, δ, and ε depending on the fabrication processes and conditions. However, the phase that has aroused more technological interest, for providing the best pyro and piezoelectric properties, is the β phase. The α phase is thermodynamically more stable than β phase. Not surprisingly, extensive research in PVDF is driven to crystallization of PVDF from α phase into β phase.

The crystalline forms of PVDF can be grouped into two categories viz. polar and non-polar form. When polymer chain packing in the unit cell occur in such a way that the dipole attributed to each crystalline align parallel to one another a non-zero dipole moment results as in the case β, γ, and δ which are polar. On the other hand when polymer chains packing in the unit cell assume antiparallel alignment of molecular dipoles, net dipole moment becomes zero, as in the case of α and ε phase.

α phase is the most commonly obtained phase and is generally obtained from melt crystallization at temperature above 110 °C [30]. The chain conformation of this phase is trans-gauche-trans-minus gauche (TGTG') with t=179° and g=45° and anti parallel dipole moment. The unit cell consists of two monomeric units, forming an orthorhombic unit cell with lattice parameters, a= 0.496 nm, b= 0.964 nm and c= 0.462 nm [31, 32].The α phase can be obtained by solution crystallization from xylene/acetone mixture, monochloro benzene (MCB) and Dimethyl Formamide (DMF) [33].

The β phase has all trans configuration comprising fluorine atoms and hydrogen atoms on opposite sides of the polymer backbone This configuration gives net non-zero dipole moment which leads β phase to exhibit high piezoelectric constant and ferroelectric properties. The oriented β phase can be obtained from α phase by uniaxial or biaxial drawing of PVDF film at temperature 70 - 90 °C [34]. Drawing at temperature more than 120 °C results in oriented α phase. The α to β conversion varies as a function of temperature and maximum conversion is obtained at 90 °C [35]. The crystallization of PVDF from solution with dimethylformamide (DMF) or dimethylacetamide (DMA) may result α or β phase or mixture of these phases depending on temperature at which evaporation occurs. The unit cell of β phase of PVDF is orthorhombic and consists of two polymer chains with cell constants, a=0.858 nm, b=0.491 nm and c=0.256 nm [31]. The polymer chains possess a slightly deflected all trans conformation and parallel dipole moment.

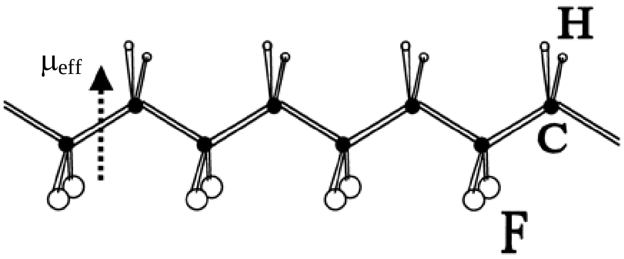

Figure 1.3: Stick diagram of all Trans TTTT (β) phase of PVDF.

γ phase is obtained by either melt crystallization or solution casting by crystallizing at a temperature near the melting temperature of α phase (T >160 °C). Lovinger suggested a monoclinic structure for this phase with cell constants, a=0.496 nm, b=0.967 nm and c=0.920 nm and β=93° [36]. γ phase has a chain conformation of TTTGTTTG' with parallel dipole moments [37].

Properties of PVDF

Crystallinity:

The commercial grade PVDF is about 40-50 % crystalline. The heat of fusion of 100 % crystalline PVDF is 25 Cal/g [38].

Thermal properties:

PVDF is thermally stable up to temperature 470 °C beyond which it degrades with pronounced loss of mass, nearly 60 %. The degradation is due to the emission of hydrogen fluoride along with a small amount of $C_4H_3F_3$. Above 600 °C a residual mass closer to 20 % is observed corresponding to the cross-linked material. The glass transition temperature is found to be about − 60 °C from dynamic mechanical analysis (DMA) and differential scanning calorimetry (DSC) experiments. The melting temperature of PVDF lies in the range of 160 °C to 180 °C depending on the type crystalline phase. The melting temperature is lower than the Curie temperature (T_c) of PVDF calculated in the range 205 to 208 °C. This indicates that heating the poled β PVDF films to temperatures lower than the melting temperature induces important conformational changes, but not a complete phase transition and thus not a complete depolarization of the polymer.

Piezoelectric properties:

Piezoelectric material is one which undergoes changes in electrical polarization in response to mechanical stress (or vice versa). This property can further extended to distinguish two important related properties i.e. pyroelectricity and ferroelectricity. In 1969, Kawai found high piezoelectric activity in polarized PVDF and many potential applications of PVDF were explored since then. PVDF exhibits by far strongest piezoelectric and pyroelectric property of all known polymers [39]. Moreover, piezoelectric polymer is considered superior over conventional piezoelectric ceramics as they offer ease of process and flexibility of polymer matrix. The acoustic impedance of piezoelectric polymer is low which matches closely with water, living tissue and other organic materials. Owing to their low acoustic impedance, they have been also used as materials for broadband energy convertors[40].

Ferroelectric properties:

Ferroelectric polymer thin films have great potential for applications in microelectromechanical systems and solid state electronic memories. The origin of ferroelectric properties in PVDF lies in the internal crystal structure imparting nonzero dipole moment due to high electronegative fluorine atom and orientation of crystalline dipole in the preferred direction. Polar PVDF (β, γ, δ phases) exhibits ferro-electric properties. The long-range order interaction of dipoles in the ferroelectric phase is extremely strong. Therefore, the Curie temperature (T_C) of 220 °C is higher than the melting point (T_m) [25].

Pyroelectric property:

Pyroelectricity in PVDF was first observed by Bergman et al. in 1971. PVDF is strong absorber of infrared energy in the wavelength region of 7-20 μm [41]. This wavelength region covers same wavelength region of human body. Therefore, PVDF makes natural choice of material useful in human motion sensor and pyroelectric sensor in sophisticated instruments like night vision cameras and laser beam profiling sensors.

Dielectric Property:

PVDF is known for its unique dielectric properties. The unique dielectric properties of PVDF based nanocomposites originates from the presence of highly electronegative fluorine on the polymer chains and the alignment of the C-F dipole in the direction of applied electric field. The dielectric permittivity of PVDF is close to 9 for non-polar α phase and around 10-12 for polar β phase. Several dielectric relaxations are seen in PVDF. The α_a relaxation, corresponding to the segmental motion in amorphous phase of PVDF, is observed at − 40 °C [42]. This peak maxima shifts towards lower frequency with decreasing temperature along with a broadening. The α_c-transition observed at approximately 80 °C of PVDF is due to the relaxation within the crystalline phase [43]. As temperature increases the magnitude of the loss peak increases and shifts to higher frequencies. This α_c relaxation is observed only in the case of α phase PVDF. Third relaxation is observed in the low frequency which is ascribed to the Maxwell-Wagner-Sillars (MWS) relaxation. The MWS relaxation is observed due to difference in the conductivity and permittivity values of the crystalline and amorphous phases.

Along with above mentioned properties, PVDF is known for its heat resistant, flame resistance and thermally stable engineering polymer. It is highly weather resistant, and is resistant to most of the chemicals.

1.4 Nanomaterials

Before discussing properties of nanocomposites, it is important to understand the advantages offered by nanofillers compared to large sized fillers. The first obvious difference between conventional composites materials and nanocomposites is the size of the filler. Nanoparticles are, by definition, particles with diameters below the micron dimension: generally, below 0.1 μm (100 nm). A more stringent definition considers nanoparticles as particles with properties depending directly on their size. Examples are optical, electrical, or magnetic properties. The reduced filler size leads to a large increase in their specific area and as a consequence this influences filler polymer interactions [44, 45]. Because of the very high values of specific surface area in nanomaterials, the relative number of molecules close to the surface is very high, which leads to significant variations of their electronic, optical, electro-magnetic and thermodynamic or mechanical properties and behavior [46-50]. In other words, the amount of nanofiller incorporated into polymer matrix is considerably lower compared to micron sized fillers to achieve the similar improvement of properties. Thus, the important advantage that these nanocomposites have is the various property enhancements are all achieved at very low filler content of ≤5 vol% [51, 52]. Hence, in most cases, clarity and polymer processability are unaffected.

Along with the individual properties of the host material and fillers, interfacial region shared by both the components affect properties of nanocomposites. Small size of nanoparticles provides large interfacial area between particles and host material. Other factors like aspect ratio of the nanoparticles, filler dispersion in the matrix, physical or chemical interaction of nanoparticles with host material also affect properties of nanocomposites [53, 54]. Good dispersion of nanoparticles in the polymer matrix is the key requirement for attaining superior properties in nanocomposites. The unique properties of nanocomposites are achieved by interfacial interaction between polymer and nanofillers. Poor nanofiller/polymer interfacial interactions lead to brittle materials. Thus, the key factor obtain performing composites is linked to the ability to finely disperse the nanoparticles and to take a maximum benefit of their large surface area through strong interfacial adhesion within the polymer matrix.

1.4.1 Clay

Clays are hydrous aluminum silicates and are generally classified as phyllosilicates. This consists of natural clays like montmorillonite, hectorite, and saponite as well as synthetic clays such as magadite, mica, laponite, flourohectorite, etc [55, 56]. Montmorillonite is the clay by far most commonly used in polymer layered silicate nanocomposite. Montmorillonite has a general formula (M^+y. n H_2O) (Al_{2-y} Mg_y) Si_4 O_{10} $(OH)_2$). M^+ is the exchangeable cation (monovalent ion) and nH_2O includes the interlayer water not specifically associated with ions. Crystal structure consists of layers made up of two tetrahedrally coordinated silicon atoms fused to an edge-shared octahedral sheet of either aluminum or magnesium hydroxide. The layer thickness is around 1 nm, and the lateral dimensions of these layers may vary from 30 nm to several microns or larger, depending on the particular layered silicate. When these high aspect ratio nanoparticles are dispersed in a polymer, they can be either, intercalated by the polymer chains, or, individually exfoliated within the polymer matrix. Stacking of the layers leads to a regular Van der Waals gap between the layers called the interlayer or gallery. Isomorphic substitutions within the layers (for e.g., Al^{3+} replaced by Mg^{2+} or Fe^{2+} replaced by Li^+) generate negative charges that are counterbalanced by alkali or alkaline earth cations located between the platelets or in the galleries as shown in figure 1.4. Chemical modification of clay is required for making it dispersible in polymer matrix. The properties of polymer/clay nanocomposites are governed by the level of dispersion of clay in the polymer matrix.

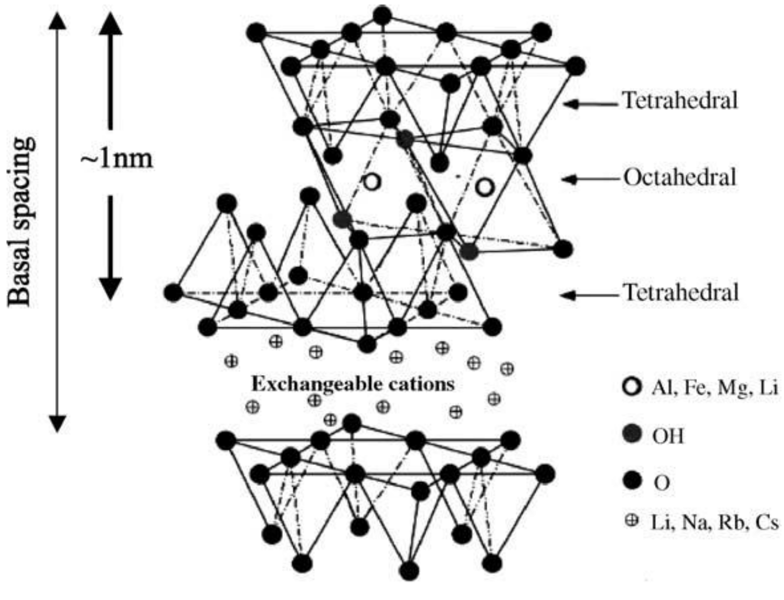

Figure 1.4: Structure of Montmorillonite clay [7].

1.4.2 Carbon nanotubes (CNT)

Carbon nanotubes (CNTs) were first reported by Ijima in 1991 [57], and the first polymer nanocomposite using CNTs as filler was reported in 1994 by Ajayan et. al [58]. Carbon nanotubes (CNTs) are broadly classified as single walled carbon nanotubes (SWCNT) and multi-walled carbon nanotubes (MWCNT). Carbon nanotubes can be thought of as graphitic sheets with a hexagonal lattice that have been wrapped up into a seamless cylinder. These layers are held together by Van der Waals force. The interlayer distance in multi-walled nanotubes is close to the distance between graphene layers in graphite, about 3.4 A°. MWCNTs have a unique combination of mechanical, electrical, and thermal properties that make them excellent candidates to substitute or complement conventional nano fillers in fabrication of multifunctional polymer nanocomposites [59-61]. Carbon nanotubes are either metallic or semiconducting depending on their diameter and the helicity of the arrangement of graphitic rings in their walls [62, 63]. CNTs are stronger than steel, lighter than Aluminum and more conductive than Copper. It has been shown by theoretical and experimental studies that CNT Young's modulus is greater than 1 TPa and they posses tensile strength up to 180 GPa [64]. The unique structure and properties of carbon nanotubes offer promising potential for developing novel, smart, and advanced materials. Owing to its properties, carbon nanotubes (CNTs) have been extensively investigated for their applications to various fields, including field-effect transistors (FETs), electron field emitters, and hydrogen storage [65-67]. The schematic of SWCNT and MWCNT is shown in figure 1.5.

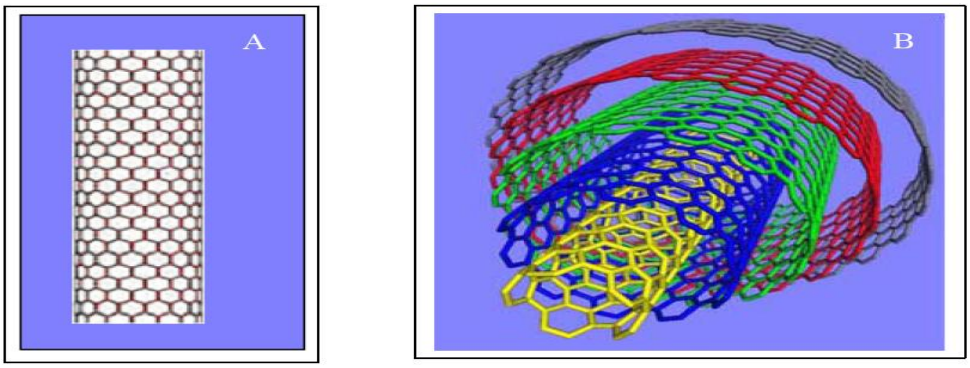

Figure 1.5: Schematic representation of (A) single walled and (B) multi walled carbon nanotubes.

1.4.3 Barium Titanate ($BaTiO_3$)

The ceramic Barium Titanate ($BaTiO_3$) is perhaps the most widely investigated oxide in the field of dielectrics. It has been attracted considerable interest for its wide variety of applications. The high dielectric constant of $BaTiO_3$ makes it suitable for applications like multilayer ceramic capacitors (MLCCs), dynamic random access ferroelectric memories (DRAMs), etc. $BaTiO_3$ also exhibits attractive piezoelectric properties useful for a large area of applications such as nonvolatile memories, surface acoustic wave devices, tunable capacitors, pyroelectric detectors, etc. However, major disadvantage of $BaTiO_3$ is the requirement of high temperature during its processing.

Barium titanate belongs to a group of materials that crystallize with the perovskite structure having the general composition of ABO_3. Barium titanate exists in the paraelectric cubic phase above its Curie temperature of about 130 °C, while in the temperature range of 0 °C to 130 °C, the ferroelectric tetragonal phase is stable [68]. The important dielectric properties of $BaTiO_3$ arise from a structural change where the center Ba^{2+} and Ti^{4+} cations are displaced relative to the O^{2-} ions, leading to the formation of electric dipoles (Figure 1.6). This leads to net dipole moment produced per unit volume for the dipoles pointing in a given direction.

$BaTiO_3$ nanoparticles are synthesized by using number of methods, such as, hydrothermal method, sol-gel processing, flame assisted spray pyrolysis (FASP), radio-frequency plasma chemical vapor deposition (RF-plasma CVD), and electrochemical route [69-73].

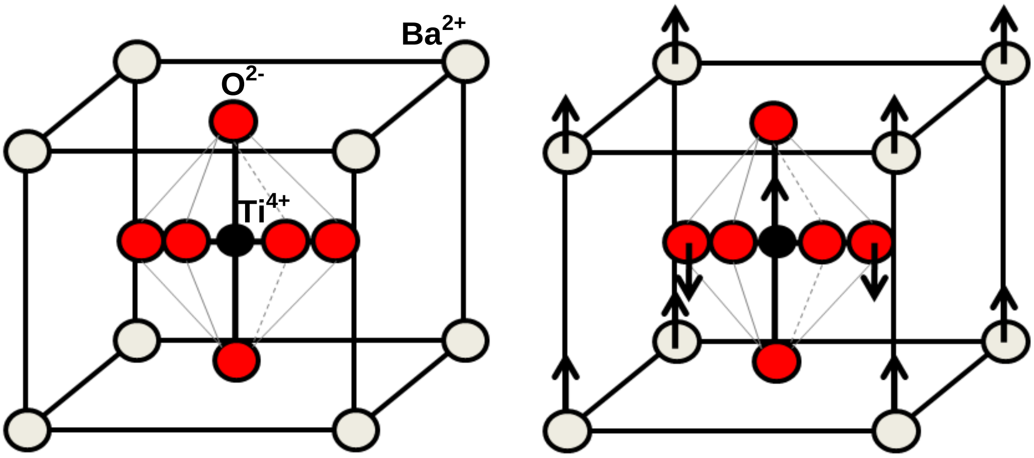

Figure 1.6: Crystal structure of $BaTiO_3$ above the Curie temperature is cubic (left) and below the Curie temperature is tetragonal (right).

1.5 PVDF based Nanocomposites

PVDF is studied with various nanofillers having different morphology and dimensions in nanoscale. The nanofillers addition to PVDF is used for variety of reasons: cost reduction, improved processing, thermal conductivity, electrical property, magnetic property and high dielectric material. For example fillers such as $FeCl_2$ and $MnCl_2$ are used to provide better electrical and magnetic properties [74]. Below we discuss some important nanocomposites systems based on PVDF.

As mentioned earlier, α phase can be easily obtained from melt crystallization and is more stable compared to β phase. Generally, it is difficult to obtain β phase PVDF film and many attempts were made to stabilize the β phase. In order to enhance the β phase content, which will provide the important properties of PVDF for various applications, making composites of PVDF with other organic or inorganic fillers was studied extensively. Nanocomposites of PVDF with organically modified silicates were shown to crystallize PVDF into β phase. Priya and Jog first reported the stabilization of β phase of PVDF in nanocomposites with the addition of clay [75, 76]. The thermal annealing studies indicated the stable β phase in these nanocomposites. The addition of clay also found to improve the mechanical properties of nanocomposites. Wu et al. studied nanocomposite of Poly (vinylidene fluoride) (PVDF) with graphene sheets (GSs) [77]. The structure-properties relationships of PVDF/GSs nanocomposites were studied using differential scanning calorimetry and X-ray diffraction. The addition of GSs to the PVDF matrix promotes α phase to β phase transformation of the polymer crystal. The nanocomposites also found to exhibit significant increases in mechanical properties and thermal stability compared to the neat PVDF. Addition of MWCNT to PVDF has demonstrated remarkable improvement properties, not only dielectric permittivity but also mechanical, thermal and piezoelectric properties [78]. In case of MWCNT based nanocomposites, dispersion of MWCNT is important factor which determines the final properties achieved in the nanocomposites. Hong et al. studied the piezoelectric properties of solution blended MWCNT and PVDF nanocomposites [79]. For drawn samples, the β phase content increased with increasing MWCNT loading. With the addition of poling process, pure β phase has been obtained at 0.2 wt% loading of MWCNT. The presence of MWCNT in PVDF matrix plays a role of nucleating agent for the crystallization of β phase PVDF and hence the enhancement in the properties. Levi et al., have shown that α to β conversion of PVDF occurs in solution blended PVDF/Carbon nanotube composites and the ratio between these two crystalline phases varies depending on the weight % of Carbon nanotubes [80]. The nanofillers $MgNO_3$ and $AgNO_3$ were used to promote α to β phase of PVDF and to increase the electric conduction in the nanocomposites [81]. In other work $CuCl_2$ based nanocomposites were used to promote the β phase in PVDF. Recently, electrospinning of PVDF nanofibers shows β phase formation [82]. The high voltage during electrospinning acts like poling filed to PVDF which helps in crystallization of β phase PVDF.

The electronic packaging industry requires thermally conductive but electrically insulating polymer composites. The composites of PVDF with aluminium nitride and silicon nitride were studied in this context. The highest thermal conductivity of 11.5 W/mK was obtained with PVDF and aluminium nitride [83].

Various nanofillers were added to PVDF to increase the dielectric permittivity of PVDF. Electroactive ceramics like lead zirconate titanate (PZT) and $BaTiO_3$ are useful for this purpose [84]. These ceramics possess very high dielectric permittivity at relatively low dielectric losses. However they have drawbacks like high temperature is required for synthesis, poor flexibility and not suitable for large area synthesis. PZT and $BaTiO_3$ were added to PVDF to get piezo and pyroelectric transducers. These composites are important in various applications as they combine important feature of individual components and their property can be tailored to various requirements. These nanocomposites are also useful in the development of sensors and actuators. The dielectric permittivity was also increased to high value in these nanocomposites. A three-phase composite with multi-walled carbon nanotubes (MWNTs) and $BaTiO_3$ particles embedded into Polyvinylidene fluoride was prepared by using a simple blending and hot-molding technique by Dang et al [85]. The results show that dielectric permittivity increases rapidly when the concentration of MWCNT is close to percolation threshold. In another alternative approach, semiconducting nanofillers were added into PVDF matrix to increase dielectric permittivity with low conductivity level. Nan et al. studied the Bi_2S loaded PVDF nanocomposites [86]. The preferential orientation of Bi_2S rods led to the anisotropic electric properties.

The ever increasing demand of energy from modern society is perhaps the greatest challenges that mankind will continue to face. Over the past decades intensive research efforts have been carried out in developing energy harvesting system. Several efforts were demonstrated for mechanical energy harvesting using PVDF based nanofibers membranes [87, 88]. Most of them were based on piezoelectric effect. Electrospun PVDF nanofibers were directly used as active layer to make mechanical to electrical energy conversion devices. The device was also useful for driving electronic device and shows long term stability. Piezoelectric PVDF is a good alternative material for fabricating flexible generators. Piezoelectric polymer nanofibers also offers better flexibility in comparison to the inorganic nanowires. Although PVDF has poorer piezo property than PZT, they offer unique advantage in fabrication of flexible nanogenerators [89]. The piezoelectric coefficients of ~ − 20 to 30 (d_{33}) and ~ 18 (d_{31}) pC/N are reported for β phase PVDF, which is sufficient to generate appreciable voltage under strain [90]. The biocompatibility of PVDF also allows to use in biological system for energy harvesting.

In recent year significant interest in molecular electronics and organic compounds based devices has taken place. Due to its ferroelectric properties, PVDF is one of the most promising candidates for applications in information storage medium among various non-volatile organic memories. The basic principle of operation in this device is bistable electric polarization of gate dielectric, which can be switched by an applied electric field [91]. The present motivation in OFET is driven to search for SiO_2 alternative which can significantly reduce the operating voltage [92]. Therefore, choice of gate dielectric material is important parameter to fully utilize applications of OFET. In this context, PVDF and its copolymers are extensively investigated as gate dielectric material in OFET architecture. These OFET showed mobility comparable to conventional silicon base FET and high on/off ratio.

Mhaisalkar et al. fabricated ferroelectric thin film transistor using Pentacene as semiconducting layer and P(VDF-TrFE) copolymer as gate insulator [93]. The transistor devices exhibited a generally observed clockwise hysteresis of drain current during the sweeping of gate voltage, which indicates the memory effects by dipole moment in P (VDF-TrFE) layer. They have also found positive turn on voltage shift up to +25 V when the gate bias was swept from ON to OFF state. This observed shift was attributed to the surface dipole field, trap states in semiconductor, and surface roughness due to high remnant dipolar polarization of P (VDF-TrFE). Cheomlin park et al. used spin coated β PVDF thin films to fabricate ferroelectric OFET [94]. The device shows a drain current bistablility of 100 μA at zero gate voltage with ±20 V gate voltage sweep. Ideal characteristics of a gate dielectric are that it should be solution processable at room temperature, flexible and should possess high dielectric constant. Feng Yan et al. fabricated solution processable low voltage OFET with high dielectric constant PVDF copolymer as relaxor ferroelectric [95]. The OFET shows carrier mobility greater that 0.1 $cm^2 V^{-1} s^{-1}$ at gate voltage of 3 V.

Functional materials can be directly integrated into OFET device to get several applications of OFET. Organic thin film transistors and ferroelectric polymer (polyvinylidene difluoride) sheet material are integrated to form various sensors for stress/strain, acoustic wave, and Infrared (heat) sensing applications [96]. Recent studies have demonstrated that direct integration functional materials into OFET device offers a unique way of realizing multimodal devices [97].

1.6 Applications of Polymer Nanocomposites

In the past decade polymer nanocomposite materials have been developed and its several potential applications were been explored in variety of fields including energy, sensor, transistors, etc. Figure 1.7 shows the important applications of nanocomposites in diverse fields.

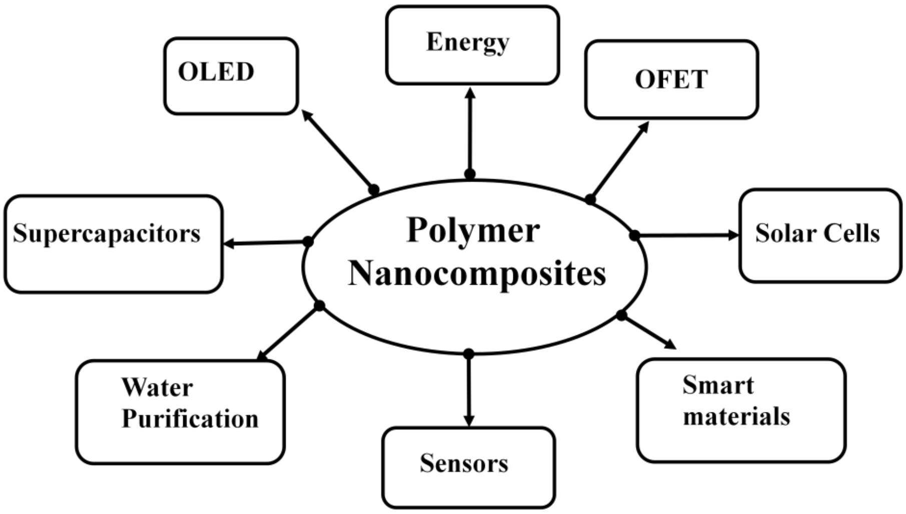

Figure 1.7: Overview of some of the potential applications of polymer nanocomposites.

1.6.1 High Dielectric Constant Materials

High energy storage capacitors with high efficiency plays very important role in the modern electric industry [98]. To achieve this materials with high permittivity and high breakdown strength are required, as the energy density of the material is proportional to the dielectric permittivity and the square of the applied field. Polymers are suitable choice for high energy density capacitors because of combination of high breakdown strength and low cost. However, polymers have relatively low dielectric constant (usually within the range of 2–10) and it is difficult for them to meet the capacitor requirements. On the other hand, ferroelectric ceramics have high dielectric constant but suffer from problem like high processing temperatures, brittle nature and large area synthesis. Currently, research interest is focused on the fabrication of high-dielectric constant polymer-based nanocomposites. Recently, nanocomposites of ceramic particles and polymer matrix are fabricated as means of engineering dielectric property and energy storage capacity [99]. The basic idea behind this approach is to integrate complementary properties of each constituent to get substantially enhanced energy density. The advantage of this method is that, although the breakdown strength of the polymer/ceramic composites is generally lower than that of pure polymers, the composites can withstand a relatively high electric field. Different polymer matrix are used in the nanocomposites are polyethylenes, poly (methyl methacrylate)s, epoxy resins, and polyimides. These polymers have typically low dielectric constant which significantly limits energy density obtained in the nanocomposites. Owing to its high dielectric constant, ferroelectric polymers like PVDF and its copolymer have been also used for the fabrication of high dielectric constant nanocomposites.

Another popular approach to increase the dielectric permittivity is to add conducting nanofiller to polymer matrix. Percolative systems consisting of insulating polymers and conductive fillers can show very high dielectric constants near the percolation threshold. Dramatic changes in the physical properties of composites occur when filler particles form a percolating network through the polymer matrix. So far, numerous percolative composites with high dielectric constants have been reported [100]. Typical conductive components include (i) carbon-based fillers such as carbon black, carbon nanotubes, carbon fiber, graphene, graphite platelets, (ii) metal-based fillers such as particles and nanowires [101].

The enhancement in the dielectric constant can well described by established percolation theory. According to percolation theory, the effective dielectric constant ε of a nanocomposites in percolative system is inversely proportional to the difference between the volume content of conductive fillers and the percolation threshold, f_c:

$$\varepsilon \propto (f_c - f)^{-s} \quad as\, f_c \leq f$$

According to above equation, a very high dielectric constant can be achieved if the composites contain an appropriate volume fraction of conductive filler.

Although a very high capacitance or dielectric constant can be realized, the nanocomposite material cannot withstand a high electric field because of the very high electrical conductivity of the fillers, resulting in some limitations for certain applications.

1.6.2 Organic Field Effect Transistor (OFET)

A field-effect transistor (FET) is a three terminal device where the drain source current (I_{DS}) is modulated and controlled by input voltage at drain electrode (V_{DS}) and gate electrode (V_{GS}). The metal insulator semiconductor (MIS) structure is fabricated respectively by gate electrode, gate dielectric and active semiconducting layer. By controlling the voltage on gate electrode (field effect), charges can be collected at the semiconductor dielectric interface. These charges are collected across the conducting channel due to field effect can then be drifted along the channel by applying a voltage at the drain terminal (V_{DS}). An FET is already referred to as being organic field effect transistor (OFET), in which the semiconducting layer is merely composed of organic molecules or polymers, although all components may be replaced by organic materials.

Unlike silicon based transistors, organic thin film transistors can be fabricated at room temperature and a variety of substrates can be used. The main difference between organic and inorganic device is that OFET works in accumulation mode, i.e. conduction mainly occurs in the ON state of device. Without a gate voltage being applied, no current flows between the source and drain electrode, the device is in OFF state. In the ON state, charge carriers are formed within few angstroms of the semiconductor dielectric interface when the gate voltage is applied. These charges are of same type of majority carriers in the semiconductor. Despite of this fundamental difference, the basic equations describing operation of device resembles those of inorganic FET and can be applied to organic FET.

Operating mode

Most OFETs reported in the literature so far exhibit either p-type or n-type behavior, meaning that the charge carriers are either holes or electrons respectively. p-type OFETs comprise the majority of these devices, showing the best transport properties and considerably more stable than n-type devices [102]. However, very recently, few groups [103, 104] have shown that ambipolar charge transport is also quite achievable and is a generic property of the organic semiconductors.

As stated earlier, the OFETs mainly works in accumulation mode. In hole transporting devices, a negative voltage is applied to the gate, inducing holes at the source electrode. These positive charge carriers will be injected into the semiconductor layer, provided that the hole injection barrier between the Fermi level of the metal and the highest occupied molecular orbital (HOMO) of the semiconductor is low. These accumulated holes form a conducting channel at the organic semiconductor/insulator interface. By applying a second negative bias to the drain (V_{DS}), the charges move along the channel and are collected at the drain.

OFETs are generally prepared in two configurations: The bottom-gate and the top - gate configuration as shown in Figure 1.8 (a). Bottom gate- top contact is favored over the top gate-bottom contact configuration because bottom contact has higher resistance, which reduces the output current due to poor growth of semiconductor on electrode surfaces. Also top contact device has larger contact area between the electrodes and the semiconductor which allows for more effective charge injection into the organic semiconductor. However, patterning of metal electrodes on top of semiconductor requires controlled metal evaporation in order to avoid damage of polymer film during deposition. Figure 1.8 (b) presents the schematic of device architecture in top contact geometry showing the channel width (W) and length (L).

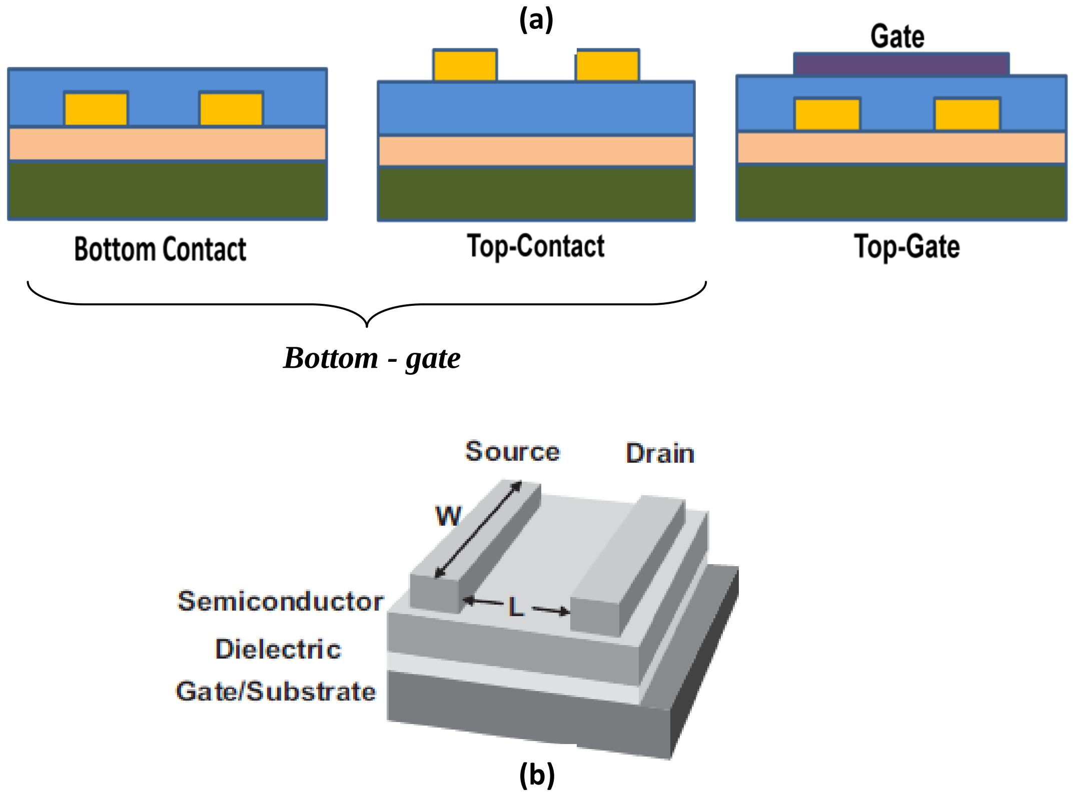

Figure 1.8: (a) Various structures of Organic Field effect transistor and (b) Schematic of OFET in bottom gate configuration showing channel width and length.

The operation of an OFET is defined by several parameters: the channel width (W) which is the width of the source-drain region, the channel length (L) defined as the spacing between the source and drain electrodes, the capacitance per unit area of the gate insulator (Ci), and charge mobility of the semiconductor. The channel length and width are limited by process technology, while capacitance and charge mobility are the materials property. Typical current–voltage (I-V) characteristics for OFET with Pentacene as a channel and SiO_2 as a gate dielectric are shown in Figures 1.9 (a) and 1.9 (b). The output characteristic shows variation of drain current, I_{DS} as a function of the source-drain voltage, V_{DS}, at fixed gate voltages, V_G. We can also plot I_{DS} versus V_G at a fixed drain source voltage. This is called transfer characteristics. The transfer curves give more information about the device such as its field-effect mobility (μ), threshold voltage (V_{th}), current on/off ratio (I_{on} / I_{off}) and subthreshold swing (S).

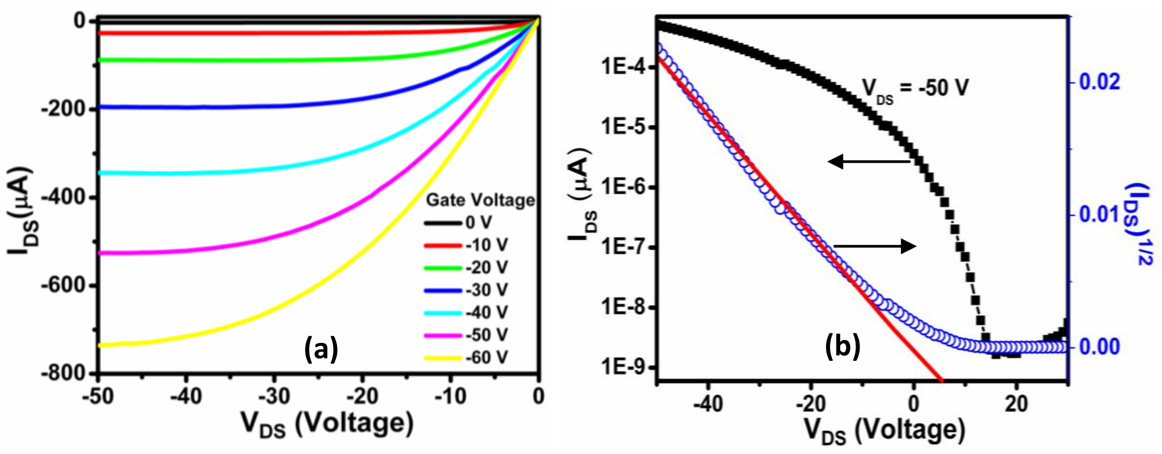

Figure 1.9: (a) Output and (b) transfer characteristics of Pentacene/SiO$_2$ OFET.

The output curves show the gate modulation of source–drain current (I_{DS}). According to the common model of OFETs, in the linear regime (at low V_{DS} ($< V_{GS} - V_{th}$)), μ (which has units of cm^2 V^{-1} s^{-1}) can be calculated from the following equation:

$$I_{DS} = \frac{W}{L}\, \mu\, C_i \left(V_{GS} - V_{th} - \frac{V_{DS}}{2}\right) V_{DS}$$

The value of μ of the OFETs in the saturation region (at high V_{DS} ($> V_{GS} - V_{th}$)) is given by:

$$I_{DS} = \frac{W}{2L}\, \mu\, C_i\, (V_{GS} - V_{th})^2$$

Where, C_i is the capacitance per unit area of the gate dielectric layer, and *L* and *W* are the channel length and width, respectively. From this equation, it is obvious that μ will be gate-voltage dependent, if the relationship between I_{DS} and V_G is nonlinear. Although it is expected that the linear regime and the saturation regime μ values to be similar for a device, this is not always the case. Source and drain contact resistances or high electric fields often affect the linear regime mobilities.

Transistor performance parameters

- On/Off ratio (I_{ON}/I_{OFF}): It is the ratio of the maximum current (I_{DS}) to the minimum current in the gate voltage sweep range at a certain V_{DS}. It represents the amplification factor by a transistor.
- Threshold Voltage (V_{th}): It is defined as minimum voltage at which the device turns ON i.e. the minimum voltage at which conductive channel is formed close to the dielectric/semiconductor interface, between the source and drain electrodes. V_{th} is determined by extrapolating I_{DS}-V_{GS} curve in linear region or $I_{DS}^{1/2}$ – V_{GS} curve in saturation region on V_{GS} axis to the intercept which gives V_{th}.
- Mobility (μ): This is a measure of how fast a charge carrier can move in response to electric field. It determines the maximum I_{DS} and operating frequency of the transistor.

Linear mobility: $$\mu_{lin} = \frac{L}{WC_iV_{DS}}\frac{\partial I_{DS}}{\partial V_{GS}}$$

Saturation mobility: $$\mu_{sat} = \frac{2L}{WC_i}\left(\frac{d\sqrt{I_{DS}}}{\partial V_{GS}}\right)^2$$

1.6.3 Thermal Emissivity

Advent of new technology led to the development of different technique for viewing the objects during night time and remote locations. Thermal imagers, night vision camera and forward looking infrared (FLIR) camera are mostly used in defense application for viewing objects, which extends the vision beyond the visible wavelength into the far infrared region. These all instrument work by tracing and detecting the infrared (heat radiant energy) radiation emitted by all objects. All objects above absolute zero emit thermal radiation. This radiation is proportional to the body temperature and the emissivity of objects. The radiation emitted from material surface at normal temperature lies in the IR region of the electromagnetic radiation (8-14 μm region). These radiation are detected by suitable thermal detector and image is formed by them are used in night viewing cameras. Thus, if the IR radiations from the object are suppressed by some means then such object becomes difficult to view by IR cameras. In defense, the concealment of important objects such as military equipments or vehicles from infrared detection is necessary for the protection from the enemies. Figure 1.10 shows the IR camera images of military vehicle. When coated with low thermal emissivity material the visibility of vehicle in IR camera significantly reduces.

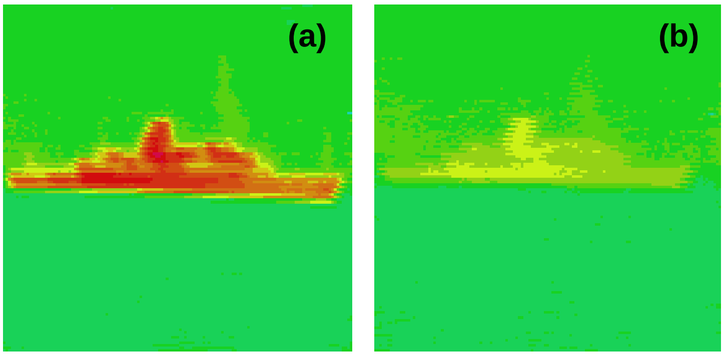

Figure 1.10: Camouflaging of military vehicles (a) without and (b) with low thermal emissive material coating.

In context to deceive and conceal an object, materials with low emissivity are often required. This technique of concealment of object through avoiding IR radiation is called Camouflaging. A thermal camouflage material is expected to possess a very low emissivity (0.5- 0.6), so that IR radiation emitted by an object coated with such a material will not be seen by the detector. As an example, this would permit a vehicle, or a person to blend into its surroundings, and become invisible to an infrared camera. Recently, it is predicted that nanoscale inorganic material embedded in suitable polymer matrix provides this property and therefore finds an application as a potential candidate for thermal camouflage material. Polymer nanocomposite films with low infrared emissivity present an attractive material choice for camouflaging technique and vast research is going in this direction. The interaction between the inorganic and organic compositions through physical force and chemical bond is important as a method for controlling the structure and properties of the inorganic-organic composite materials.

The reason why nanocomposites materials should have low emissivity can be understood from the basic origin of black body radiation in IR region. Basically, the vibrational modes of the atoms in the individual molecule are prime source emission of objects. And the vibrations in atoms increases with the increasing temperature. Each mode of vibration emits a characteristic frequency in the IR region of electromagnetic spectrum. This emission can be suppressed either by reducing the temperature or by reducing the extend of atomic vibrations. In nanocomposites, the incorporation of nanoparticles is expected to increase lattice constant or internuclear distance between the atoms and therefore reducing the force constant of vibrational modes [105]. This ultimately shifts the frequency of vibration into longer frequency region and hence reducing the thermal emissivity. Also, the understanding of thermal emissivity is important as it serves important intrinsic thermo physical property of material in the energy balance [106].

In recent years, application of functional nanomaterials for low emissivity application attracted extensive attention. The reduction in the emissivity value is made possible by the use of different types of functional nanofillers. Apart from high aspect ratio of these nanoparticles, their unusual physiochemical and optoelectronic properties have led to their useful application. Indium tin oxide (ITO), silicon based nanomaterials are commonly used materials for the low emissivity application. Especially, Collagen-g-PMMA/In_2O_3 nanocomposite found to exhibit lower infrared emissivity, however due its low decomposition temperature puts limit on the end use of this material. Some authors studied the use of $BaTiO_3$ for low emissivity application [107]. The incorporation of $BaTiO_3$ into silicon containing polyimide has found to affect the emissivity of nanocomposites. This decrease in emissivity was attributed to the presence of interfacial interaction between silicon containing polymer and $BaTiO_3$ nanoparticles.

1.7 Research Objectives

The primary objective of this thesis is to fabricate novel polymer nanocomposites based on PVDF using three different commercially available nanofillers viz. organically modified layered silicates , MWCNTs, and $BaTiO_3$. Three different techniques of were used to fabricate the polymer nanocomposites. Melt mixing technique is used for PVDF/$BaTiO_3$, pulsed laser deposition for PVDF/ MWCNT nanocomposites, spin coating is used for PVDF/Clay nanocomposites.

The specific objectives of this dissertation are:

- To fabricate nanocomposites based on PVDF and organo–inorganic nanofiller having various dimensions in nanoscale viz. MWCNTs, $BaTiO_3$ and clay.

- To study the effect of addition of nanofiller on the crystal structure of PVDF and dielectric properties of PVDF.
- To study the application of PVDF/$BaTiO_3$ nanocomposites for low thermal emissivity camouflaging material.
- To study the applications of PVDF/MWCNT nanocomposites as an active channel layer in field effect device.
- To fabricate OFET using PVDF/Clay nanocomposites as gate dielectric layer and to study the memory retention and IR sensing applications of OFET.

1.8. Structure of the Thesis

The entire research work is presented in six chapters.

Chapter 1 provides the importance of PVDF and its properties. A brief overview of polymer nanocomposites and their applications relevant to thesis are also discussed.

Chapter 2 describes various methods used for the fabrication of polymer nanocomposites. This chapter also includes details of basic theoretical background of various characterization techniques used for PVDF nanocomposites.

Chapter 3 presents fabrication of PVDF/$BaTiO_3$ nanocomposites by simple melt mixing technique. The effect of $BaTiO_3$ nanoparticles on the dielectric properties of PVDF is studied. Further, the fabrication of nanofibers by electrospinning and their potential application for camouflaging technique is also discussed.

Chapter 4 presents fabrication of thin films of PVDF/MWCNT nanocomposites by Pulsed Laser Deposition (PLD). The addition of MWCNT on the dielectric and conductivity properties were presented in this chapter. The use of PVDF/MWCNT nanocomposite as an active channel layer in OFET device is discussed.

Chapter 5 presents the dielectric properties of PVDF/Clay nanocomposites. The application of PVDF/clay nanocomposite as dielectric layer in OFET configuration is described. Further, the application of OFET as memory retention and IR sensing abilities is studied.

Chapter 6 summarizes the work described in this thesis by presenting the salient features of the work and also presents the possible avenues for future work

1.9 References

1. D.Y.Godovsky, *Advances in polymer sciences,* **2000**, 153, 165-204.
2. Rolf E. Hummel, *"Understanding Materials Science: History, Properties, Applications"*, Springer, 2nd ed. **2005**.
3. C. Velasco-Santos, A. L. Martinez-hernandez, V. M. Castano, *Composite Interfaces,* **2005**, 11, 567 – 586.
4. Hatsuo Ishida, Sandi Campbell, John Blackwell, *Chem. Mater.,* **2000**, 12, 1260-1267.
5. Philippe Dubois, Michaël Alexandre, *Advanced Engineering Mater.*, **2006**, 8,147-154.
6. D.R. Paul, L.M. Robeson, *Polymer,* **2008**, 49, 3187–3204.
7. Suprakas Sinha Ray, Masami Okamoto, *Prog. Polym. Sci.,* **2003**, 28, 1539–1641.
8. T. J. Pinnavaia, *Science,* **1983**, 220**,** 365-371.
9. A. Usuki, Y. Kojima, M. Kawasumi, A. Okada, Y. Fukushima, T. Kurauchi, O. Kamigatio, *J. Mater. Res.,* **1993**, 8, 1179.
10. K. Yano, A. Usuki, A. Okada, T. Kurauchi, O. Kamigatio, *J. Polym. Sci. Part A: Polym. Chem.,* **1993**, 31, 2493.
11. P. B. Messersmith, E. P. Giannelis, *Chem. Mater.,* **1994**, 6**,** 1719.
12. A. Okada, A. Usuki, *Mater. Sci. Eng.: C,* **1995**, 3, 109.
13. T. Lan, T. J. Pinnavaia, *Chem. Mater.,* **1994**, 6, 2216.
14. J. W. Gilman, *Appl. Clay. Sci.,* **1999**, 15, 31.
15. Del K. Strawhecker, E. Manias, *Chem. Mater.,* **2000**, 12, 2943.
16. H. Jeon, H. Jung, S. Lee, S. Hudson, *Polym. Bull.,* **1998**, 41, 107.
17. H. Choi, S. Kim, Y. Hyun, M. Jhon, *Macromol. Rapid Commun.,* **2001**, 22, 320.
18. Jr. R. Gregorio, E. M. Ueno, *Journal of Materials Science*, **1999**, 34, 4489-4500.
19. Jr. R. Gregorio, *Journal of Applied Polymer Science*, **2006**, 100, 3272-3279.
20. Y.Y. Zhang, S.L. Jiang, Y. Yu, G. Xiong, Q.F. Zhang, G.Z. Guang, *Journal of Applied Polymer Science*, **2011**,123, 2595-2600.
21. T. Umasankar Patro, Milind V. Mhalgi, D.V. Khakhar, Ashok Misra, *Polymer,* **2008**, 49 3486–3499.
22. N. Shukla, A. Shukla, A. K. Takhur, R N P Choudhary, *Indian journal of Engineering and Materials Sciences*, **2008**, 15, 126-132.

23. A. Tawansi, A. H. Oraby, S. I. Badr, I. S. Elashmawi, *Polym Int.,* **2004,** 53, 370–377.
24. M. A. Marcus, *Ferroelectrics*, **1982**, 40, 29.
25. A. J. Lovinger, *Ferroelectrics*, **1983**, 40, 227.
26. J. Kułek, I. Szafraniak, B. Hilczer, M. Połomska, *Journal of Non-Crystalline Solids*, **2007**, 353, 4448-4452.
27. Chengliang Sun, Jian Shi, Dylan J. Bayerl, Xudong Wang, *Energy Environ. Sci.,* **2011,** 4, 4508-4512.
28. Qi-Dan Ling, Der-Jang Liaw, Chunxiang Zhu, Daniel Siu-Hung Chan, En-Tang Kang, Koon-Gee Neoh, *Progress in Polymer Science,* **2008**, 33, 917–978.
29. A Kimoto, N Sugitani, *Meas. Sci. Technol.*, **2010**, 21, 075202.
30. Y. Takahashi, A. Tadokoro, *Macromolecules,* **1980**, 13, 1318.
31. M. A. Bachman, J.B. Lando, *Macromolecules*, **1981**, 14, 40.
32. L. Kutschabsk, E. Hohne, R. G. Kretschmer, *Acta polymerica*, **1991**, 43, 357.
33. R. Hasegawa, Y. Takahashi, Y. Chatani, H. Tadokoro, *Polymer Journal*, **1972**, 3, 600.
34. C. C. Hsu, P. H. Geil, *Journal of Material Science*, **1989**, 24, 1219.
35. P.Sajkiewicz, A. Wasiak, Z. Goclowski, *European polymer journal,* **1999**, 35, 423.
36. J. H. Wendroff, *Journal of Polymer Science: Polymer Letters*, **1980**, 18, 439.
37. A. J. Lovinger, *Journal of Polymer Science: Polymer Physics*, **1980**, 18, 793.
38. H. Nagawada, Y. Ishida, *Journal of Polymer Physics*, **1973**, 11, 2153.
39. J. Strathdee, W. H. Robinson, *Journal Applied Physics*, **1982**, 53, 605.
40. W. T. Chen, E. Sacher, D. H. Strope, J. J. Woods, *Journal of Macromolecular Science Part B:,***1982**, 21, 397.
41. Jacob Fraden, *Handbook of Modern Sensors Physics, Designs, and Applications*, Fourth edition, Springer, London, **2010**.
42. N. G. Mccrum, B. E. Read, G. William, *"Anelastic and dielectric effects in Polymeric solids",* John Wiley and sons, **1967**.
43. B. Hahn, J. Wendroff, D. Y. Yoon, *Macromolecules,* **1985**, 18,718.
44. Emil Roduner, *Chem. Soc. Rev.*, **2006**, 35, 583–592.
45. G. Cao, "*Nanostructures and Nanomaterials: Synthesis, Properties and Applications"*, Imperial College Press**, 2004**.

46. C. N. R. Rao, Achim Muller, Anthony K. Cheetham, "*The Chemistry of Nanomaterials*", John Wiley & Sons, **2006**.
47. A. P. Alivisatos, *Science,* **1996**, 271, 933 – 937.
48. Pavel Zrazhevskiy, Xiaohu Gao, *Nano Today,* **2009,** 4, 414 – 428.
49. Vivek Dhas, Subas Muduli, Wonjoo Lee, Sung-Hwan Han, Satishchandra Ogale, *Appl. Phys. Lett.* **2008**, 93, 243108.
50. Chris Binns, *"Introduction to Nanoscience and Nanotechnology",* Wiley, **2010**.
51. P. Walter, D. Mader, P. Reichert, R. Mülhaupt, *J. Macromol. Sci. Pure. Appl. Chem.* **36A 1999**, 1613.
52. L. E. Nielsen, Marcel Dekker, *"Mechanical Properties of Polymers and Composites",* New York, **1974**.
53. C.-W. Nan,Y. Shen, Jing Ma, *Annu. Rev. Mater. Res.,* **2010**, 40,131–151.
54. Michael E. Mackay, Anish Tuteja1, Phillip M. Duxbury, Craig J. Hawker, Brooke Van Horn, Zhibin Guan,Guanghui Chen, R. S. Krishnan, *Science,* **2006**, 311, 1740-1743.
55. Philippe Dubois, Michaël Alexandre, *Advanced Engineering Materials*, **2006**, 8, No. 3
56. E. Giannelis, R. Krishnamoorti, E. Manias, *Adv. Poly. Sci.*, **1999**, 138, 107.
57. S. Ijima, *Nature (London),* **1991**, 354, 56.
58. P. M. Ajayan, O. Stephan, C. Colliex, D. Trauth, *Science,* **1994**, 265, 1212.
59. Sandler J, Shaffer M, Prasse T, Bauhofer Q, Schulte K, Windle A, *Polymer,***1999**, 40, 5967.
60. P. M. Ajayan, *Chem. Rev.,* **1999,** 99, 1787-1799.
61. Inpil Kang , Yun Yeo Heung , Jay H. Kim , Jong Won Lee , Ramanand Gollapudi , Srinivas Subramaniam , Suhasini Narasimhadevara , Douglas Hurd , Goutham R. Kirikera , Vesselin Shanov , Mark J. Schulz , Donglu Shi , Jim Boerio , Shankar Mall , Marina Ruggles-Wren, *Composites: Part B,* **2006**, 37, 382–394.
62. Jeroen W. G. Wildoer, Liesbeth C. Venema, Andrew G. Rinzler, Richard E. Smalley, Cees Dekker, *Nature*, **1998**, 391, 59-62.
63. Sander J. Tans, Alwin R. M. Verschueren, Cees Dekker, *Nature*, **1998**, 393, 49-51.
64. T. Uchida, S. Kumar, *J. Appl. Polym. Sci.* **2005**, 98, 985.
65. Bachtold A, Hadley P, Nakanishi T, Dekker C. *Science*, **2001**, 294, 1317.

66. Lamari Darkrim F, Malbrunot P, Tartaglia G. *International Journal of Hydrogen Energy*, **2002**, 27, 193.
67. Zhu W, Kochanski G, Bower C, Zhou O, Kochanski G, Jin S. *Applied Physics Letters*, **1999**, 75, 873.
68. Peter Barber, Shiva Balasubramanian, Yogesh Anguchamy, Shushan Gong, Arief Wibowo, Hongsheng Gao, Harry J. Ploehn, Hans-Conrad zur Loye, *Materials*, **2009**, 2, 1697-1733.
69. I. J. Clark, T. Takeuchi, N. Ohtori, D. C. Sinclair, *J. Mater.Chem.*,**1999**, 9, 83.
70. M. H. Frey, D. A. Payne, *Phys. Rev. B,* **1996**, 54, 3158.
71. A. Purwanto, W. Wang, I. W. Lenggoro, K. Okuyama, *J. Europ. Ceram. Soc.* **2007**, 27, 4489.
72. K. Suzuki, K. Kijima, *J. Alloys and Comp.* **2006**, 319, 234.
73. J. Ta, *Mater. Res. Bull.* **2008**, 43, 639.
74. A. Tawansi, A. H. Oraby, E. Ahmed, E. M. Abdelrazek, M. Abdelaziz, *Journal Of Applied Polymer Science*, **1998**, 70, 1759.
75. L. Priya, J.P. Jog, *J. Polym. Sci. Polym. Phys.*, **2002**, 40, 1682.
76. L. Priya, J.P. Jog, *J. Polym. Sci. Polym. Phys.*, **2003**, 41, 31.
77. Liangke Wu, Alamusi, Junmin Xue, Takomi Itoi, Ning Hu, Yuan Li, Cheng Yan, Jianhui Qiu, Huiming Ning, Weifeng Yuan, Bin Gu, *Journal of Intelligent Material Systems and Structures*, **2014**,1-12.
78. Dan Chen, Min Wang, Wei-De Zhang, Tianxi Liu, *Journal of Applied Polymer Science*, **2009**, 113, 644–650.
79. Ji Seok Lee, Gwang Ho Kim, Woo Nyon Kim, Kyung Hwan Oh, Hyeong Tae Kim, Seung Sang Hwang, Soon Man Hong, *Mol. Cryst. Liq. Cryst.*, **2008**, 491, 247–254.
80. N. Levi, R. Czerw, S. Y. Xing, P. Lyer, D. L. Carroll, *Nano Lett.* **2004**, 4, 1267.
81. W. T. Chen, E. Sacher, D. H. Strope, J. J. Woods, *Journal of Macromolecular Science Part B: Physics, B21*, **1982**, 397.
82. Erika Simona Cozza, Orietta Monticelli, Enrico Marsano, Peggy Cebe, *Polym Int.,* **2013,** 62, 41–48.
83. Yunsheng Xu, D. D. L. Chung, C. Mroz, *Composites: Part A*, **2001**, 32, 1749-1757.
84. Mailadil T. Sebastian, Heli Jantunen, *Int. J. Appl. Ceram. Technol.*, **2010**, 7 , 415–434

85. Sheng-Hong Yao, Zhi-Min Dang, Mei-Juan Jiang, JinBo Bai, *Applied Physics Letters*, **2008,** 93, 182905.
86. Yang Shen, Ce-Wen Nan, Ming Li, *Chemical Physics Letters,* **2004**, 396, 420–423.
87. Jian Fang, Xungai Wang, Tong Lin, *J. Mater. Chem.*, **2011**, 21, 11088.
88. Chieh Chang, Van H. Tran, Junbo Wang, Yiin-Kuen Fuh, Liwei Lin, *Nano Lett.,* **2010**, 10, 726-731.
89. Bo zena Hilczer, Jan Kułek , Ewa Markiewicz , Marija Kosec, Barbara Mali, *Journal of Non-Crystalline Solids,* **2002**, 305, 167-173.
90. *"Piezoelectricity: Evolution and Future of a Technology"* By Walter Heywang, Karl Lubitz, Wolfram, *Springer.*
91. C.A. Nguyen, P.S. Lee, S.G. Mhaisalkar, *Organic Electronics*, **2007**, 8, 415–422.
92. Antonio Facchetti, Myung-Han Yoon, Tobin J Marks, *Adv. Mater.*, **2005**, 17, 1705-1725.
93. C.A. Nguyen, P.S. Lee, S.G. Mhaisalkar, *Organic Electronics*, **2007**, 8, 415-422.
94. Seok Ju Kang, Insung Bae, Ji-Hyuk Choi, Youn Jung Park, Pil Sung Jo, Yuna Kim, Kap Jin Kim, Jae-Min Myoung, Eunkyoung Kimb, Cheolmin Park, *J. Mater. Chem.*, **2011**, 21, 3619.
95. Jinhua Li, Zhenhua Sun, Feng Yan, *Adv. Mater.,* **2012**, 24, 88-93.
96. Yu-Jen Hsu, Zhang Jia, Ioannis Kymissis, *IEEE Transactions on Electron Devices*, **2011**, 58, 3.
97. Tran Quang Trung, Nguyen Thanh Tien, Young Gug Seol, Nae-Eung Lee, *Organic Electronics*, **2012**, 13, 533-540.
98. V. Tomer, E. Manias, C. A. Randall, *Journal of Applied Physics,* **2011**, 110, 044107.
99. Jin-Kai Yuan, Zhi-Min Dang, Sheng-Hong Yao, Jun-Wei Zha, Tao Zhou, Sheng-Tao Li, Jinbo Bai, *J. Mater. Chem.*, **2010**, 20, 2441-2447.
100. Cheng Huang, Qiming Zhang, *Adv. Func. Mater.,* **2004**, 14, 501.
101. C.W. Nan, Y. Shen, Jing Ma, *Annu. Rev. Mater. Res.,* **2010**, 40,131-151.
102. Yunlong Guo, Gui Yu,Yunqi Liu, *Adv. Mater.* **2010**, 22, 4427-4447.
103. Haibo Wang, Jun Wang, Xuanjun Yan, Jianwu Shi, Hongkun Tian, Yanhou Geng, Donghang Yana, *Applied Physics Letters*, **2006**, 88, 133508.

104. Hajime Nakanotani, Masayuki Yahiro, and Chihaya Adachi Koki Yano, *Applied Physics Letters,* **2007**, 90, 262104.
105. P.K. Biswas, A. De, N.C. Pramanika, P.K. Chakraborty, K. Ortner, V. Hock, S. Korder, *Materials Letters,* **2003**, 57, 2326-2332.
106. Laurent Ibos, Mario Marchetti, Abderrahim Boudenne, Stefan Datcu, Yves Candau, Jean Livet, *Meas. Sci. Technol.,* **2006**, 17, 2950-2956.
107. Baoping Lin, Hongjian Liu, Shixian Zhang, Chunwei Yuan, *Journal of Solid State Chemistry*, **2004**,177, 3849–3852.

Chapter 2

Materials & Experimental Techniques

This chapter presents details of various techniques used for preparation and characterization of polymer nanocomposites. The theoretical background of various techniques used for the fabrication and characterization of nanocomposites are also discussed.

2.1 Introduction

The thesis addresses the fabrication of PVDF based nanocomposites and their applications in field effect devices. Three different techniques such as melt compounding (bulk), pulsed laser deposition (thin film), and electrospinning (fiber) were used to fabricate the nanocomposites in bulk, thin film and nanofibers phase respectively. These techniques of fabrication are discussed in this chapter. The fabricated nanocomposites have been characterized for their microstructure by a host of techniques such as X–ray Diffraction (XRD), Transmission Electron Microscopy (TEM), and Scanning Electron Microscopy (SEM). Dielectric Relaxation Spectroscopy (DRS) was used to study the relaxation dynamics in polymer nanocomposites.

2.2 Materials

2.2.1 PVDF

PVDF grade SOLEF 1008, purchased from Solvay Belgium, is a low viscosity, all purpose injection-molding grade. It has excellent chemical resistance to most aggressive substances and solvents, excellent mechanical strength and toughness, high abrasion resistance, excellent aging resistance, resistance to UV and nuclear radiation, excellent intrinsic fire resistance, resistance to weathering, low permeability to most gases and liquids, and can easily be melt-processed by standard methods of molding and extrusion. The properties of PVDF (SOLEF 1008) as per company data sheet are as follows.

The average molecular weight is reported to be $\overline{M_w} = 119813$, $\overline{M_n} = 53909$.

Density: 1.78 g/cc,

Water Absorption: Max 0.04%

Melt flow: 24 g/10 min/5 Kg at 230 °C

Crystallinity: 48.9%

Coefficient of Thermal expansion (CTE), (linear 20 °C): 120-140 μm m^{-1} °C

Melting point: 174 °C

Crystallization temperature: 140 °C

2.2.2 Barium Titanate ($BaTiO_3$)

The Barium Titanate ($BaTiO_3$) nanoparticles used in this study were procured from Aldrich chemicals. The density of the nanoparticles is 6.08 gm/cc at 25 °C. Figure 2.1(a) shows the transmission electron microscopy (TEM) micrograph of $BaTiO_3$ clusters. The TEM micrograph shows that the nanoparticles has spherical and/or truncated cubic shape with average size nanoparticles around 30-50 nm. Figure 2.1 (b) presents Raman Spectra of $BaTiO_3$ nanoparticles. All the characteristic peaks corresponding to $BaTiO_3$ are seen in Raman spectra.

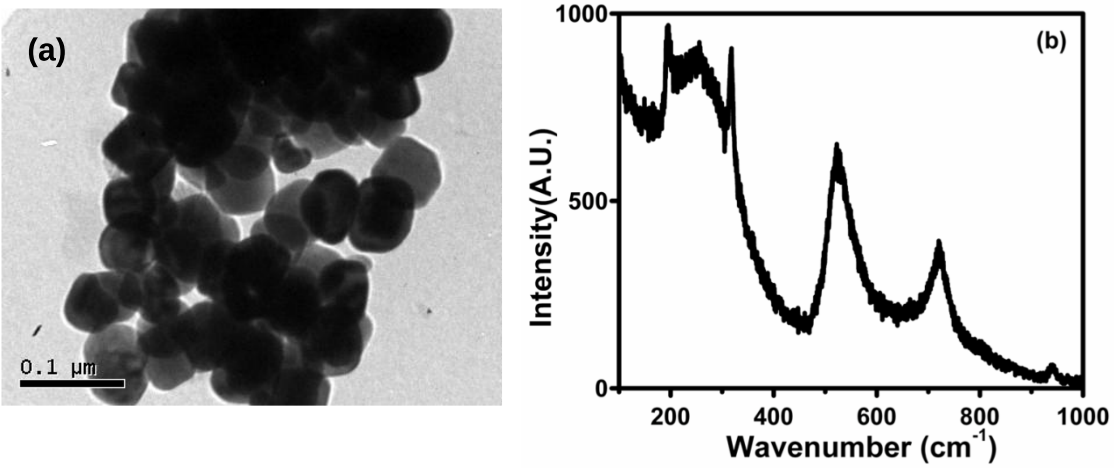

Figure 2.1: (a) HRTEM micrograph of $BaTiO_3$ nanoparticles (b) Raman spectra of $BaTiO_3$ nanoparticles.

The X-ray diffraction pattern for $BaTiO_3$ nanoparticles is shown in Figure 2.2. All the diffraction peaks can be indexed to cubic structure of $BaTiO_3$ and are in good agreement with the values reported [1]. The sharp XRD patterns indicate presence of highly crystalline nanoparticles.

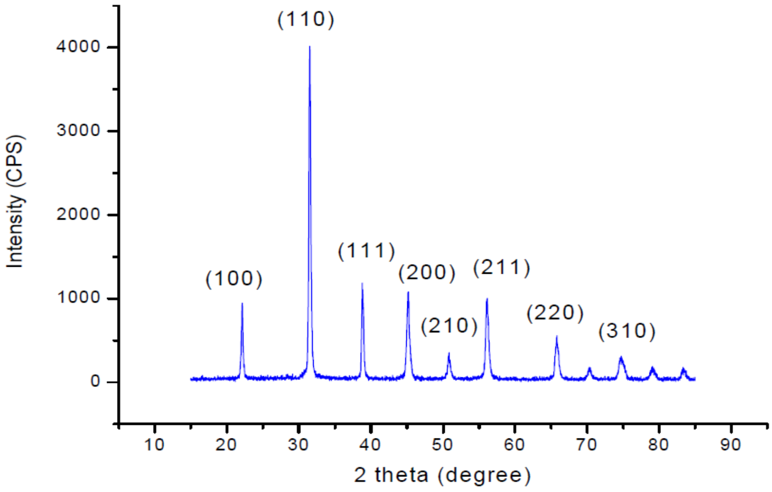

Figure 2.2: X-ray Diffraction (XRD) pattern of $BaTiO_3$.

2.2.3 Multiwalled Carbon Nanotubes (MWCNT)

Multiwalled carbon nanotubes procured from Aldrich, were used in this work. The properties of MWCNT as per the company data sheet are presented in the table 2.1.

Property	**Value**
Outer Diameter	10-20 nm
Inner Diameter	5-10 nm
Length	0.5-200 μm
Purity	95+%
Surface area (BET method)	40-600 m^2/g
Melting Point	3652–3697 °C
Density	2.1 g cm^{-3}

Table 2.1: Properties of MWCNTs used for nanocomposite fabrication.

Figure 2.3 (a) shows the X-ray diffraction pattern of MWCNT. A sharp peak at 2θ values of 26° (002), and other two peaks at 45° (101), 53° (004) are due to the ordered concentric cylinders of graphitic carbon [2]. Figure 2.3 (b) shows the transmission electron micrograph (TEM) of MWCNT. The diameter of MWCNTs varies between 20 to 50 nm and length is in few microns.

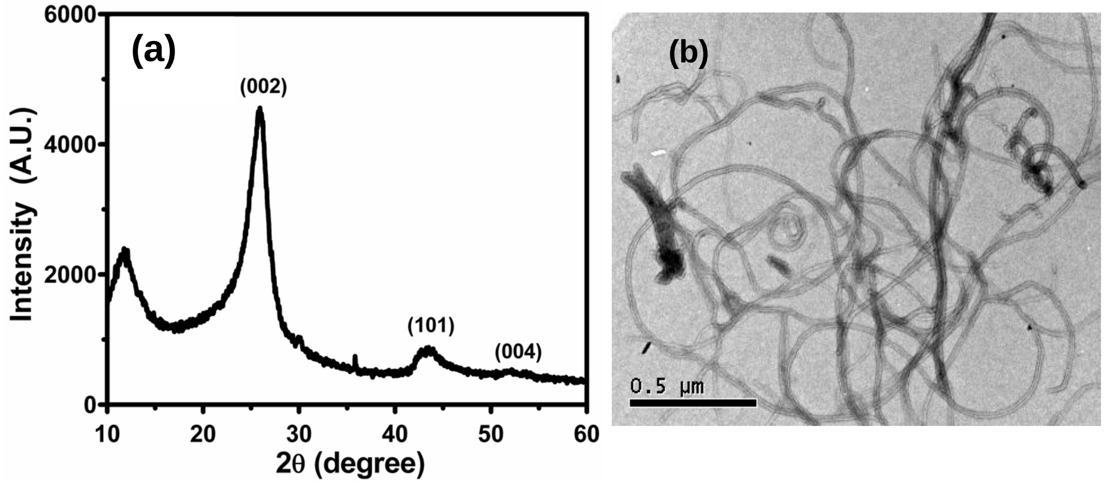

Figure 2.3: (a) X-ray diffraction pattern of MWCNT (b) Transmission Electron Micrograph (TEM) of as received MWCNT sample.

2.2.4 Clay

The clay used for this study is a organically modified clay, namely 20A generously supplied by Southern Clay Products (United States). The details of these organic modified clay is summarized in the table 2.2.

Clay Trade name	Organic Modifier	Modifier Conc. (meq /100g)	d spacing (nm)		% Weight loss		Specific Gravity (g/cc)
			Initial	After annealing at 200°C for 10 min	At ignition	At 200°C	
Cloisite 20A	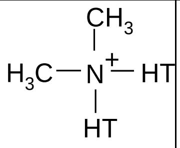 $H_3C-\overset{+}{N}(CH_3)(HT)-HT$ Anion- Cl^-	95	2.4	2.4	38	1	1.77

Table 2.2: Properties of organically modified Clay (HT represents Hydrogenated tallow).

The clay samples were used as received with no further purification steps. Thermal stability of the clay sample was ascertained by observing the d_{001} spacing after annealing at 200 °C for 5 min and observing percentage weight loss at 200 °C from thermo gravimetric (TGA) analysis. This data is shown in the table above. This was essential to ensure that the clay gallery does not collapse during the compounding step due to decomposition of organic content. The clay samples were dried at 60 °C overnight before compounding.

2.3 Fabrication of Nanocomposites

2.3.1 Melt Compounding Technique

The nanocomposites are prepared using melt compounding technique. A Haake Polylab batch mixer having 50 gm capacity is used for the compounding of nanocomposites of MWCNT and $BaTiO_3$ nanoparticles. The batch mixer is a Rheomix 600P equipped with roller rotors R600. The melt compounding is carried out at 200 °C for 5 min at a rotor speed of 60 rpm.

The films for different characterization were prepared by compression molding using Carver press model F-15181. An appropriate quantity of material is taken and heated above melting temperature between metal sheets, which are sprayed using mold release spray. Nominal pressure is applied to get the required thickness of the film. Platens of carver press are then cooled using water circulation. These films are used for further characterization.

2.3.2 Pulsed Laser Deposition (PLD)

Pulsed Laser Deposition is a physical vapor deposition method, carried out in a vacuum chamber. The experimental setup consists of a high energy laser source (generally an UV excimer laser like KrF (248 nm), ArF (193 nm) or Nd: YAG laser) and a vacuum chamber (capable of evacuating in the order of $\sim10^{-6}$ mbar with the help of rotary and turbo molecular pumps). The vacuum chamber is equipped with a rotating target holder (where multiple target mounting is possible for the multilayer deposition) controlled by a motor and a substrate holder, which can be simultaneously heated with the help of a heater controlled by a thermocouple. A gas inlet for inserting reacting gases, such as oxygen is also provided. The laser beam incident at an angle of 45° to the target surface is focused on to the rotating target (made up of the material to be deposited) with a quartz lens. Laser beam of energy ~100 to 400 mJ is focused to a size such that energy density is maintained between 1 to 5 J/cm^2, at the target. The deposition processes can be controlled by externally connected computer. For the deposition, at sufficiently high laser energy, the target material is ablated to form plasma plume. The plasma plume contains various excited atoms, molecules, ions and small particles. This plasma quickly expands away from the target towards the substrate where it is deposited at the surface of the heated substrate leading to growth of the desired thin film.

Figure 2.4: Pulsed Laser Deposition (PLD) unit at National Chemical Laboratory, Pune.

There are several parameters, which immensely influence the growth and properties of thin films [3-5]. These parameters are: laser energy density falling on the surface of the target, ambient pressure during and after deposition, pulse repetition rate, temperature of the substrate, choice and orientation of the substrate itself, target to substrate distance, etc. Laser energy density is a vital factor that hugely affects the properties of the films. The energy density must be selected and controlled according to the target material. If the target is made up of a soft material, such as a polymer, then the energy density should be kept low, so that the polymer chains won't break. While for a ceramic target material, it should be kept little high so that the material will be ablated. In all cases, care should be taken so that droplet-like particles should not get deposited on the substrate, due to very high energy density. The ambient oxygen partial pressure too is vital for the thin film growth of complex oxides to make up the loss of oxygen in the ceramic target itself or during the course of transfer of the excited species from the target to the substrate. The temperature is important to maintain the desired phase and stoichiometry of the film. In the present work, a KrF excimer laser (Lambda Physik, LPX200) having 248 nm wavelength and pulse duration of 20 ns was used for thin film deposition. The photograph of the PLD system is shown in figure 2.4.

2.3.3 Electrospinning

Electrospinning is a simple and versatile process by which polymer fibers with diameter ranging from few nanometers to several micrometers can be produced from a rich variety of materials that include polymers, composites and ceramics. The fibers produced possess extraordinary unique characteristics such as high surface area per unit mass coupled with remarkable high porosity, excellent structural mechanical properties [6, 7]. Electrospinning technique is found to be unique and cost effective route for fabricating fibers for a variety of applications. Choice of polymer solution and control on processing parameters provide a capacity of nanofibers produced with the range of diverse properties. The rheological properties of polymer solution or melt are enhanced, sometimes using external additives, to improve the efficiency of the electrospinning process.

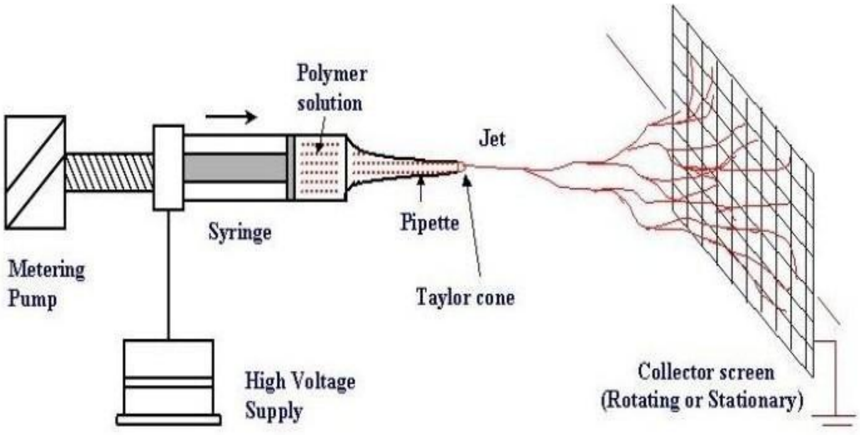

Figure 2.5: Schematic of electrospinning setup.

In a typical electrospinning process, a high electrical potential is applied between droplet of a polymer solution, or melt, held at the capillary tube and a grounded collector. When the applied electrostatic force overcomes the surface tension of the droplet, a charged jet of polymer solution is ejected. The route of the charged jet is controlled by electric field. The charged jet travels linearly for only a short distance before undergoing bending instability, resulting in the formation of looping trajectory of the jet. The electrospinning process is shown in figure 2.5.

Dependence of process parameters & solution parameters:

The following process variables and solution parameters affect the electrospinning process

- Spinning voltage- The spinning voltage is important in initial shape formation of droplet. The fiber size decreases with the increase in the applied spinning voltage, flow rate, concentration,
- Nozzle to collector distance- The structure and morphology of electrospun fibers is easily affected by the working distance because of its dependence on evaporation rate of solvent and deposition time.
- Polymer solution flow rate- The flow rate of solution through syringe important parameter, which control jet velocity and solution transfer rate. In general it is observed that with the increasing flow rate, fiber diameter is increased.

Polymer solution parameters like solution concentration and solution conductivity are important deciding factors in electrospinning process. At low viscosities ($\eta < 1$ Poise), surface tension is the dominant and influences fiber morphology and below a certain concentration droplets will be formed instead of fibers. At high concentrations ($\eta > 20$ Poise), processing will be prohibited by inability to control and maintain the flow of a polymer solution to the tip of the needle. Low concentration solution forms droplets due to influence of surface tension, while higher concentration prohibits fiber formation due to higher viscosity. Additives added to the solution control rheological properties of solution such as surface tension, electrical conductivity and dielectric constant. Figure 2.6 shows the diagram of potential applications of electrospun nanofibers.

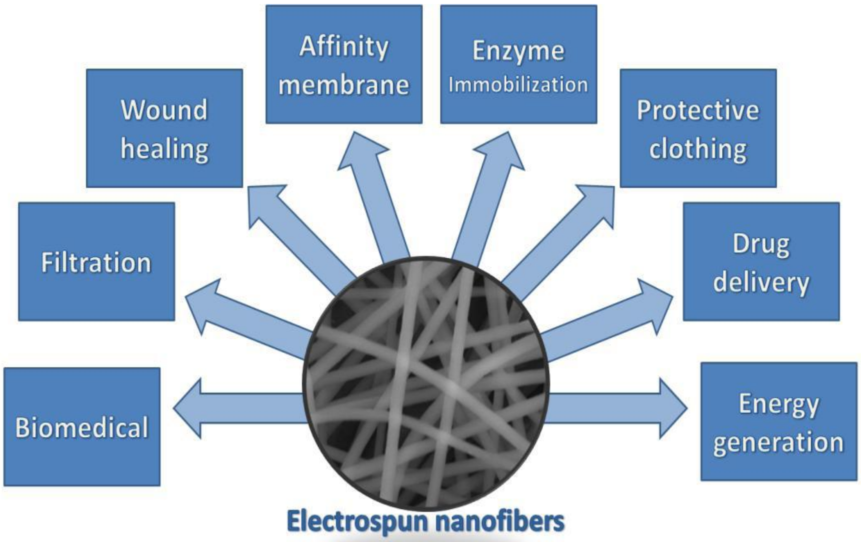

Figure 2.6: Applications of electrospun nanofibers.

2.3.4 Spin Coating

Spin coating is a widely used technique in the semiconductor industry for the deposition of polymer resist layers. A requirement for this technique is a good solubility of the polymer. Typical, spin coating procedure involves deposition of a small amount of a solution onto the centre of a substrate as shown in Figure 2.7, which is then spun around at a high speed so that the solution is spread out by the centrifugal force. The centrifugal force causes the excess solution to fly off the substrate and simultaneously, some of the solvent evaporates. The evaporation process raises the concentration and viscosity of the remaining solution. This high viscosity prevents the solution from exiting the substrate and a thin film of solution remains. Continued spinning evaporates the rest of the solvent after which a thin film of polymer is obtained. The spinning speed ranges from 1000 to 3500 rpm, depending on the interest of the film thickness. In a programmable spin coater, the solution is first spin coated at slower rate (of 100 rpm) so that the solution fully covers the substrate. Then a high speed is selected depending on the required film thickness. Final film thickness and other properties depend on the nature of the resin (viscosity, drying rate, percent solids, surface tension etc.) and the parameters chosen for the spin process. Factors such as final rotational speed, acceleration, and fume exhaust contribute to how the properties of coated films are defined.

Some variable process parameters involved in spin coating are:

- Solution viscosity
- Solid content
- Angular speed
- Spin Time

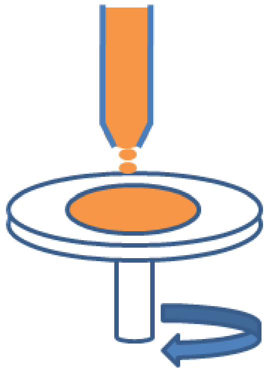

Figure 2.7: Illustration of Spin Coating.

2.4 Characterization Techniques

2.4.1 X-ray Diffraction (XRD)

X-ray diffraction (XRD) is a non–destructive analytical characterization technique for identification and quantitative determination of long–range order in various crystalline compounds [9, 10]. Crystal structure can be studied through diffraction pattern of waves that interact with atoms and have wavelength comparable with interatomic spacing in crystals. This technique is suitable for thin films, bulk and nanomaterials [11].

The basic components of the instrument are X - ray tube (X-ray generator), goniometer, detector, and the software. When fast moving electrons collide with the target atoms a continuous spectrum of X-ray is emitted known as Bremsstrahlung radiations. If the accelerating voltage is sufficient enough characteristic X-ray of target are produced. Copper and Molybdenum are commonly used targets that emit characteristic X - rays of wavelength 0.154 nm and 0.08 nm respectively. The energy of an X-ray photon is related to its wavelength λ and is given by [12]:

$$\varepsilon = h\nu = h\frac{c}{\lambda}$$

Where h is Planck's constant, ν is the frequency, c is the velocity of light, ε is energy of the photon and λ is the wavelength of X-ray source. Crystal studies require photon energies in the 10 to 50 KeV range.

The working principle of XRD can be understood from Bragg's law. Consider a collimated parallel beam of X-rays is incident on the sample as shown in figure 2.8. The diffracted beams are found when the reflections from parallel planes of the atoms interfere constructively. Let the parallel lattice planes in crystal are spaced at a distance d apart. Constructive interference of the irradiation from successive planes occurs when path difference is an integral multiple (n) of wavelength λ. Therefore,

$$2d\ \sin\theta = n\,\lambda$$

This is the Braggs law.

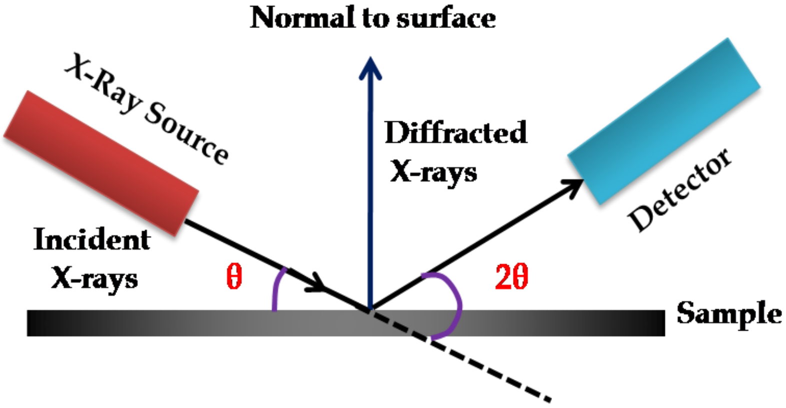

Figure 2.8: Representation of X-ray diffraction.

Although the reflection from each plane is specular, for only certain value of θ, the reflection from all parallel planes add up in phase to give strong reflected beam. The Bragg's law is a consequence of periodicity of the lattice. It requires that θ and λ to be matched. To achieve this it is necessary to scan either wavelength or angle. The condition for maximum intensity contained in Bragg's law above allow us to calculate details about the crystal structure, or if the crystal structure is known, to determine the wavelength of the X–rays incident upon the crystal. Experimentally, we use X-ray with known wavelength and take readings for different θ values to calculate the inter-planer spacing that satisfies Bragg's condition i.e. for peaks in XRD data.

In XRD a monochromatic beam of X-ray is incident on the sample at an angle of θ with the sample surface. The detector motion is coupled with the X-ray source in such a way that it always makes an angle 2θ with the incident direction of the X-ray beam. The resulting spectrum is a plot between the intensity recorded by the detector versus 2θ.

The crystalline forms of polymer and the structure of nanocomposites were evaluated by performing wide-angle X-ray Diffraction (WAXD) experiments using a Rigaku model Dmax 2500 X-ray diffractometer. The system consisted of a rotating anode X - ray generator operated at 40 kV and 100 mA with a wide-angle goniometer.

2.4.2 ATR-FTIR Spectroscopy

FTIR spectroscopy is known as finger print technique in materials characterization. Infrared spectrum appears only when the vibrations amongst bonded atoms produces a change in the permanent electric dipole moment [13, 14].

FTIR spectrophotometer consists of interferometer, infrared light source, an infrared detector, and beam splitter. Michelson interferometer is used in FTIR instruments. A parallel beam of radiation is directed from the source to the interferometer, consisting of the beam splitter B and two mirrors, M_1 and M_2. The beam splitter is a plate of suitably transparent material (e.g. KBr) so as to reflect just 50% of the radiation falling on it. Thus half the radiation goes to M_1, and half to M_2, returns from both these mirrors along the same path, and is then recombined to a single beam at the beam splitter. The recombined beam leaving B shows constructive or destructive interference, depending on the relative path lengths B to M_1 and B to M_2. Thus if the path lengths are identical or differ by integral multiple of wavelengths, constructive interference gives bright beam leaving B, whereas if the difference is a half integral number of wavelengths, the beam cancels at B. As the mirror M_2 is moved smoothly away or towards from B, therefore, a detector sees radiation alternating in intensity. It is fairly easy to imagine that if the source emits two separate monochromatic frequencies, υ_1 and υ_2 then interference pattern of υ_1 and υ_2 would overlay the interference caused by M_1 and M_2; the detector would see a more complicated intensity fluctuation as M_2 is moved, but computing the Fourier transform of the resultant signal is very rapid way of obtaining the original frequencies and intensities emitted by the source. Taking the process further, even white radiations emitted by the source produces an interference pattern which can be transformed back to the original frequency distribution.

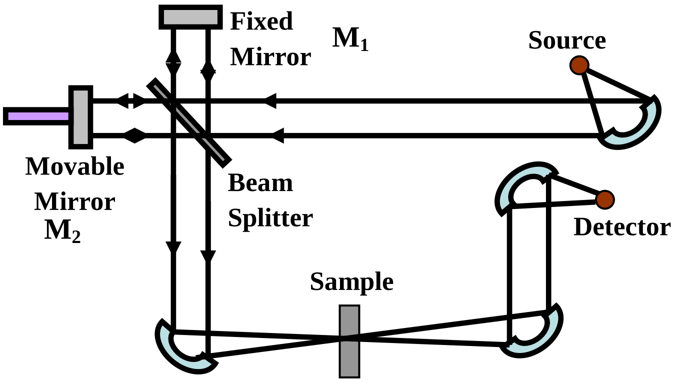

Figure 2.9: Schematic of FTIR Spectrophotometer

Attenuated total reflectance (ATR) is a sampling technique used in conjunction with infrared spectroscopy which enables samples to be examined directly in the solid or liquid state without further preparation. Light undergoes multiple internal reflections in the crystal of high refractive index, shown in blue. The sample is in contact with the crystal.

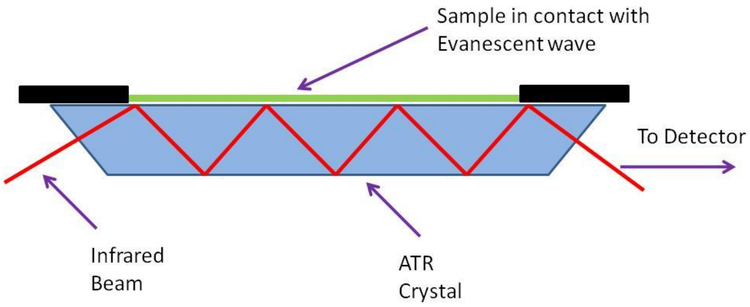

Figure 2.10: Schematic of working of ATR-FTIR spectroscopy.

ATR uses a property of total internal reflection resulting in an evanescent wave. A beam of infrared light is passed through the crystal of high refractive index such as ZnSe. Radiation from source enters the crystal where it undergoes series of total internal reflections before exiting crystal. This reflection forms the evanescent wave which extends into the sample. The penetration depth into the sample is typically between 0.5 and 2 micrometers, with the exact value being determined by the wavelength of light, the angle of incidence and the indices of refraction for the ATR crystal and the medium being probed. The beam is then collected by a detector as it exits the crystal. This evanescent effect only works if the crystal is made of an optical material with a higher refractive index than the sample being studied. In the case of a solid sample, it is pressed into direct contact with the crystal. The result is a selective attenuation of the radiation at those wavelengths at which the sample absorbs. Because the evanescent wave into the solid sample is improved with a more intimate contact, solid samples are usually firmly clamped against the ATR crystal, so that trapped air is not the medium through which the evanescent wave travels, as that would distort the results.

ATR-IR data presented in the thesis were taken from Perkin-Elmer FTIR Spectrum one spectrophotometer operated at a resolution of 4 cm^{-1}. Ten spectra were recorded for averaging.

2.4.3 Raman Spectroscopy

When a beam of monochromatic radiation is passed through a transparent substance, the radiation energy is scattered. If the scattered energy will consist almost entirely of radiation of the incident frequency then it is so-called *Rayleigh scattering* but, in addition, certain discrete frequencies above and below that of the incident beam will be scattered, it is referred to as Raman scattering [13].

According to quantum theory of radiation, when photons having energy ‘hυ’ undergo collisions with molecules and, if the collision is perfectly elastic, they will be deflected unchanged. A detector placed to collect energy at right angles to an incident beam will thus receive photons of energy ‘hυ’, i.e. radiation of frequency ‘υ’. However, it may happen that energy is exchanged between photon and molecule during the collision: such collisions are ‘inelastic’. The molecule can gain or lose amounts of energy only in accordance with the quantum laws; i.e. its energy change, ΔE joules, must be the difference in energy between two of its allowed states. Thus, ΔE must represent a change in the vibrational and/or rotational energy of the molecule. If the molecule gains energy ΔE, the photon will be scattered with the energy $(h\upsilon - \Delta E)$ and the equivalent radiation will have a frequency $(\upsilon - \Delta E/h)$. Conversely, if the molecule loses energy ΔE, the scattered frequency will be $(\upsilon + \Delta E/h)$. Radiations scattered with a frequency lower than that of the incident beam is referred to as Stokes’ radiation, while that at higher frequency is called anti-stokes’ radiation.

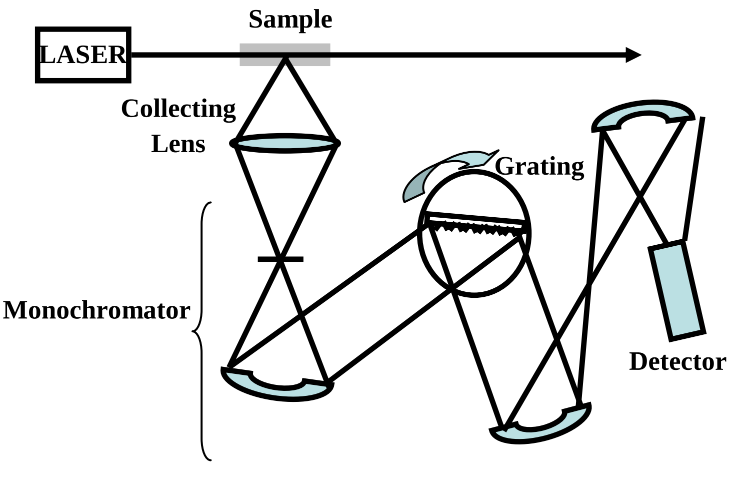

Figure 2.11: Schematic of Raman Spectrometer.

Figure 2.11 shows the schematic of Raman spectrometer. Raman Spectrometer consists of Laser beam (very narrow, monochromatic, coherent and powerful) which when passed through the sample cell (usually a narrow glass or quartz tube filled with the sample) get scattered sideways from the sample, which is collected by a lens and passed into a grating monochromator. The signal is measured by a sensitive photo multiplier tube (PMT) and after amplification; it is usually processed by a computer which plots the Raman spectrum.

Raman spectroscopy measurements were done on confocal micro-Raman spectrometer LabRAM ARAMIS Horiba Jobin-Yvon apparatus with laser excitation wavelength of 632 nm.

2.4.4 Scanning Electron Microscopy (SEM)

Scanning Electron Microscopy allows direct observations of topography and morphological features with high resolution and depth of field than optical microscope. In SEM electron beam is focused onto surface of the specimen and scanned back and forth across the surface [15, 16].

A typical schematic of a SEM is shown in figure 2.12. The instrument can be simplified into three major sections: a) electron-optical column; b) vacuum system and c) electronics and display system. The electron column consists of an electron gun and two or more electron lenses, which influence the path of electrons travelling down an evacuated tube.

A tungsten filament is heated to 2700 °K, which produces electrons that are accelerated at the voltages in the range of 2 to 40 kV. Condenser lens system is used to focus the electron beam to a diameter of about 5 nm. Ultimate performance of the SEM is mainly limited by the diameter of the beam. The surface of the specimen is brought into the focus of electron beam. These fast primary electrons (PE) interact in various ways with the surface layers of the specimen. A cathode-ray display tube is scanned synchronously with the electron beam. The signals produced control the brightness of a screen tube such that an image of the surface of the sample appears. The samples should be electrically conductive, otherwise, it may get overcharged due to the irradiations.

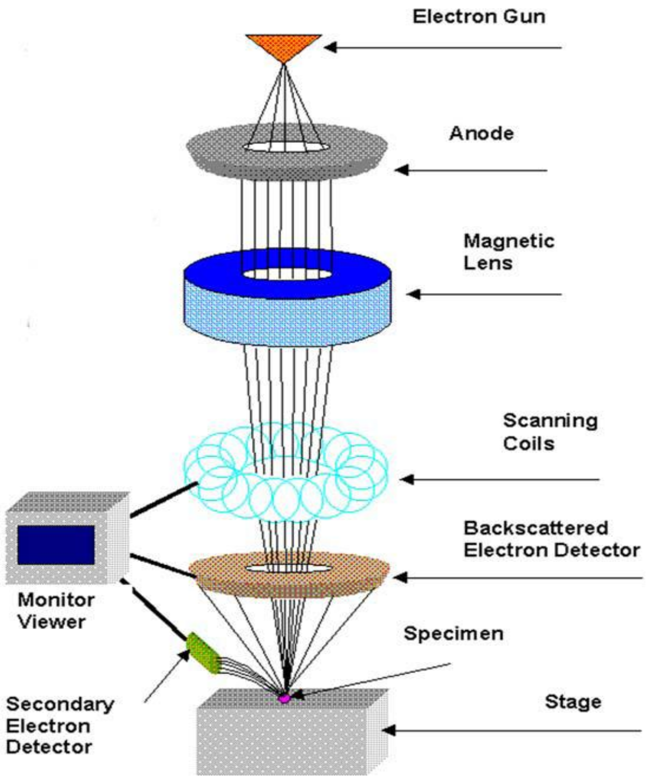

Figure 2.12: Schematic diagram of Scanning Electron Microscope (SEM). [*http://www.rpi.edu/dept/materials/COURSES/NANO/shaw/Page5.html*]

When the electron beam interacts with the specimen, many types of signals are generated. The two signals most often used to produce SEM images are secondary electrons (SE) and backscattered electrons (BSE). These elastically scattered electrons usually called 'backscattered electrons' (BSE) are used for backscattered electron imaging. These images provide information about the distribution of different elements in the sample as the intensity of backscattered electrons strongly depends on the atomic number (Z) of the elements in the sample. Some other electrons scatter inelastically due to the loss in kinetic energy upon their interaction with orbital shell electrons. The incident electrons may knock off loosely bound conduction electrons out of the surface of the sample. These are secondary electrons (SE) and are used for SEM topographical imaging.

2.4.5 Transmission Electron Microscopy (TEM)

TEM operates on the same basic principles as that of light microscope but uses electrons instead of light. What we can see with a light microscope is limited by the wavelength of light. TEM uses electrons as "light source" and their much lower wavelength makes it possible to get a resolution thousand times better than that with a light microscope [17]. We can see objects to the order of a few nanometers (10^{-9} m).

The basic components of TEM are: an electron optical column, a vacuum system, necessary electronics (lens supplies for focusing and deflecting the beam and the high voltage generator for the electron source) and the software. In TEM, a thin specimen is illuminated with uniform and high intensity electrons. The interaction of an electron beam with a solid specimen results in a number of elastic or inelastic scattering phenomena. In this thin area, only a few electrons are scattered and more than 90% of the incident beam is undeviated. Regions of the specimen, which are thicker, or of higher density will scatter the electron beam more strongly and will appear darker in the image. If the specimen is too thick, the number of electrons transmitted reduces and this reduces the contrast. Hence, the specimen thickness should be of the order of 100 nm or less.

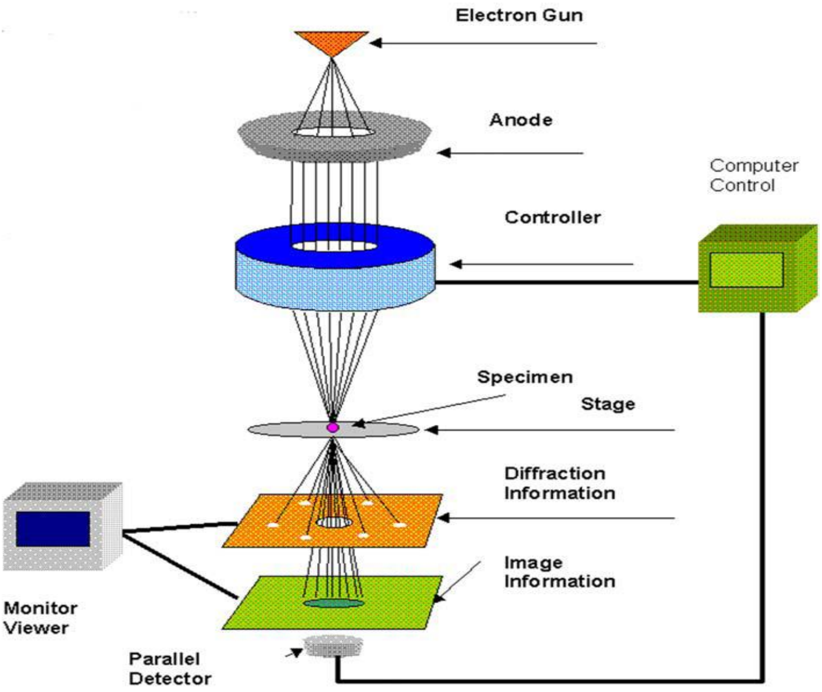

Figure 2.13: Schematic diagram of the Transmission Electron Microscope (TEM). [http://www.rpi.edu/dept/materials/COURSES/NANO/shaw/Page5.html]

2.4.6 Dielectric Relaxation Spectroscopy (DRS)

The dielectric relaxation spectroscopy (DRS) has been emerged as a powerful technique in probing the relaxation dynamics of polymer matrix at molecular level [18, 19]. The major advantage of using dielectric spectroscopy compared to other techniques is the broad frequency range covered in this technique. The broad frequency range allows investigating different characteristic relaxation processes having wide range of time and length scales. In dielectric spectroscopy, by observing the dipolar relaxation as a function of temperature and frequency, effects due to intermolecular co-operative segmental motion and hindered dipole orientation can be elucidated.

A typical set up for the measurement dielectric properties is shown in figure 2.14. Dielectric properties of the samples in the film phase are measured using the Novo Control Alpha A Analyzer equipped with ZGS active sample cell having temperature controller and WinDeta, WinImp and WinFit softwares. The samples are scanned between frequencies 0.01Hz and 1MHz at temperature ranging from 30 to 100 °C. Bias voltage applied across the sample is 0.1 V. The electrode of 20 mm diameter is used while thickness of the sample is measured and used while calculating the dielectric constant.

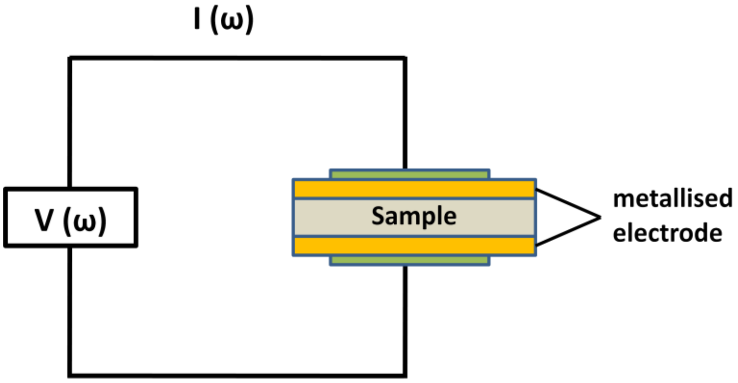

Figure 2.14: Schematic of principle of dielectric spectroscopy.

In dielectric spectroscopy, a small electric perturbation in the form of sinusoidal voltage is applied to samples. The electric field produces polarization, causing oscillation of the same frequency as that of the applied field but with a phase shift (θ). The phase angle shift is measured by comparing the applied voltage to the measured current. The measured response is represented into a complex form (ε*) that can be separated into capacitive and conductive components giving the real part of permittivity (ε′) and loss factor (ε").

The complex permittivity is defined as:

$$\varepsilon^{*}(f) = \varepsilon'(f) - i\,\varepsilon''(f)$$

Where, ε′ is the real part of permittivity and ε″ is the imaginary part of permittivity. The ratio of the imaginary to the real part (ε″/ε′) is termed as ‘‘dissipation factor’’ which is represented by tan δ, where δ is the phase angle between applied voltage and resulting current

The various relaxation processes with different time scales and length scales can be studied using dielectric spectroscopy. Following are the characteristic relaxation processes seen in polymer nanocomposites as a function of frequency and temperature,

- Co-operative relaxation (α_a) - Co-operative segmental relaxation in the amorphous phase of polymer associated with the onset of glass transition temperature (T_g).
- Crystalline relaxation (α_c) - Relaxation in local crystalline chains of polymer.
- Maxwell-Wagner-Sillars (MWS) polarization - MWS polarization is associated with the charge trapping at the interface of composites having materials with large difference in the permittivity.

Fitting to Experimental Data

Frequency dependent dielectric permittivity can be studied using several models. Debye was the first to predict the frequency dependence of dielectric relaxations in polymers [18].

The Debye equation for fitting the dielectric spectra is given by:

$$\varepsilon\,(\omega) = \varepsilon_{\infty} + \frac{\Delta\varepsilon}{1 + i\omega\tau}$$

Where $\Delta\varepsilon = \varepsilon_s - \varepsilon_\infty$ is relaxation strength (ε_s is low frequency permittivity and ε_∞ is high frequency permittivity), τ= relaxation time, $\omega = 2\pi f$.

Generally the relaxation time distribution in polymers is much broader and asymmetric than a single Debye process. A phenomenological model which accounts for the broader and asymmetric nature of the relaxation was developed by Havriliak-Negami (H-N) based on empirical modification to Debye equation [20, 21]. The H-N equation also takes into consideration the dc conductivity contribution and is given by following equation:

$$\varepsilon(\omega) = \varepsilon' - \varepsilon" = -i\left(\frac{\sigma_{dc}}{\varepsilon_0\omega}\right)^N + \left(\frac{\Delta\varepsilon}{(1 + (i\omega\tau_{HN})^{\alpha})^{\beta}}\right)$$

Where σ_{dc} = dc conductivity, α & β are the shape parameters describing the symmetric and asymmetric broadening parameters respectively, τ_{HN} = relaxation time, $\Delta\varepsilon = \varepsilon_s - \varepsilon_\infty$ is relaxation strength and $\omega = 2\pi f$.

H-N equation is the generalized equation for fitting the dielectric relaxation of polymer as it also includes Cole-Cole equation (β =1), Cole-Davidson equation (α=1) and Debye equation (α=β=1) as a special case. H-N analysis provides better understanding of the relaxation time scale (τ), the magnitude (relaxation strength) and the shape (α, β) of each relaxation processes; particularly, time scale of relaxation processes that can be extracted from the H-N equation fitting. This relaxation time can be further analyzed in terms of Arrhenius equation for determining the activation energy of the relaxation process.

Activation energy:

The temperature dependence of a relaxation process can be analyzed by plotting the frequency maximum against the reciprocal temperature. The maximum frequency (or temperature) of the peak in the loss spectrum is related to the mean relaxation time of the process and characterizes the molecular mobility.

The crystalline relaxation and MWS relaxation are known to follow Arrhenius type equation given by following equation [22]:

$$f_{\mathrm{max}} = f_0 \exp\left(\frac{-\mathrm{E_a}}{\mathrm{KT}}\right)$$

Where f_{max} = Frequency maximum in permittivity loss spectra, $\mathrm{E_a}$ = Activation energy, K is the Boltzmann’s constant, and T is the temperature.

Unlike the crystalline and MWS relaxation, the time- temperature relationship of the segmental relaxation corresponding to glass transition temperature normally follows a non-linear behavior and can be described by the Vogel-Fulcher-Tammann (VFT) equation given by:

$$\tau = \tau_0 \exp\left(\frac{\mathrm{B}\,\mathrm{T}_0}{\mathrm{T}-\mathrm{T}_0}\right)$$

Where τ, related inversely with frequency, is the segmental relaxation time and τ_0 is the prefactor correlated to the time scale at which the molecules are attempting to overcome some energy barrier. B is a parameter related to the strength for glass-forming. T_0 is a temperature below T_g and at which the segments would be frozen if they were at equilibrium. The width and the asymmetry associated with the distribution of the relaxation times result from a local structural heterogeneity.

Modulus Formalism:

The electric modulus formalism was introduced by McCrum et al. [23] and it is used to study electrical relaxation phenomena in many polymers [24-25]. According to its definition, variations in the large values of permittivity and conductivity at low frequencies are minimized and hence common difficulties like electrode nature and contact, space charge injection phenomena and absorbed impurity conduction effects can be resolved. Electric modulus is an electrical analogue to the mechanical shear modulus.

Electric modulus is defined as a quantity inversely proportional to permittivity and is given by the following equation:

$$M^* = \frac{1}{\varepsilon^*} = \frac{1}{\varepsilon' - j\,\varepsilon''} = \frac{\varepsilon'}{\varepsilon'^2 + \varepsilon''^2} + j\,\frac{\varepsilon''}{\varepsilon'^2 + \varepsilon''^2}$$
$$= M' + j\,M''$$

Where M' and M'' are the real and the imaginary part of electric modulus respectively and ε' and ε'' are the real and the imaginary part of dielectric permittivity. The electric modulus formalism has unique advantages in the interpretation of slow relaxation phenomena processes like MWS relaxation.

To elucidate the importance of electric modulus, we present the dielectric relaxation spectra of PVDF in permittivity and electric modulus formalism shown in Figure 2.15. The dielectric permittivity (ε″) curve for PVDF shows single relaxations at around 10^{+04} Hz and is attributed to crystalline chain relaxation in PVDF. However when the same data is presented in modulus presentation, two relaxations are clearly discernible. An additional peak (around 10^{+00} Hz) in the low frequency region appears in modulus presentation, which was completely masked in permittivity spectra in the low frequency region. This low frequency relaxation is identified as Maxwell-Wagner-Sillars (MWS) relaxation and is observed in many crystalline polymers. This MWS relaxation is attributed to the trapping of ionic charges at the interface between the amorphous and the crystalline regions of the polymer.

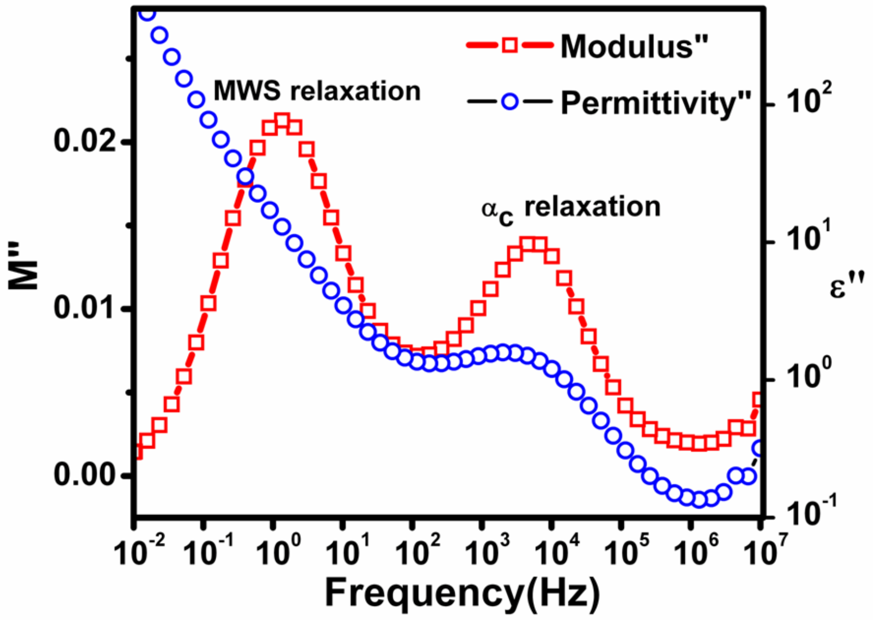

Figure 2.15: Dielectric relaxation spectra of PVDF in permittivity and modulus formalism.

2.4.7 Ferroelectric Analysis

Ferroelectricity is a property of certain materials which possess a spontaneous electric polarization that can be reversed by the application of an external electric field. The term is used in analogy to ferromagnetism, in which a material exhibits a permanent magnetic moment. Ferromagnetism was already known when ferroelectricity was discovered in 1920 in Rochelle salt by Valasek. The distinguishing feature of ferroelectrics is that the direction of the spontaneous polarization can be reversed by an applied electric field, yielding a hysteresis loop. The word spontaneous may mean that the polarization has non-zero value in the absence of electric field. The measurement of hysteresis loop is carried out by applying a sinusoidal voltage to the sample and polarization reversal current and/ or charge is continuously monitored. These measurements allow the determination of remnant polarization (amount of polarization after the poling field has been removed) and the coercive field which are the characteristic features of the ferroelectric materials.

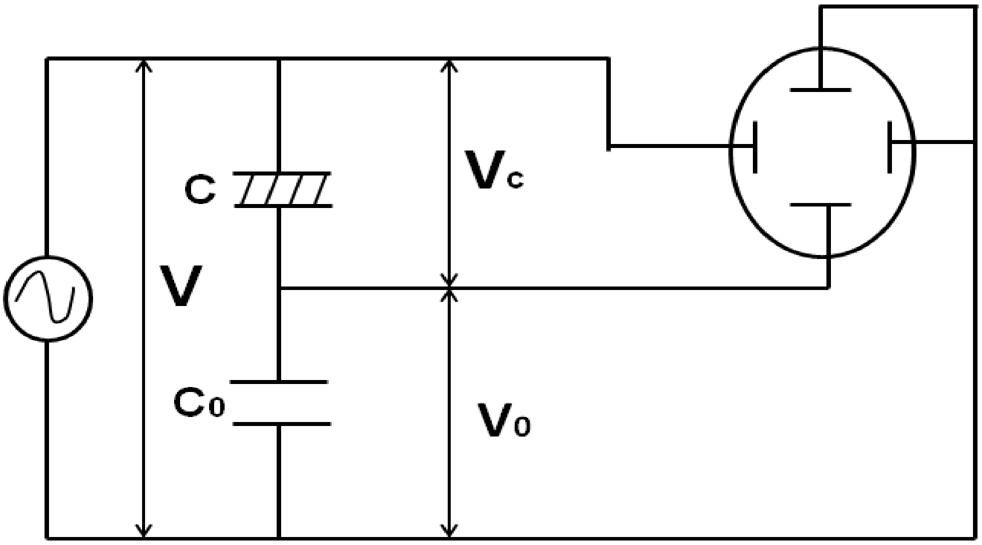

Figure 2.16: The Sawyer-Tower circuit to measure the polarization-electric field characterization.

The Sawyer-tower method is the simplest method to measure the polarization. As shown in figure 2.16 here the ferroelectric capacitor C is kept parallel to a standard capacitor C_0. A sinusoidal voltage signal is applied to one of the electrodes of the ferroelectric capacitor and the amount of charge displacement in the other electrode is measured using the voltage it creates over a reference capacitor connected in series. The voltage V sufficient to polarize the ferroelectric material

$$V = \frac{AP}{C_0}$$

Where, A is the capacitor area, P is the polarization, V is applied ac voltage of low frequency with the applied field across the specimen as $E = \frac{V_c}{d} = \frac{(V - V_c)}{d}$, with d as the sample thickness. Ferroelectricity analysis was carried out using aixACCT systems, GmbH Germany at ARDE, Pune.

2.5 References

1. Hyun-Wook Lee, San Moon, Chang-Hak Choi, Do Kyung Kim, *J. Am. Ceram. Soc.*, **2012**, 1-6.
2. L. Bokobza, J. Zhang, *eXPRESS Polymer Letters*, **2012**, 6,601–608.
3. "*Pulsed Laser Deposition of Thin Films: Applications-Led Growth of Functional Materials*", edited by Robert Eason, Wiley-Interscience A John Wiley & Sons, Inc., Publication, Hoboken, New Jersey, **2007**
4. M S Hegde, *Proc. Indian Acad. Sci.* (*Chem. Sci.*), **2001**, 113, 445–458.
5. "*Pulsed Laser Deposition of Thin Films"*, edited by D. B. Chrisey, G. H. Hubler, Wiley Interscience Publication, NewYork, **1994**.
6. Katarzyna M. Sawicka , Perena Gouma, *Journal of Nanoparticle Research* **2006,** 8, 769–781
7. Wu Aik Yee , Masaya Kotaki , Ye Liu , Xuehong Lu, *Polymer,* **2007,** 48, 512-521.
8. David B. Hall, Patrick Underhill, John M. Torkelso, *Polymer Engineering And Science,* **1998**, 38, 2040.
9. D. Dijkamp, T. Venkatesan, X. D. Wu, S. A. Shaheen, N. Jisrawi, Y. H. Min-Lee, W. L. McLean, M. Croft, *Appl. Phys. Lett.*, **1987**, 51, 619.
10. X. D. Wu, D. Dijkamp, S. B. Ogale, A. Inam, E. W. Chase, P. F. Miceli, C. C. Chang, J. M. Tarascon, T. Venkateshan *Appl. Phys. Lett.*, **1987,** 51, 861.
11. *Elements of X-ray Diffraction*, ed. by B. D. Cullity, Addison Wesley Publishing Co., **1978**.

12. R. W. G. Wyckoff, *Crystal Structures, 2nd ed.,* Wiley, New York, **1964**

13. C. N. Banwell, E. M. McCash, *Fundamentals of Molecular Spectroscopy*, 4th Ed., Tata McGraw Hill Publishing Co. Ltd., **2002**.

14. J. Coates, *Interpretation of Infrared Spectra: A Practical Approach*, *Encyclopedia of Analytical Chemistry*, R.A. Meyers (Ed.), 10815, John Wiley & Sons Ltd, **2000**.

15. G. Lawes, "*Scanning electron microscopy and X-ray microanalysis: Analytical chemistry by open learning",* John Wiley & Sons, **1987**.

16. Jonathan Atteberry, "*How Scanning Electron Microscopes Work*" 21 April **2009**.HowStuffWorks.com *http://science.howstuffworks.com/scanningelectron-microscope.htm*> 13 September 2013.

17. "*Transmission electron microscope*". Art. Encyclopedia Britannica Online. Web. 13 Sep.

18. H. Hammamia, M. Arous, M. Lagache, A. Kallel, *Journal of Alloys and Compounds,* **2007**, 430, 1-8.

19. F. Kremer, *Journal of Non-Crystalline Solids*, **2002**, 30, 1-9.

20. A. Kyritsis, G. Vikelis, P. Maroulas, P. Pissis, B. Milosheva, R. Kotsilkova, A. Toplijska, C. Silvestre, D. Duraccio, *Journal of Applied Polymer Science,* **2011**, 121, 3613-3627.

21. A.C. Comer, A.L. Heilman, D.S. Kalika, *Polymer*, **2010**, 51, 5245-5254.

22. S.A. Madbouly, J.U. Otaigbe, *Polymer*, **2007**, 48, 4097-4107.

23. McCrum, N. G., Read, B. E., Williams G., *Anelastic and dielectric effects in polymeric solids*, Wiley, London, **1967**.

24. G.C. Psarrasas, E. Manolakakib, G.M. Tsangaris, *Composites: Part A*, **2003**, 34, 1187–1198.

25. M. Arous, I.B. Amor, A. Kallel, Z. Fakhfakh, G. Perrier, *Journal of Physics and Chemistry of Solids,* **2007**, 68, 1405-1414.

Chapter 3

Dielectric Relaxations and Low Thermal Emissivity Studies of PVDF/$BaTiO_3$ Nanocomposites

---

In this chapter we describe the fabrication and dielectric relaxation studies of PVDF/$BaTiO_3$ nanocomposites. The nanocomposites exhibit enhanced dielectric permittivity with relatively low dielectric losses. The dielectric relaxation dynamics of nanocomposites was studied in details using different formalisms. The analysis showed presence of different dielectric relaxations which are attributed to crystalline (α_c), glass transition (α_a), and Maxwell-Wagner-Sillars (MWS) relaxations. The nanofibers of PVDF/$BaTiO_3$ were prepared by electrospinning technique. The PVDF/$BaTiO_3$ nanofibers were found to crystallize in ferroelectric β phase during electrospinning process. The electrospun fibers were tested for low thermal emissivity material having application in camouflaging technology. The nanocomposite nanofibers showed reduction in the thermal emissivity.

Part of the work presented in this chapter has been published in following journals:

1. C.V. Chanmal, J. P. Jog, *eXpress Polymer letters*, 2008, 2, 294-301.

2. C. V. Chanmal, J. P. Jog, *Int. J. Plast. Technology*, 2011.

Section I: Dielectric Relaxation Dynamics in PVDF/$BaTiO_3$ Nanocomposites

3.I.1 Introduction

Polymer loaded with electroactive ceramics have been studied extensively because of the need for flexible materials having high dielectric permittivity and low processing cost [1]. In these nanocomposites, the final properties depend essentially on many parameters such as grain size of ceramic, preparation method of composites and on the dispersion of the ceramic particles into the polymer matrix [2, 3, 4, 5].

PVDF is a semicrystalline polymer and exhibits different polymorphic phases. PVDF has relatively high dielectric permittivity and low dissipation factor making it a suitable material for many applications [6, 7]. PVDF is also studied extensively in industrial applications for its piezoelectric and pyroelectric properties. Generally, piezoelectricity in polymers has an advantage over piezoelectric ceramics for certain applications wherein acoustic impedance similar to that of water or living tissue is required [8]. Due to excellent electrical properties and semicrystalline structure, the investigation of dielectric and electrical behaviors of PVDF is essential from the fundamental and technological point of view [9].

Pure polymers have low dielectric permittivity, even though they have high dielectric breakdown strength. In many applications it is essential to have material having high dielectric permittivity with low dissipation factor. One common approach to increase the dielectric permittivity of polymer is to add ferroelectric ceramic into the polymer matrix. In last decade, significant efforts were made to combine the ferroelectric properties of polymer and high dielectric permittivity of the ceramic material. These nanocomposites can be potential material for high breakdown strength, charge storage and high dielectric permittivity applications. Although there are few reports on the studies of dielectric properties of PVDF/$BaTiO_3$ nanocomposites, the relaxation dynamics in these nanocomposites was not studied in details [10, 11]. To realize microscopic properties of nanocomposites from molecular concepts it is important to understand motions or dynamics of these materials in response to electric fields. There are several techniques to understand dynamics in polymer nanocomposites. Dielectric relaxation spectroscopy (DRS) is emerged as an excellent tool to characterize the dielectric and electric behaviors of polymers. DRS has been widely used to investigate the nature of molecular motions in polymers[12, 13].

The wide frequency range of the dielectric spectroscopy allows to characterize the material over broad range of both time and length scale. In dielectric spectroscopy, the magnitude and frequency location of the energy absorption associated with various processes depend critically on physical and chemical nature of the material [14].

In the present work, relaxation dynamics in PVDF/$BaTiO_3$ nanocomposites at low $BaTiO_3$ content i.e. upto 11.5% by volume is investigated using dielectric spectroscopy over a temperature range from 30 °C to 150 °C. The nanocomposites were prepared by simple melt mixing technique and characterized for morphology, structure, mechanical, and dielectric properties. The different dielectric relaxations processes in the PVDF/$BaTiO_3$ nanocomposites were identified viz. crystalline (α_c), glass transition (α_a) and MWS relaxation. The frequency and temperature dependence of these relaxations were studied in detail. The dynamics of relaxations was further studied using Cole-Cole plot and activation energy analysis. The measured data is presented with different formalisms for better understanding the dielectric properties. Electric modulus formalism was used to analyze the relaxation mechanism which helps to minimize the effect of conductivity on the relaxation process. The results show that, PVDF/$BaTiO_3$ nanocomposites exhibit desired dielectric properties for potential application in embedded capacitor technology.

3.I.2 Experimental

3.I.2.1 Materials

PVDF grade, Solef 1008 procured from Solvay Belgium was used for this study. $BaTiO_3$ nanoparticles of more than 99% purity were procured from Aldrich chemicals. The average size of nanoparticles is around 30-50 nm. The density of the nanoparticles is 6.08 gm/cc at 25 ^{o}C.

3.I.2.2 Fabrication of PVDF /$BaTiO_3$ Nanocomposites

The nanocomposites of PVDF with various weight percent of $BaTiO_3$ (10, 20 & 30 % wt/wt) were prepared by melt mixing in Thermo Haake Polylab batch mixer at 200 ^{o}C, with 60 rpm and residence time of 5 minutes. Prior to melt processing, all the materials were dried in an air circulatory oven at 70 ^{o}C for 24 h. The films of uniform thickness were compression molded at 200 ^{o}C under 5-ton pressure using Carver Press (Germany). The thickness of the films was around 0.4 to 0.5 mm.

3.I.2.3 Nanocomposites Characterization

Scanning Electron Microscopy (SEM)

The dispersion of $BaTiO_3$ nanoparticles in the polymer matrix is determined from the morphology of fractured surfaces of PVDF/$BaTiO_3$ nanocomposites using Leica-440 Scanning Electron Microscope. To observe dispersion, the composites were cooled below their glass transition temperature in liquid nitrogen and fractured to expose the surfaces with internal microstructure. To avoid charging effects, the fracture surface was coated with gold and then examined with a scanning electron microscope.

X-ray Diffraction (XRD)

The microstructure of the nanocomposites was evaluated by performing wide angle X-ray Diffraction experiments (XRD) using Rigaku model Dmax 2500 X-ray diffractometer. The system consisted of X-ray source of Cu $K\alpha_1$ (λ=0.154 nm) radiation operated at 40 kV and 150 mA. Scanning rate during measurement was 4°/min.

Dielectric Relaxation Spectroscopy (DRS)

Complex dielectric permittivity measurement of PVDF and PVDF/$BaTiO_3$ nanocomposites was done using Novocontrol broadband dielectric spectrometer with the ZGS active sample cell equipped with temperature controller and WinFit software for data analysis. The dielectric response of material in the frequency ranging from 10 MHz to 0.01 Hz over the temperature range of 30 °C to 150 °C was measured by placing sample between two 20 mm gold plated electrodes. Quick drying silver paste was used to ensure good electrical contact.

3.I.3 Results and Discussion

3.I.3.1 Morphology

The cryofractured surface morphology of PVDF/$BaTiO_3$ nanocomposites studied using scanning electron microscopy (SEM) is shown in Figure 3.1. SEM micrograph reveals slight agglomeration of $BaTiO_3$ nanoparticles in the nanocomposites. The average aggregate size of filler in nanocomposites is around 100 nm. The microscopic observation validates the nano-dispersion of filler in the polymer matrix.

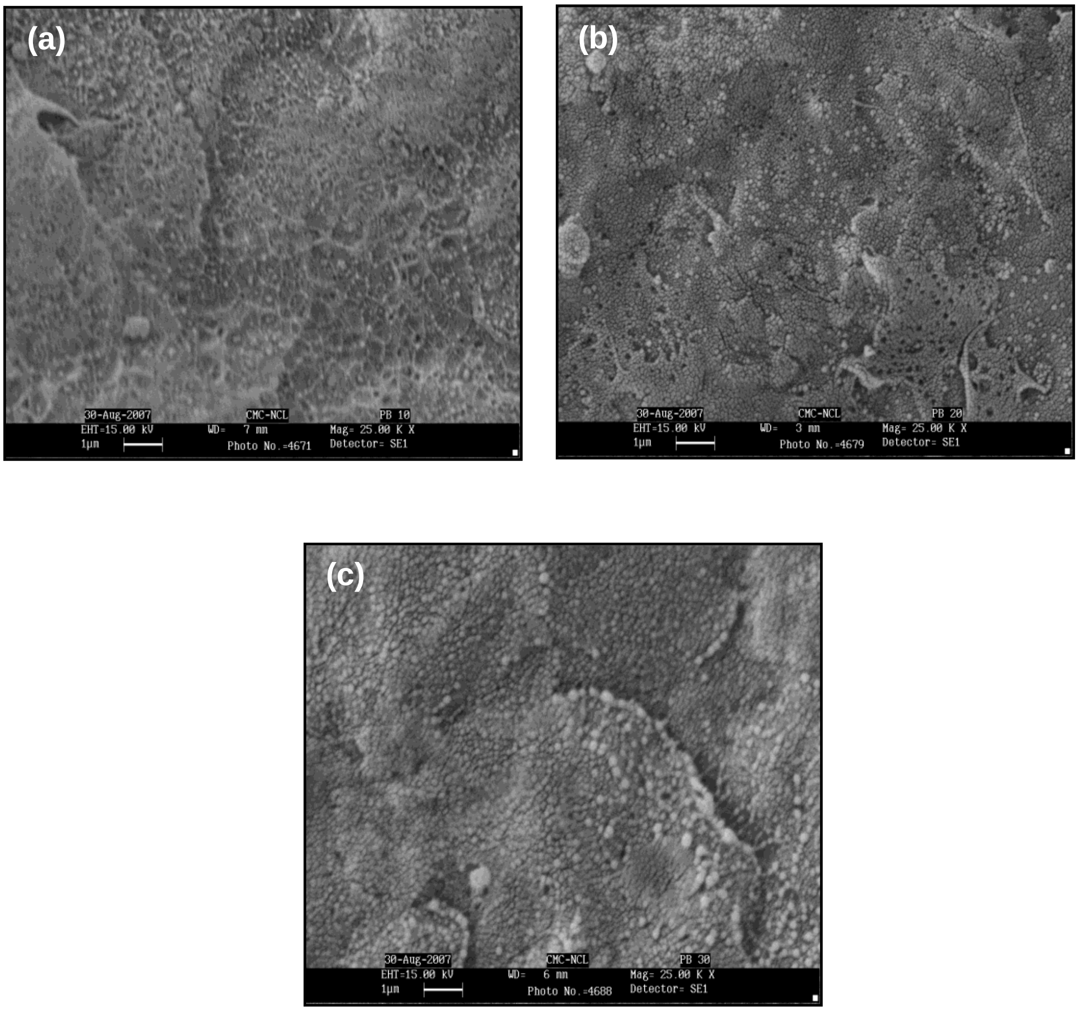

Figure 3.1: SEM micrographs of PVDF/$BaTiO_3$ nanocomposites with (a) 10% (b) 20% and (c) 30% of $BaTiO_3$ nanoparticles.

3.I.3.2 Structural Analysis

Figure 3.2 shows the XRD patterns of PVDF and PVDF/$BaTiO_3$ nanocomposites. The peak observed at $2\theta = 18.5°$ & $20°$ were attributed to α phase of PVDF. In case of composites, several characteristic peaks of $BaTiO_3$ were clearly seen in XRD pattern. The peak at $2\theta = 45°$ is attributed to the cubic phase of $BaTiO_3$. The crystalline peaks of PVDF remain unaltered with the addition of $BaTiO_3$. Thus XRD results indicate that PVDF is in α phase and $BaTiO_3$ is in cubic form. However, the diffraction peaks of PVDF in composites show marginal change with increase content of $BaTiO_3$. This change in the characteristic diffraction peaks of PVDF in composites indicates that $BaTiO_3$ nanoparticles dispersion in PVDF has an important effect on crystallization of PVDF. The crystallization of PVDF is expected to be affected with the addition of $BaTiO_3$ [15].

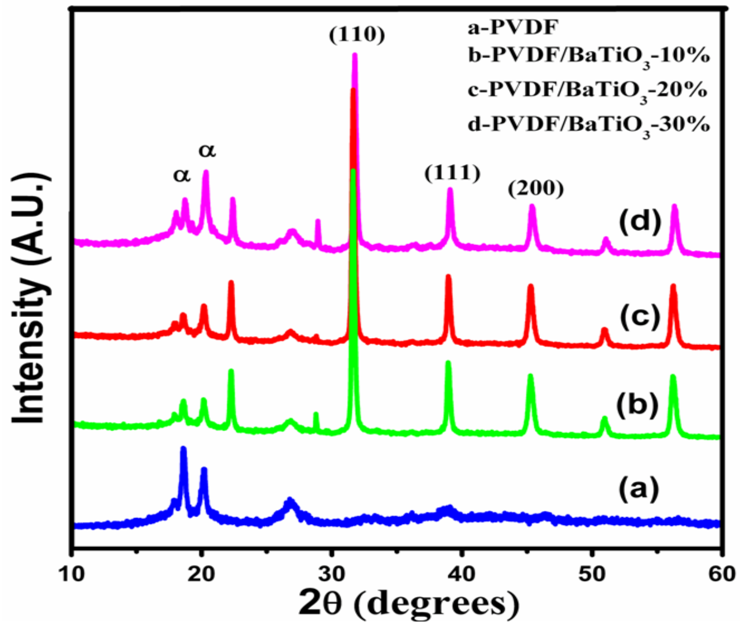

Figure 3.2: X-ray diffraction patterns of PVDF and PVDF/$BaTiO_3$ nanocomposites.

3.I.3.3 Dielectric Relaxation Spectroscopy (DRS)

Dielectric spectroscopy has been widely used in polymer relaxation analysis and has the advantage over dynamic mechanical methods in that it covers much wider frequency ranges [16-19]. The study of dielectric properties of polymers as a function of frequency and temperature can be used to elucidate the effects due to intermolecular co-operative motions and hindered dielectric rotations.

Frequency Dependence of Dielectric Permittivity

Figure 3.3 shows the typical plot of dielectric permittivity (ε') of PVDF/$BaTiO_3$ nanocomposites as a function of frequency at 30 °C. As expected, the dielectric permittivity of PVDF/$BaTiO_3$ nanocomposites increases significantly with the increase in $BaTiO_3$ content. It can be found that dielectric permittivity measured at lower frequency is always greater than higher frequency. The frequency dependence of dielectric study indicates that introduction of $BaTiO_3$ increases the dielectric permittivity of the PVDF from about 11 to 25 at 30 wt% of $BaTiO_3$ content at 10^{-02} Hz. In the studied frequency range 10^{-02} Hz to 10^{+07} Hz, the decrease in dielectric permittivity of PVDF/$BaTiO_3$ nanocomposites with increase in frequency is similar to that of PVDF. Dielectric permittivity remains almost constant in the frequency range from 10^{+02} Hz to 10^{+06} Hz. With the increasing frequency, a significant drop in dielectric permittivity occurs when frequency reaches to 10^{+02} Hz. This is attributed to the dipole relaxation of the polymer composites which lags behind the rapidly changing applied fields. In this regime, characteristic relaxation peaks of PVDF matrix can be observed.

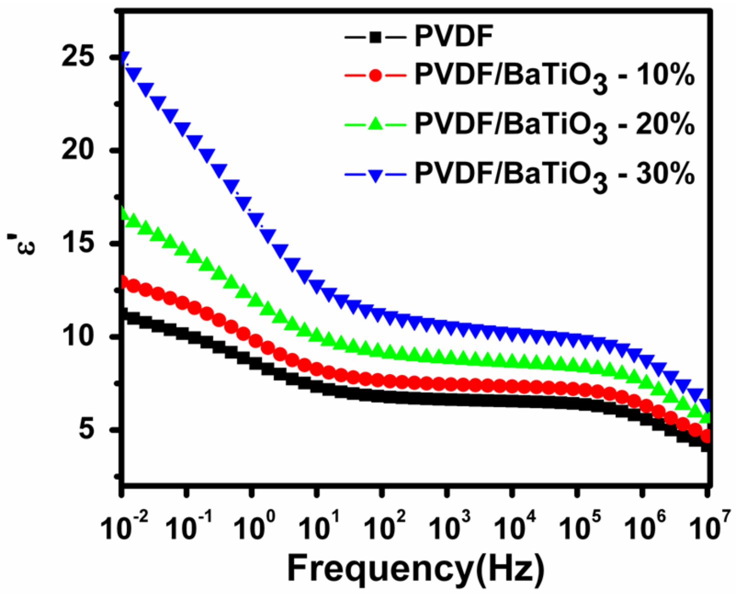

Figure 3.3: Dielectric permittivity (ε') of PVDF and PVDF/$BaTiO_3$ nanocomposites as a function of frequency at 30 °C.

Dielectric Relaxations

Figure 3.4 shows the dielectric loss (ε") plot of PVDF/$BaTiO_3$ nanocomposites as a function of frequency at 30 °C. Two dielectric relaxations are seen in the dielectric loss curve of PVDF. The peak at 10^{+07} Hz is related to the glass transition relaxation of PVDF and is denoted as α_a relaxation [19, 20]. The frequency and temperature limit of the instrument constraints the full view of α_a relaxation. Earlier reported literature work also confirms peak at 10^{+07} Hz is related to the micro-Brownian cooperative motions of the main chain backbone and is dielectric manifestation of the glass transition temperature of PVDF [21]. The relaxation peak at about 10^{+00} Hz is associated with the molecular motions in crystalline region of PVDF and is denoted as α_c relaxation. The presence of α_c relaxation peak in PVDF/$BaTiO_3$ nanocomposites confirm the non-polar i.e. α phase of PVDF in nanocomposites [22]. Several interpretations of these transitions have been reported in the literature [23-25]. Takahashi and Miyaji et al. [23] attributed this relaxation to the reversible conformation rearrangement in the crystals while Nagakawa and Ishida [24] have attributed this relaxation to the molecular motions in chain folds of crystalline lamellae and in the interior of crystals. Miyamoto et al. [26] have ascribed this transition to the change in conformation with internal rotation that occur in crystalline phase and have reported that the defects in the crystalline phase play a major role.

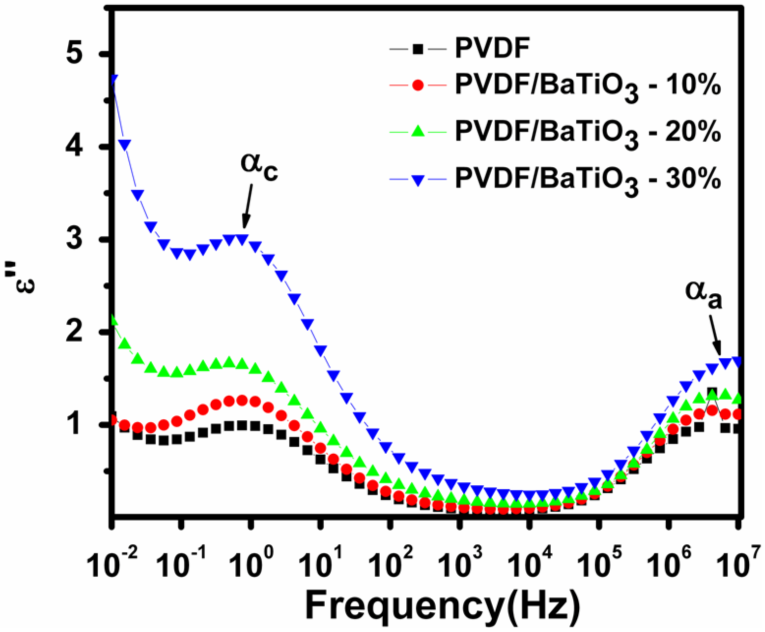

Figure 3.4: Dielectric loss (ε") of PVDF and PVDF/$BaTiO_3$ nanocomposites as a function of frequency at 30 °C.

The frequency dependence of dielectric loss can be analyzed by empirical Havriliak - Negami (HN) function. Havriliak - Negami (HN) functional formalism can be phenomenologically described as a combination of the conductivity term with the HN functional form as following equation: [21]

$$\varepsilon(\omega) = \varepsilon' - i\varepsilon'' = -i\left(\frac{\sigma_{dc}}{\varepsilon_0\omega}\right)^N + \sum_{k=\beta,\propto}\left[\frac{\Delta\varepsilon_k}{(1+(i\omega\tau_{HN})^{a_k})^{b_k}}\right]$$

where, σ_{dc} is the direct current electrical conductivity, $\omega=2\pi f$ is the angular frequency, ε_0 denotes the vacuum permittivity, N is an exponent ($0<N<1$), $\Delta\varepsilon$ is the dielectric strength of the k^{th} process, τ_{HN} is the most probable value of the central relaxation time distribution function, and a and b are shape parameters related to symmetric and asymmetric broadening of the relaxation peak, respectively. Figure 3.5 shows the dielectric loss spectrum of PVDF and PVDF/BaTiO$_3$ nanocomposites at selective temperature which can be fitted using HN equations. All HN fits reported here were performed using WinFit software program provided with the Novocontrol dielectric analyzer. The values of the HN parameters a and b for crystalline relaxation of the nanocomposites were found to be similar to those of pure PVDF. This suggests that the intermolecular and intramolecular interactions that arise in the polymer and the nanocomposites are almost identical.

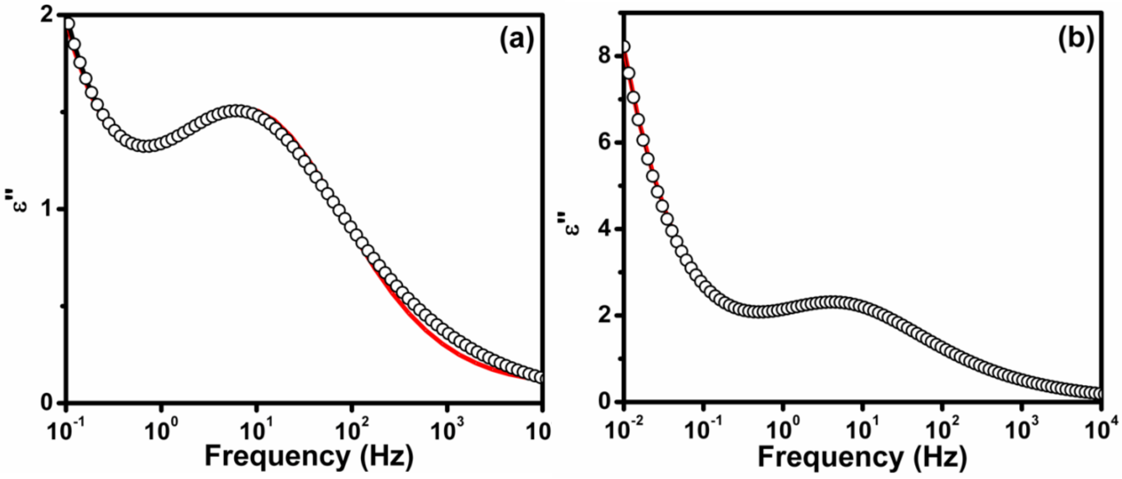

Figure 3.5: Dielectric loss (ε'') as a function of frequency for (a) PVDF and (b) PVDF/BaTiO$_3$-20% nanocomposites at 50 °C. The solid line (red color) represents best H-N fit to the crystalline relaxation observed in PVDF.

Temperature Dependence of Dielectric Permittivity

The dielectric permittivity for PVDF in the temperature range of 30 °C to 90 °C over a frequency range 10^{-02} Hz to 10^{+07} Hz is shown in Figure 3.6(a). As can be seen, the dielectric permittivity increases with increasing temperature. The room temperature value of permittivity for PVDF at frequency 10^{-02} Hz is about 13, which increase to about 42 at 90 °C. In case of permittivity loss curves shown in figure 3.6 (b), the α_a relaxation corresponding to the glass transition temperature shifts to higher frequency with increasing temperature and thus cannot be detected in this experimental window, while the crystalline relaxation is clearly visible. The crystalline relaxation peak shifts systematically to higher frequency with the increasing temperature. At elevated temperatures the dielectric loss in the low frequency regime increases continuously as a result of contributions due to conductivity from mobile charge carriers.

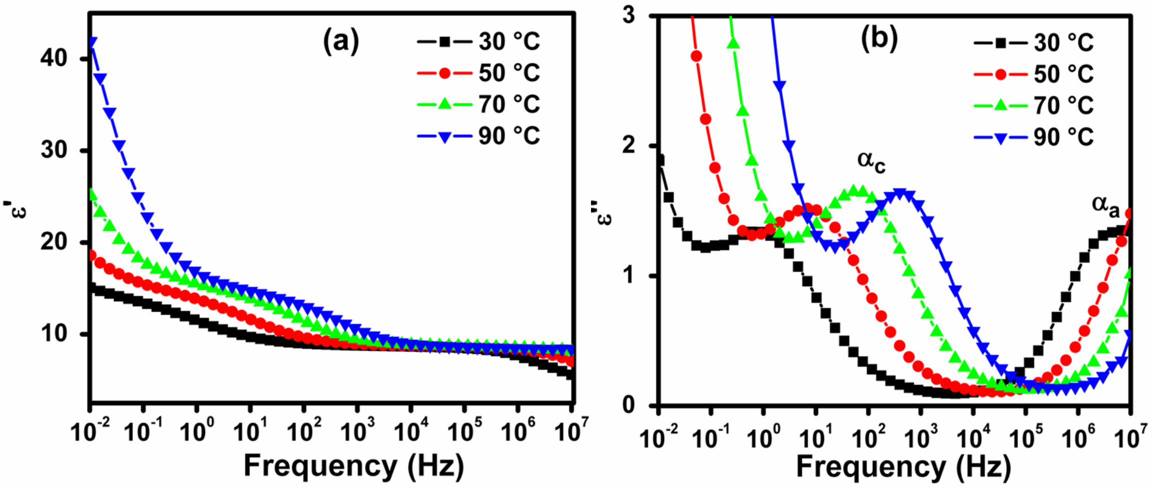

Figure 3.6: (a) Dielectric permittivity (ε') and (b) loss (ε'') at various temperatures for PVDF.

The temperature dependence of PVDF/BaTiO$_3$ nanocomposites also exhibit the similar dielectric behavior to that of PVDF as shown in Figure 3.7. However, the most apparent difference between PVDF and PVDF/BaTiO$_3$ nanocomposites can be seen at low frequency region. The conductivity effect in the low frequency is more pronounced in PVDF/BaTiO$_3$ nanocomposites as compared to that of PVDF. The behavior is similar to that observed in polyisoprene and organically modified 25A nanocomposites [27]. The increase in the values of the permittivity and the displacement of the peak maximum of permittivity with the temperature are characteristic behavior of dielectric dispersion. Most generally, in the system with low conductivity the rapid increase of the permittivity at very low frequency is due to the electrode polarization and the effect of electrode polarization can completely mask the low frequency relaxation.

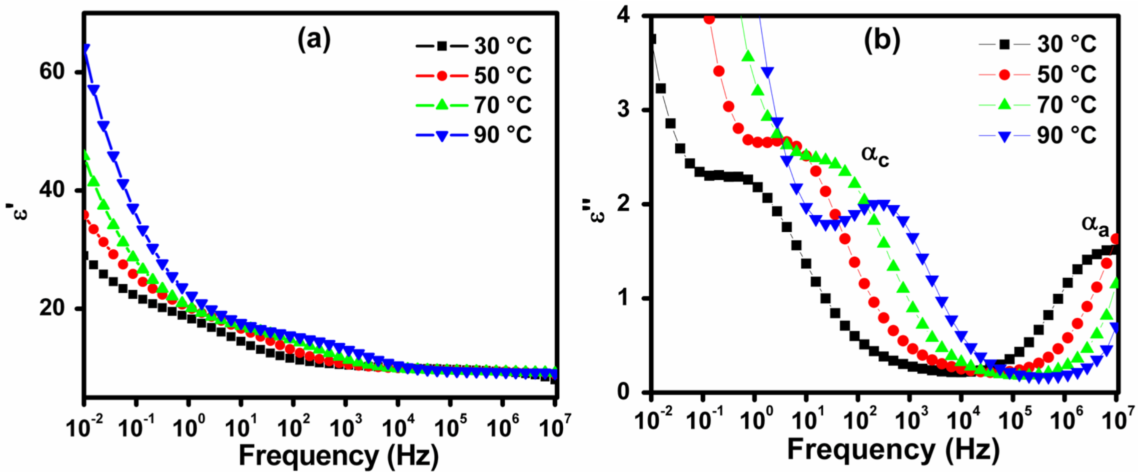

Figure 3.7: (a) Dielectric permittivity (ε') and (b) loss (ε'') at various temperatures for PVDF/BaTiO$_3$*- 30%.*

3.I.3.4 Electric Modulus Formalism

When electrode polarization effect dominates the dielectric loss spectra and masks relaxation spectra in the low frequency region, electric modulus formalism is used to resolve low frequency relaxations. The electric modulus formalism is introduced by McCrum et al [14] and it is used to study electrical relaxation phenomena in many polymers [28-30]. As the dielectric modulus is derived from the dielectric permittivity and loss values, it contains the similar information of the sample, however contributions from electrode polarization are reduced.

The electric modulus can be defined by the following equation:

$$M^* = \frac{1}{\varepsilon^*} \ , \ M' = \frac{\varepsilon'}{\varepsilon'^2 + \varepsilon''^2}, \ M'' = \frac{\varepsilon''}{\varepsilon'^2 + \varepsilon''^2},$$

Where M' and M'' are the real and the imaginary part of electric modulus respectively, and ε' and ε'' are the real and the imaginary part of dielectric permittivity.

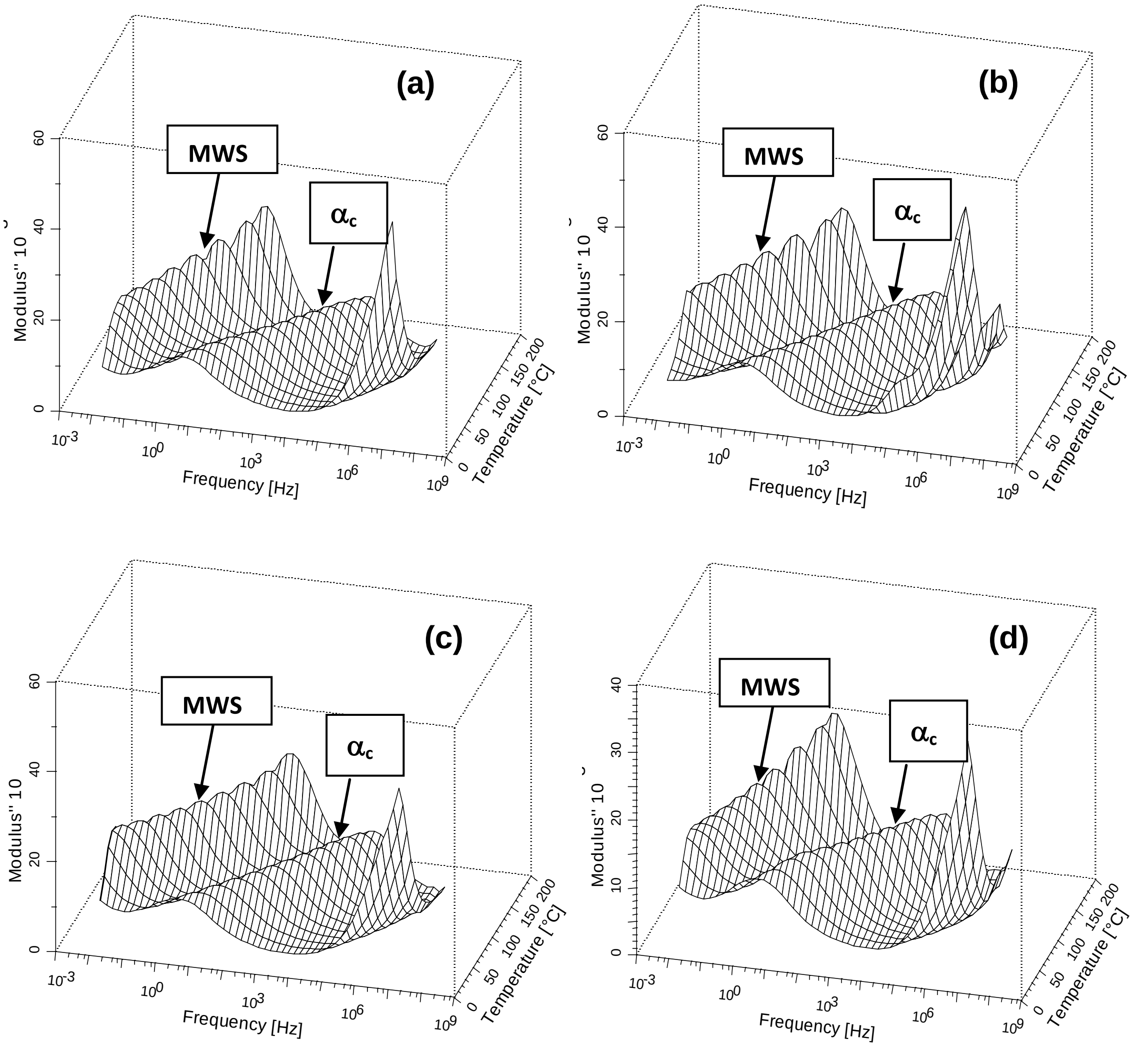

Figure 3.8: Dielectric loss modulus (M'') as a function of frequency and temperature for (a) PVDF (b) PVDF/BaTiO$_3$ –10% (c) PVDF/BaTiO$_3$ –20% (d) PVDF/BaTiO$_3$ –30%

Figure 3.8 (a) shows typical 3-d plots of dielectric modulus spectra for pure PVDF at various temperatures as a function of frequency. Two relaxation processes can be clearly observed in the M″ curves. The relaxation peak at high frequency side is identified as fast symmetric crystalline relaxation and it shifts to higher frequency with the increasing temperature. At high temperature, another relaxation peak appears in modulus spectra. This relaxation is attributed to Maxwell-Wagner-Sillars (MWS) polarization which can be seen in the heterogeneous materials and is also known as interfacial polarization. At temperature above 70 °C the MWS relaxation peak starts appearing in PVDF whereas in PVDF/$BaTiO_3$ nanocomposites the MWS peak is seen at higher temperature about 90 °C. In semicrystalline polymers, the crystalline regions are dispersed in amorphous matrix and MWS relaxation is observed in these materials due to the differences in the conductivity and permittivity values of the crystalline and amorphous phases [31, 27]. For heterogeneous composite, an interfacial polarization is almost always present because of filler additives or even impurities that migrate towards the interface [32]. The modulus relaxation peaks (M") for both relaxation processes shift to a higher frequency with increasing temperature. In addition, there is no significant change in the dielectric relaxation peak height for crystalline relaxation process. However, the intensity of dielectric relaxation peak at low frequency side increases with temperature and peak broadening decreases signifying asymmetric nature of MWS relaxation. Similar dielectric relaxation in the low frequency region below that of crystalline relaxation (α_c) is noted in earlier work on PVDF and this relaxation is ascribed to be interfacial or MWS polarization [33].

The relaxation peaks of PVDF and PVDF/$BaTiO_3$ nanocomposites as a function of frequencies at 120 °C are shown in Figure 3.9. In case of α_c relaxation, peak appears at same frequency for polymer and nanocomposites, whereas MWS peak for PVDF/$BaTiO_3$ nanocomposites shifts to lower frequency as compared to PVDF. The graph also clearly shows that the intensity of MWS relaxation decreases with increasing content of $BaTiO_3$, which is characteristic of MWS relaxation [34, 35]. Similar behavior is observed for PVDF/$BaTiO_3$ nanocomposites at all measured temperatures. It is also noteworthy that the dielectric loss of the nanocomposites arises primarily from the polymer matrices and is almost independent of the volume content of the $BaTiO_3$ filler.

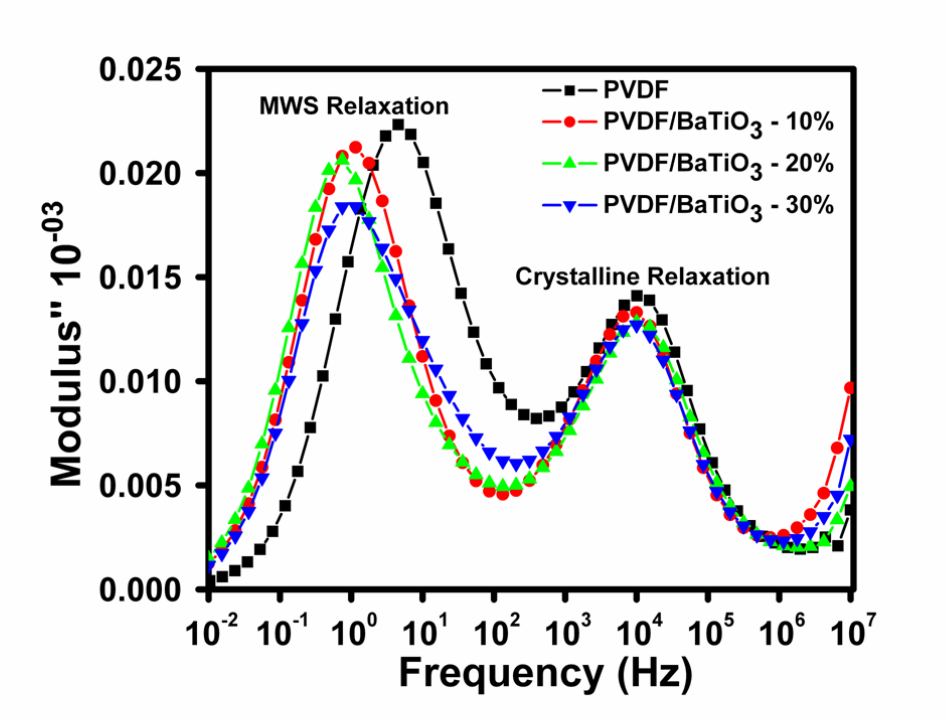

Figure 3.9: Comparison of dielectric modulus spectra of PVDF and PVDF/BaTiO$_3$ *nanocomposites at 120 °C as a function of frequency.*

3.I.3.5 Activation Energy

The temperature dependence for crystalline and MWS relaxations is further analyzed by plotting the logarithm of relaxation time log (τ) at the peak maxima versus reciprocal of temperature (1000/T) as shown in Figure 3.10. The relaxation time, defined as the inverse of frequency maximum, decreases with increasing temperature due to enhancement in the mobility of charge carriers at high temperature. The temperature dependence of dielectric relaxation can be well described by the Arrhenius type behavior.

The plot for crystalline relaxation process exhibits a linear dependence of logarithmic relaxation time log (τ) versus inverse of temperature over a wide temperature range for all composite films and follows Arrhenius equation:

$$\tau\,(T) = \tau_0 \exp\left(-\frac{E_a}{KT}\right)$$

Where, τ = relaxation time corresponding to frequency maximum

E_a = Activation energy

K = Boltzmann’s constant

From the Arrhenius equation, the activation energy (E_a) can be determined from the slope of the curve.

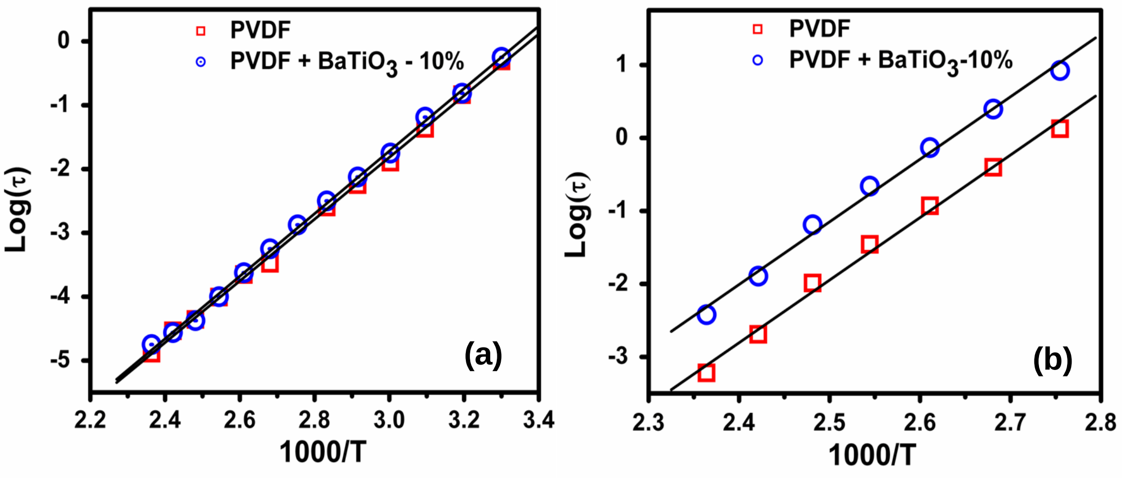

Figure 3.10: Activation energy plot for (a) crystalline relaxation and (b) MWS relaxation showing Arrhenius type behavior.

The slope of the best fitted straight lines gives the activation energy. The activation energy for the crystalline relaxation peak was found to be about 0.41 eV for PVDF as well as for PVDF/$BaTiO_3$ nanocomposites. This value is in good agreement with the reported value of (0.40 eV) activation energy for crystalline relaxation (α_c) in PVDF [36].

The MWS relaxation also shows Arrhenius type behavior indicating relaxation is thermally activated process. The activation energy for MWS relaxation slightly decreases in case of PVDF/$BaTiO_3$ nanocomposites. Table 3.1 summarizes the calculated parameters for crystalline (α_c relaxation) and MWS relaxations.

Composition	Crystalline relaxation (α_c)		MWS relaxation	
	Log τ (sec)	E_a (eV)	Log τ (sec)	E_a (eV)
PVDF	-16.4	0.42	-23.5	1.8
PVDF/$BaTiO_3$-10%	-16.3	0.41	-22.6	1.7
PVDF/$BaTiO_3$-20%	-16.2	0.41	-21.1	1.6
PVDF/$BaTiO_3$-30%	-15.9	0.40	-20.7	1.60

Table 3.1: Fitting parameters for crystalline relaxation and MWS relaxation.

3.I.3.6 Cole-Cole Plot

The relation between real (ε') and complex part (ε'') of dielectric permittivity is expressed using complex plane Cole-Cole plot. Here, a complex electric modulus M*, which is defined as the inverse of complex permittivity ε*, is introduced in the Cole-Cole plot. An advantage of using the complex electric modulus is that the variation in large values of the dielectric permittivity and conductivity at low frequencies are minimized. In this way, familiar difficulties of electrode nature and contact, space-charge injection phenomena can be resolved or ignored [27]. Cole-Cole plot has no frequency axis, but since real part of permittivity is monotonously decreasing function of frequency, hence higher the permittivity lower the frequency. Also, permittivity and modulus are inversely related. Therefore, the peak at higher modulus corresponds to the crystalline relaxation and whereas semicircle at lower modulus corresponds to the MWS type relaxation. The presence of MWS relaxation at higher temperature deviates the semicircle nature of crystalline relaxation.

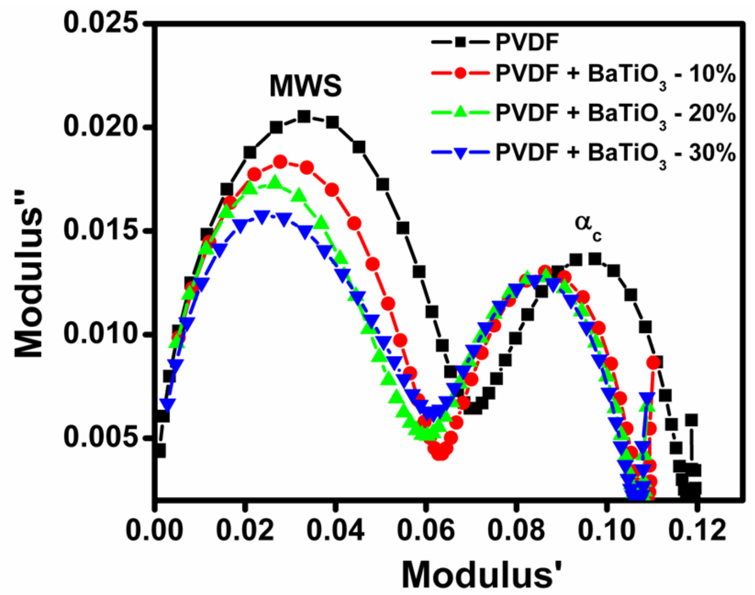

Figure 3.11: Cole-Cole plot of PVDF/BaTiO$_3$ nanocomposites at various loading of BaTiO$_3$ at 100 °C.

Figure 3.11 shows the Cole-Cole plot at 100 °C. Two relaxations are clearly discernible in the Cole-Cole plot. The low frequency relaxation (lower modulus') corresponds to MWS relaxation while the high frequency relaxation (higher modulus') is the crystalline relation (α_c). The crystalline relaxation (α_c) shifts to lower frequency without any composition dependence as a result of incorporation of $BaTiO_3$. Similar shift to lower frequencies is observed for MWS relaxation but with some composition dependence. The shift of relaxation process to lower frequency with increase in filler content indicates the characteristic of MWS nature [37]. The shift in the Cole-Cole plots towards the origin with increasing $BaTiO_3$ content implies an increase in the relaxation time with heterogeneity.

3.I.4 Conclusions

PVDF/$BaTiO_3$ nanocomposites are prepared using simple melt mixing technique. The $BaTiO_3$ nanoparticles are well dispersed in the PVDF matrix as evidenced by the scanning electron micrographs. The dielectric permittivity increases with increasing $BaTiO_3$ content. The room temperature dielectric spectra shows two relaxations processes corresponding to the glass transition (α_a) and crystalline (α_c) relaxation while at high temperature another low frequency relaxation is observed which is attributed to the MWS relaxation. The temperature dependence of α_c-relaxation and MWS relaxation follows Arrhenius type behavior.

Section II: Electrospun PVDF/$BaTiO_3$ Nanofibers for Low Thermal Emissivity

3.II.1 Introduction

In this section we present the fabrication of PVDF/$BaTiO_3$ nanofibers by electrospinning process. The effect of addition of $BaTiO_3$ on the thermal emissivity of electrospun fiber was studied. A prototype instrument based on the principles of black body radiation was built in the laboratory and used for the measurement of the thermal emissivity. A calibration curve is plotted using reference standard materials and this curve was to calculate the thermal emissivity of polymer nanocomposites.

3.II.2 Experimental

The solution (15 wt%/vol) of PVDF was prepared by dissolving PVDF pellets in mixture of DMF and acetone (1:1 ratio) and was heated at 60 °C for 30 min to make the solution homogenous. Solution for PVDF/$BaTiO_3$ nanocomposites were prepared by adding known quantity of $BaTiO_3$ nanoparticles (5 wt%) to the PVDF solution followed by ultrasonication. The viscous solution of PVDF/$BaTiO_3$ nanocomposites was transferred to glass syringe for electrospinning. The glass syringe with 5 ml capacity and a stainless steel needle with 0.8 mm diameter was used for electrospinning. A positive voltage of 15 KV was applied between needle and the collector plate. The fibers were collected onto grounded aluminium foil. The polymer solution was electrospun at a flow rate of 0.075 ml/min on to collector kept at 15 cm from the needle. All electrospinning experiments were carried out at room temperature. The nanofibers mats were dried in vacuum oven at 60 °C prior to characterization. The electrospun mats were characterized for morphology and structural analysis.

Emissivity Measurement using Thermopile as a Sensor

Most generally, Thermopile is used to determine temperature by assuming an emissivity for the object. In the present work we will use thermopile to determine the emissivity of a variety of materials when the surface temperatures kept at constant temperature using PID controller.

A thermopile is basically a number of thermocouples connected in series. When two dissimilar metals connected kept at different temperature then a voltage appears across the junctions, this principle is called “Seebeck effect” and same is used in thermocouple. It is used to convert thermal potential difference into electric potential difference. When temperature difference appears across the junction, because of the difference in the work function of two metals, an electric voltage is generated across the junction. The generated electric voltage is very small in mV and it is proportional to power radiated. The thermopile measures temperature by focusing infrared radiation emitted by an object onto a thermopile detector. The thermopile is heated by this radiation and its equilibrium temperature is proportional to the emissive power of the object which, from the Stefan-Boltzmann law, is

$$\mathbf{P = \in(T)\sigma\, T^4}$$

Where, P is Power radiated from the material, $\in(T)$ is the Emissivity of the object, σ Stefan Boltzmann's constant and T is the temperature

If the temperature is held constant, then power radiated from sample is proportional to the emissivity of the material.

$$\mathbf{P\ \alpha\ \in} \quad \text{(when temperature is kept constant)}$$

This method involves measurement of the electric voltage generated at a constant temperature. The measurement set up consists of detector housing assembly in which IR sensor and sample are enclosed in single housing that avoids external radiation effects. To isolate the detector form sources of radiation other than object, a Teflon sheet is attached in front of detector to ensure thermal isolation of the detector. The measurement sample is firmly place on an Aluminium block with good thermal contact and the metal block is heated by using resistive heating technique.

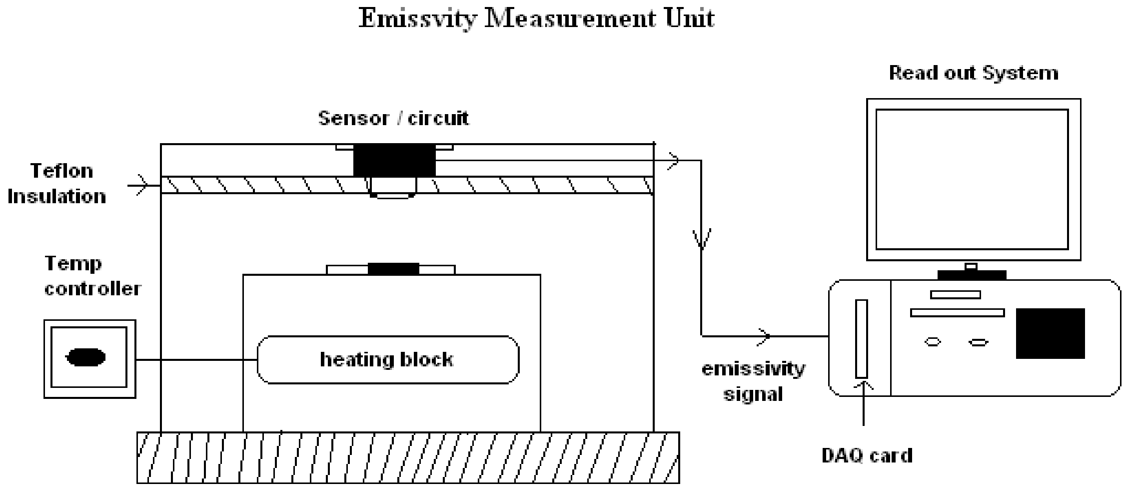

*Figure 3.12**:** Thermopile Set-up Block Diagram for emissivity measurement.*

The block diagram of emissivity measurement instrument is shown in figure 3.12. During the measurement, the temperature of the sample is accurately maintained at 60 °C using PID controller 2216L from Eurotherm. The temperature stabilization is better than 0.1 °C. The temperature was chosen so that the maximum emission, calculated from Weins displacement law, appears at wavelength of 7.8 μm. The detector is mounted in front of the sample at a distance of 15 mm. The distance between sample and detector is optimized by taking field of view concept into account which gives the maximum sensitivity. Field of view is the solid angle through which detector see the object. Electromagnetic radiation (Infrared ray) emitted from sample is focused onto thermopile. Based on principles of thermoelectric effects, thermopile sensor converts the incident thermal radiation into the electric signal in the form of electric voltage. As discussed in the theory of emissivity measurement, this electric signal generated is proportional to emissivity of the material provided temperature is held constant. External electronic circuit is used to activate the thermopile sensor. As the voltage received is in millivolts, a low noise amplifier with the gain of 1000 is used for the amplification. A DAQ card from Labview is installed in computer to receive the data in digital form. The data received is stored on computer using Labview software. The data received can be retrieved in the Excel format. Figure 3.13 shows the photographs of emissivity measurement unit in the lab.

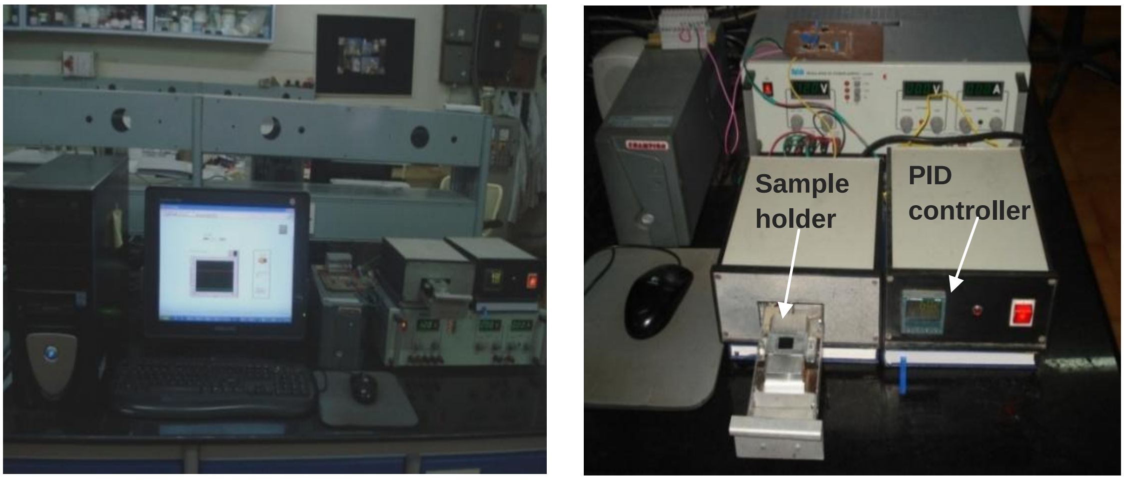

Figure 3.13: Photographs of prototype instrument for the measurement of thermal emissivity.

Emissivity Measurement Procedure

The samples were heated to set temperature with accurate heating control using PID temperature controller. Black body is first loaded into the sample holder. Radiation emitted from black body is directed towards detector, which in turn produces a voltage signal response. Thermal voltage from black body is recorded and saved. Next measurement sample is loaded in sample holder, and its thermal voltage is recorded. Using following relation emissivity of sample is calculated:

$$\varepsilon_{\text{polymer}} = \frac{V_s}{V_{bb}} \times \varepsilon_{\text{black body}}$$

Where, $\varepsilon_{\text{polymer}}$ is emissivity of polymer, $\varepsilon_{\text{black body}}$ is emissivity of black body, V_s is thermal voltage from polymer sample and V_{bb} is thermal voltage from black body.

Calibration of the instrument

The instrument is initially calibrated by using standard set of samples with known values of thermal emissivity (shown in table 3.2). Figure 3.14 shows calibration graph of thermopile for thermal voltage against the reported emissivity of standard materials.

Sr. No.	Standard Material	Reported Emissivity	Thermal Voltage (mV)
1.	Glass	0.92	3.3
2.	Anodized Aluminium	0.8	2.95
3.	Cotton Cloth	0.75	2.78
4.	Silver paste	0.49	2.06
5.	Lead (ruf)	0.43	1.84
6.	Lead (Polish)	0.28	1.44
7.	Stainless steel	0.16	1.4
8.	Al-Foil	0.09	1.16
9.	Copper	0.1	1.18

Table 3.2: Reported emissivity values for standard samples used and the measured thermal voltage.

Calibration graph of thermopile shows that response of the thermopile is linear with r^2 value of 0.99. The nature of graph indicates that emissivity is directly proportional to thermal voltage from thermopile. With this calibration graph emissivity of unknown material can be predicted when thermal voltage is measured from thermopile. The emissivity values obtained were also confirmed with measurement by using IR camera and the results were found to match closely.

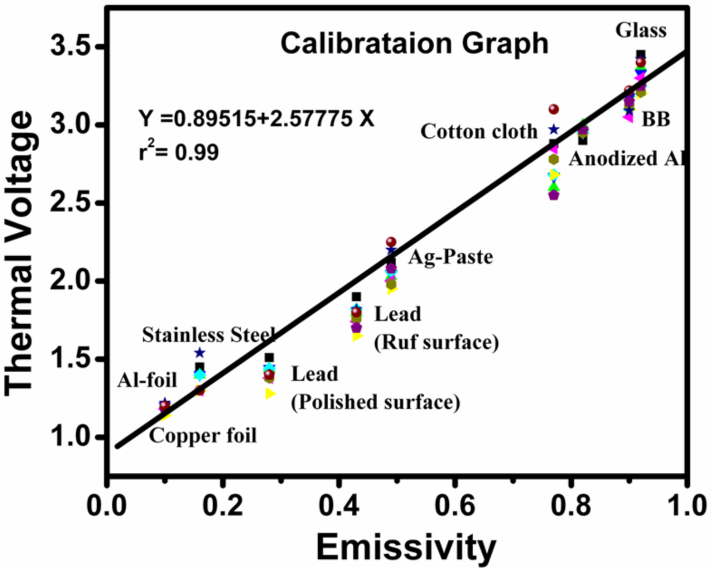

Figure 3.14: Calibration Graph at 60 °C of Thermopile sensor for emissivity measurement

3.II.3 Results and Discussion

3.II.3.1 Morphology

Figure 3.15 depicts the scanning electron micrographs (SEM) of PVDF and PVDF/$BaTiO_3$ electrospun mats. SEM images show the fiber morphology of PVDF/$BaTiO_3$ electrospun mats. It can be seen that the fibers are randomly oriented. Under the processing conditions used in the present study, round fibers with diameters in the range of 100–200 nm are observed.

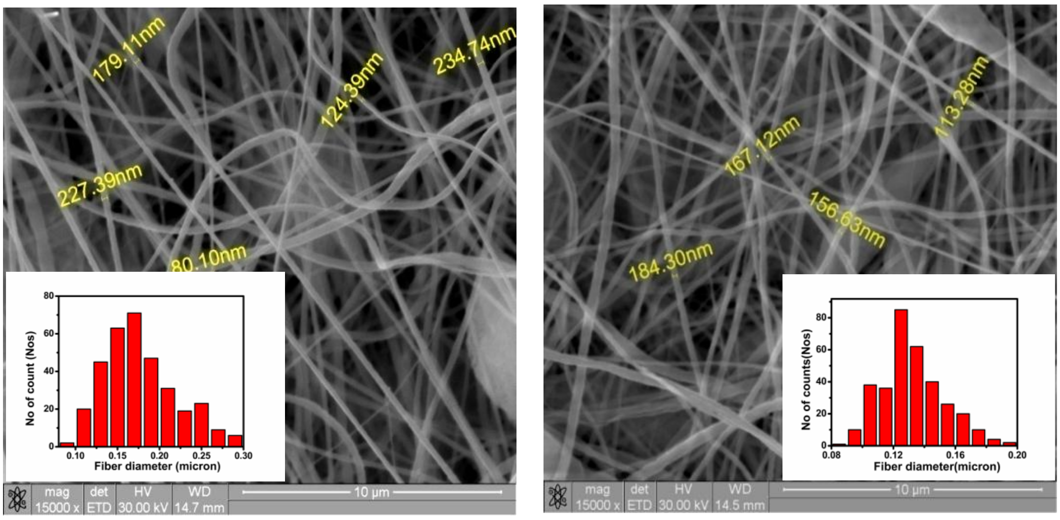

Figure 3.15: SEM micrograph of PVDF and PVDF/$BaTiO_3$ electrospun nanofibers (inset shows the histogram of fiber size distribution).

3.II.3.2 Structural Analysis

Figure 3.16 illustrates the X-ray diffraction patterns for electrospun PVDF and PVDF/$BaTiO_3$ nanocomposites. As can be seen from the diffraction patterns, PVDF electrospun fibers show two peaks at 2θ values of about 19.9° and 18.5° corresponding to the α phase of PVDF. A very fine shoulder appears in PVDF electrospun fiber at 20.8° which corresponds to β phase of PVDF [38]. This indicates that PVDF crystallizes mainly in α phase during electrospinning process. However, X-ray diffraction study of PVDF/$BaTiO_3$ electrospun fiber shows a single diffraction peak at about 20.8° which corresponds distinctively to β phase of PVDF. Thus, X-ray diffraction study shows that addition of $BaTiO_3$ and electrospinning process assist in the formation β phase of PVDF. This β phase formation can be explained on the basis of electrospinning process. Application of high voltage in electrospinning process which acts as a poling field to dipoles in PVDF and stretching of electrospun fiber assists in the enhancement of β phase in PVDF. Thus, these two processing parameters viz. stretching and application of high electric field in electrospinning provides an advantage over other techniques such as melt mixing or solution casting where after the preparation of nanocomposites either stretching or poling has to be done separately to generate β phase in PVDF. Additional peaks at 32°, 39° and 45° confirms the presence of (110), (111) and (200) planes of $BaTiO_3$ nanoparticles respectively.

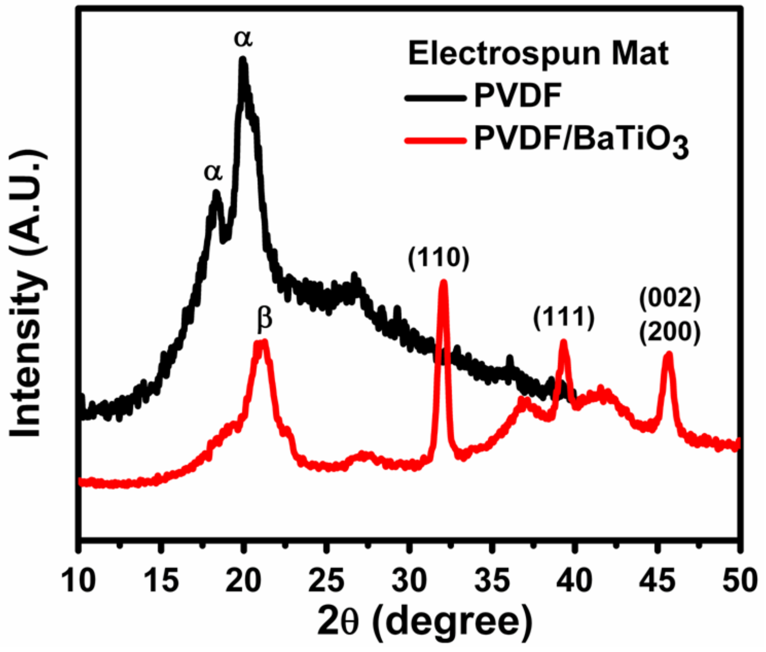

Figure 3.16: X-ray diffraction patterns for electrospun PVDF and PVDF/$BaTiO_3$ nanocomposites.

Figure 3.17 shows the ATR-FTIR spectra of electrospun fiber mats of PVDF and PVDF/$BaTiO_3$ nanocomposite. The electrospun mats of PVDF nanocomposites show peaks at 613,762,840, 874, 975, 1072, 1179, 1275, and 1400 cm^{-1}. The peaks at 613, 762, and 975 cm^{-1} are attributed to α phase of PVDF while the bands at 840 and 1275 cm^{-1} are attributed to the β phase of PVDF [16]. The peaks at 613 and 762 cm^{-1} can be assigned to the CF_2 bending and skeletal bending of C (F)-C (H)-C (F) of α phase of PVDF while the peak at 975 cm^{-1}can be assigned to CH_2 bending mode of α phase of PVDF. The peak at 840 cm^{-1} is due to the CH_2, CF_2 rocking and asymmetric stretching in β phase of PVDF. This clearly shows that the electrospun mats of PVDF exhibit a mixed structure of α and β phase. A comparison of FTIR spectra of PVDF and PVDF/$BaTiO_3$ electrospun mats demonstrates that the absorption bands (613, 762, and 975 cm^{-1}), characteristic of α phase absorption peaks are diminished in intensity as a result of $BaTiO_3$ loading. This observation indicates that the crystallization of PVDF in PVDF/$BaTiO_3$ during electrospinning promotes formation of β phase of PVDF under the set of experimental conditions used. It can be envisaged that crystallization of polymer in electrospinning process is associated with high shear stress and extremely rapid structure formation [39]. Accordingly, stretching of the electrospinning jet could result in change in molecular conformation which facilitates formation of β phase in PVDF.

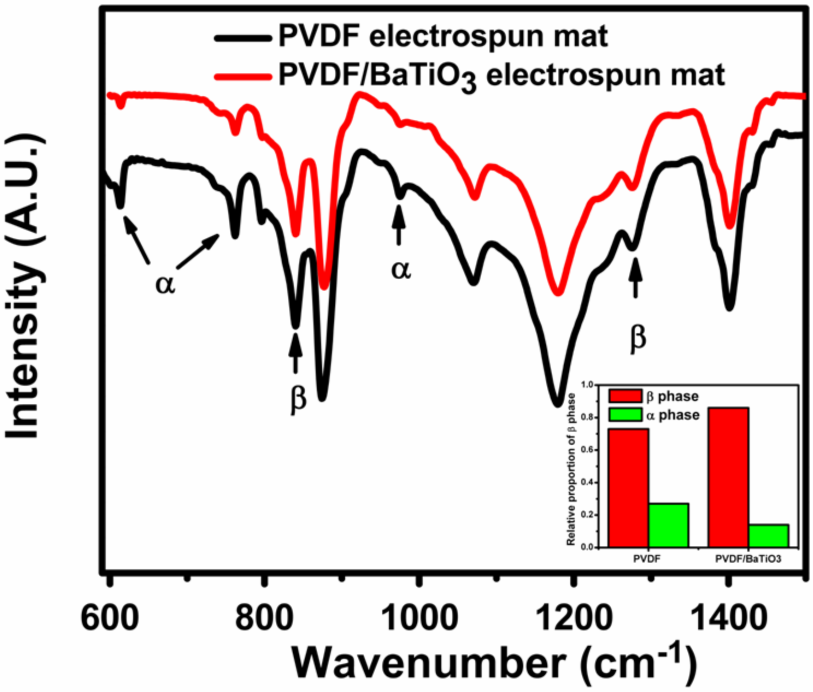

Figure 3.17: ATR-FTIR of electrospun PVDF and PVDF/$BaTiO_3$ nanocomposite.

The fraction of the β phase, $F(\beta)$ was calculated using the following equation,

$$F(\beta) = \frac{A_\beta}{1.26\,A_\alpha + A_\beta}$$

Where, A_α is the intensity of peak at 840 cm^{-1} in the FTIR spectrum and A_β is intensity of the peak at 765 cm^{-1} in the FTIR spectrum. The relative proportion of β and α phase is shown in the inset of figure .It clearly shows the $BaTiO_3$ loaded PVDF electrospun fiber contain more than 85% of electroactive β phase, whereas the neat PVDF fibers have less than 75% of β phase.

Dielectric Relaxation Study

Figure 3.18 shows the dielectric permittivity loss spectra for PVDF and PVDF/$BaTiO_3$ electrospun mats. The permittivity loss (ε'') spectra shows a relaxation peak at 10^{+07} Hz which is attributed to the glass transition temperature of PVDF [40]. A broad relaxation observed in PVDF at 10^{+00} Hz, is attributed to α phase of PVDF. However in case PVDF/$BaTiO_3$ electrospun mats this relaxation is not observed. The absence of crystalline relaxation peak is attributed to formation of the β-phase of PVDF. Thus the dielectric relaxation study further supports the formation of β-phase PVDF in presence of $BaTiO_3$ nanoparticles.

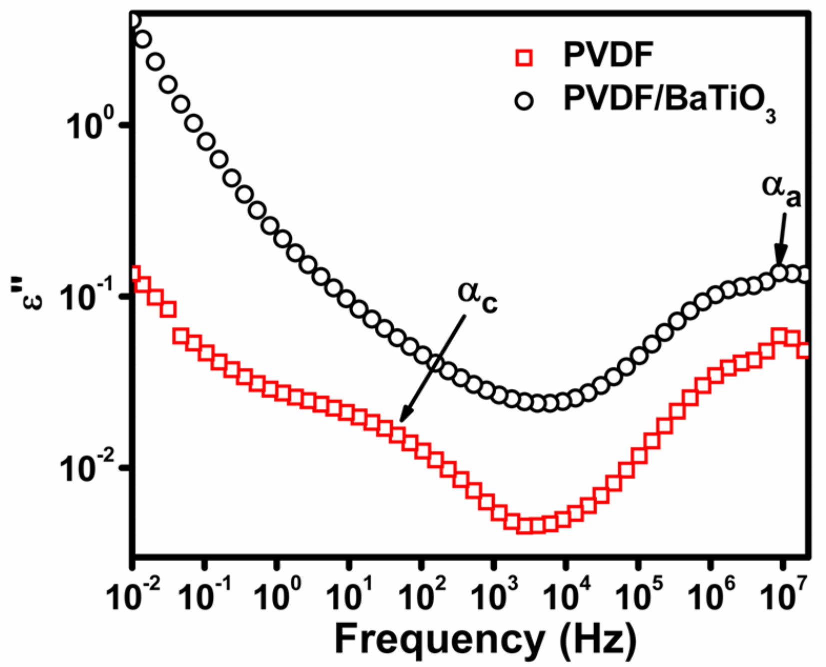

Figure 3.18: Dielectric permittivity (ε'') spectra of PVDF and PVDF/$BaTiO_3$ nanocomposites electrospun fibers.

3.II.3.3 Thermal Emissivity of PVDF/$BaTiO_3$ Nanofibers

The electrospun nanofibers were tested for low thermal emissivity application. For a comparative study, emissivity of melt pressed bulk samples of PVDF and PVDF/$BaTiO_3$ nanocomposite were also measured. Table 3.3 presents the values of emissivity for electrospun mats as well as melt pressed films of PVDF and PVDF/$BaTiO_3$ nanocomposite. The result indicates that, as compared to melt pressed films the emissivity of electrospun mat is lower in PVDF and PVDF/$BaTiO_3$ nanocomposite fibers. Secondly, the incorporation of $BaTiO_3$ in PVDF results in significantly lower values of emissivity than PVDF electrospun fibers. When the emissivity values of the electrospun fiber mats are compared it is observed that the value decreased from 0.7 for PVDF to 0.64 for the PVDF/$BaTiO_3$ mat. The decrease in the value of emissivity in PVDF/$BaTiO_3$ nanocomposite suggests presence of interfacial interactions between PVDF and $BaTiO_3$ nanoparticles [41]. Further, the reduction in emissivity can also be attributed to the non-woven porous morphology of electrospun membrane which reduces the emissivity due to internal scattering [42]. The porosity of the material cancels any emission contribution from the underlying materials due to scattering in the homogenous system.

Sr. No.	**Sample**	**Infrared Emissivity**
1.	PVDF melt pressed film	0.86
2.	PVDF/$BaTiO_3$ (5 % by wt %) melt pressed film	0.82
3.	PVDF Electrospun mat	0.7
4.	PVDF/$BaTiO_3$ (5% by wt %) Electrospun mat	0.64

Table 3.3: Infrared emissivity of Electrospun PVDF and PVDF/$BaTiO_3$ nanocomposite.

3.II.4 Conclusions

Fibers of PVDF/$BaTiO_3$ nanocomposite were prepared by electrospinning technique. The diameter of electrospun fibers was between 100-200 nm. Structural characterization of electrospun mats show that PVDF crystallized in mixed α and β phase whereas addition of $BaTiO_3$ nanoparticles to PVDF matrix was found to enhance β phase structure in PVDF as evidenced by X-ray diffraction and ATR-FTIR analysis. The dielectric relaxation spectra also supported the presence of β phase in PVDF/$BaTiO_3$ electrospun mats. Thermal emissivity of PVDF/$BaTiO_3$ electrospun mats was found to be lower than melt pressed PVDF/$BaTiO_3$ sample. In general, addition of $BaTiO_3$ has shown to enhance structural properties of PVDF.

3.II.5 References

1. Jin-Kai Yuan, Zhi-Min Dang, Sheng-Hong Yao, Jun-Wei Zha, Tao Zhou, Sheng-Tao Li, Jinbo Bai, *J. Mater. Chem.*, **2010**, 20, 2441–2447.
2. C.K. Chiang, R. Popielarz, *Ferroelectrics*, **2002**, 275, 1-9.
3. G. A. Kontos, A. L. Soulintzis, P. K. Karahaliou, G. C. Psarras, S. N. Georga, C.A. Krontiras, M. N. Pisanias, *Express polymer letters*, **2007**, 1, 781-789.
4. G. C. Psarras, K. G. Gatos, P. K. Karahaliou, S. N. Georga, C. A. Krontiras, J. Karger-Kocsis, *Express polymer letters*, **2007**, 1, 837-845.
5. H. Ishida, S. Campbell, John Blackwell, *Chem. Mater.*, **2000,** 12, 1260-1267.
6. Jr. R. Gregorio, M. Cestari, *Journal of Polymer Science: Part B: Polymer Physics*, **1994**, 32, 859-870.
7. K.P. Pramoda, A. Mohamed, In Yee Phang, L. Tianxi, *Polymer Int.* **2005**, 54, 226-232.
8. Jr. R. Gregorio, E.M. Ueno, *Journal of Material Science*, **1999**, 34, 4489-4500.
9. Rinaldo Gregorio, Jr., *Journal of Applied Polymer Science*, **2006**, 100, 3272–3279.
10. Z.M. Dang, H.Y. Wang, Y.H. Zhang, J.Q. Qi, *Molecular Rapid Communications*, **2005**, 26, 1185-1189.
11. R. Sekar., A.K. Tripathi, P. K. Pillai, *Materials Science and Engineering*, B5, **1989**, 33-36.
12. F. Kremer, *Journal of Non-crystalline solids*, **2000**, 305, 1-9.

13. H. Djidjelli, D. Benachour, A. Boukerrou, O. Zefouni, J. Martinez-Vega, J. Farenc, M. Kaci, *Express polymer letters*, **2007**, 1, 846-852.
14. N.G. McCrum, B.E. Read, G. Williams, *“Anelastic and viscoelastic behavior of polymeric solids”*, London, Wiley, (**1967**).
15. S. F. Mendes, C. M. Costa, C. Caparros, V. Sencadas, S. Lanceros-Mendez, *J Mater Sci.*, **2011**, 011, 5916.
16. S.A. Madbouly, J.A. Otaigbe, *Polymer*, **2007**, 48, 4097-4107.
17. J. Mijovic, Jo-wing Sy, T.K. Kwei, *Macromolecules*, **1997**, 30, 3042-3050.
18. L. Hongbo, Z. Xingyuan, *Journal of Macromolecular science, Part B: Physics*, **2006**, 45, 933-944.
19. A. Linares, A. Nogales, D. R. Rueda, T.A. Ezquerra, *Journal of Polymer Science: Part B: Polymer Physics*, **2007**, 45, 1653-1661.
20. Jo Wing Sy, Jovan Mijovic, *Macromolecules*, **2000**, 33, 933-946.
21. A. Bello, E. Laredo, M. Grimau, *Physical Review B*, **1999**, 60, 12764- 12774.
22. V.K. Valetine, A.M. Inna, V.M. Grigory, N.V. Gavrilov, N.P. Bessonova, *Journal of Applied Polymer Science*, **2007**, 105, 1107-1117.
23. Y. Takahashi, K. Miyaji, *Macromolecules*, **1983**, 16, 1789- 1792.
24. K. Nakagawa, Y. Ishida, *Journal of Polymer Science*, **1973**, 11, 1503-1533.
25. M. Yoshihisa, M. Hideki, A. Kenjiro, *Journal of Polymer Science: Polymer Physics*, **1980**, 18, 597- 606.
26. Y. Miyamoto, H. Miyaji, K. Asai, *Journal of Polym. Sci. Part B: Polym. Phys.*, **1980**, 18, 597606.
27. J. Mijovic, L. Hyuangki, J. Kenny, J. Mays, *Macromolecules*, **2006**, 39, 2172-2182.
28. G.M. Tsangaris, G.C. Psarras, N. Kouloumbi, *Journal of materials science*, **1998**, 33**,** 2027-2037.
29. H.W. Starkweather, P. Avikian, *Journal of Polymer Science Polymer Physics*, **1992**, 30, 637- 641.
30. I.M. Hodge, A. Eisenberg, *Journal of non-crystalline solids*, **1978**, 27, 441- 443.
31. M. Arous, B. I. Amor, A. Kallel, Z. Fakhfakh, G. Perrier, *Journal of Physics and Chemistry of Solids*, **2007**, 68, 1405-1414.
32. G.C. Psarras, E. Manolakaki, G.M. Tsangaris, *Composites: Part A*, **2003**, 34, 1187-1198.

33. H. Sasabe, S. A. Saito, H. Kakutani, *Journal of polymer science: Part A-2*, **1969**, 7, 1405-1414.
34. Y. Suzhu, P. Hing, H. Xiao, *Journal of Applied Physics*, **2000**, 88, 398-405.
35. J.H. Daly, M. J. Guest, *Journal of Materials Science Letters*, **1992**, 11, 1271-1273.
36. E. Tuncer, M. Wagener, R. Gerhard-Multhaupt, *Journal of Non-crystalline solids*, **2005**, 351, 2917-2921.
37. H. Hammamia, M. Arous, M. Lagache, A. Kallel, *Journal of Alloys and Compounds*, **2007**, 430, 1–8.
38. Ganji Zhong, Lifeng Zhang, Run Su, Ke Wang, Hao Fong, Lei Zhu, *Polymer*, **2011**, 52, 2228-2237.
39. Z.M. Huang, Y.Z. Zhang, M. Kotaki, S. Ramakrishna, *Composites science and technology*, **2003**, 63, 2223-2253.
40. C.V. Chanmal, J.P. Jog, *Express Polymer Lett.*, **2008**, 2, 294-301.
41. Z.M. Dang, H.P. Xu , H.Y. Wang, *Appl. Phys. Lett.*, **2007**, 90, 012901.
42. H. Wu, J. Fan, N.J. Du, *Appl. Polym. Sci.*, **2007**, 106,576-583.

Chapter 4

Strong Electric Field Modulation of Transport in PVDF/MWCNT Nanocomposite near the Percolation Threshold

---

This chapter describes the fabrication of PVDF/MWCNT nanocomposite thin films by pulsed laser deposition and the study of their structural and dielectric properties. The addition of MWCNT results in crystallization of PVDF into ferroelectric β phase and an enhancement in the dielectric permittivity at relatively low dielectric loss. The aspect ratio of MWCNT was found to decrease in the PLD process which effectively increases the percolation threshold in nanocomposites and allows the higher loading of MWCNTs into polymer matrix. The nanocomposites also exhibit an increase in the conductivity due to addition of MWCNT. The nanocomposites material when used as a channel layer in the field effect device architecture showed high modulation in the drain current.

Part of the work presented in this chapter has been published in following journals:

1. Chetan Chanmal, Meenal Deo, Abhimanyu Rana, Jyoti Jog, Satishchandra Ogale, *Solid State Communications,* 2011, 151, 1612–1615.
2. Chetan Chanmal, Meenal Deo, Jyoti Jog, *Applied Surface Science,* 2011, 258, 1256–1260.

4.1 Introduction

Polymer based composites with high dielectric constant and low dielectric losses are of great interest in embedded capacitor technology as they provide advantage in size and cost reduction. In this context, ferroelectric polymers have received increasing interest in recent years due to their potential applications in embedded capacitors, gate dielectrics and charge storage applications [1-3]. Generally, polymers have low dielectric permittivity and the dielectric properties of polymers can be enhanced by addition of ferroelectric nanofillers [4, 5]. However, this technique requires higher filler loading which is detrimental to the mechanical properties of the polymer. Another method of increasing dielectric permittivity which has gained significant interest is to add metallic nanofiller in the vicinity of percolation threshold [6, 7]. The dielectric permittivity in this case is found to increase by several orders of magnitude when filler loading is near to percolation threshold. One of the most studied nanofiller in this context is multiwalled carbon nanotubes (MWCNT). In case of MWCNTs, percolation threshold depends on many parameters like processing method, polymer matrix and nature of carbon nanotubes [8, 9].

Although, percolative nanocomposites exhibit a significant increase in the dielectric permittivity, there are few challenges in making these systems useful for commercial applications. First, near the percolation threshold due to increase in the conductivity, a remarkable increase in the losses are generally observed [8]. Secondly, to realize the true potential of these nanocomposites in the field of micro-electronics one needs to prepare the materials in thin film phase. Many researchers have studied the polymer based MWCNT nanocomposites in bulk and thick films [10-13].

Along these lines, in the present work we have successfully fabricated the thin films Poly (vinylidene fluoride) (PVDF)/MWCNT nanocomposite by pulsed laser deposition (PLD). PLD has an advantage over other techniques of depositing polymer composite films as it is a dry process which is also compatible with other vacuum processing methods [14, 15]. PVDF is used as a polymer matrix which is important for its ferroelectric properties. PVDF is a semi-crystalline polymer and depending on the type of conformation it exhibits five polymorphic phases, namely, *TTTT* for β phase, *TGTG*' for α and δ phases, *TTTGTTTG'* for γ and ε phases [16]. Out of these, β phase attracts maximum research and industrial interest due to its ferroelectric properties [17]. The orthorhombic β phase is normally obtained with different techniques such as mechanical stretching of PVDF, addition of clay, and poling in a strong electric field [18-21]. The specific synergistic interaction between MWCNT and PVDF is known to nucleate the β phase in solution prepared PVDF/MWCNT nanocomposites [22, 23]. Indeed, we find that incorporation of MWCNT stabilizes the important piezoelectric β-phase PVDF in our thin films even though we start with a bulk target comprising of the non-polar α-phase of PVDF. Moreover, the short interaction times and non-equilibrium conditions imposed by the PLD process are found to be useful in achieving good dispersion of the filler in the polymer matrix. Thus, detailed characterization of the nanocomposites carried out shows that MWCNTs not only help in enhancing the ferroelectric β-phase in the pulsed laser deposited polymeric film, but also provide adequate dispersion of MWCNTs leading to high values of dielectric permittivity over a broad range of frequencies.

As the fabricated nanocomposite shows a remarkable enhancement in the conductivity, these nanocomposite films were further studied for channel layer in field effect device architecture. Field effect transistor (FET) is perhaps the most significant device in any modern electronic chip architecture. Not surprisingly, there have been a large number of studies on FETs based on semiconducting and inorganic materials as transport channels over the past several decades [24-26]. With the growing emphasis on flexible electronics for novel futuristic technologies as well as to explore novel materials alternatives for non-flexible electronics, materials such as conducting and semiconducting carbon forms (CNTs, graphene) are now being actively explored [27,28]. In most such studies a thin uniform layer of a single semiconducting polymer or carbon form is used, and organic FETs (O-FET) with functionalities comparable to the established inorganic semiconductor based devices have been demonstrated [29, 30]. However, polymer based nanocomposites as a channel layer was examined only scarcely in field effect devices [31, 32]. In this work we use thin film of a functional nanocomposite comprising of a ferroelectric polymer (PVDF) and MWCNTs as an active channel layer and demonstrate that a strong electric field modulation of carrier transport can be realized therein, just below the percolation threshold.

4.2 Experimental

4.2.1 Materials

PVDF (Grade Solef 1008) obtained from Solvay, Belgium was used in this study. Multiwalled carbon nanotubes MWCNTs with (OD = 10-20 nm, ID = 5-10 nm & length = 0.5 to 200 μm) were procured from Aldrich chemicals and used without any further chemical modification. The density of MWCNT was 2.1 g cm^{-3}. The details of the properties of these materials are presented in chapter 2.

4.2.2 PLD Processing of PVDF/MWCNT Thin Films

Initially, nanocomposites of PVDF/MWCNT were prepared by melt mixing method in Haake Polylab batch mixer. The MWCNTs were mixed with PVDF pellets and fed to the batch mixer. The batch mixer was operated at a temperature of 200 °C, screw speed of 60 RPM and residence time of 5 minutes. Subsequently the pellets of the nanocomposites were prepared by hot press technique. The disk shaped pellets of PVDF/MWCNT nanocomposites were used as the targets for Pulsed Laser Deposition (PLD). In the PLD process, KrF excimer laser (λ = 248 nm, pulse width 20 ns) at an energy density of 1.5 J/cm^2 was used for ablation of polymer. The copper foil was used as a substrate in the PLD deposition. The nanocomposites were characterized for structural, morphology, dielectric and various other properties. Following table shows the sample coding and composition of PVDF/MWCNT nanocomposites. Volume percentage was calculated using the value of density of MWCNT as 2.1 g cm^{-3}.

Sample Code	Wt% loading of MWCNT	Volume% loading of MWCNT
PCNT1	1	0.84
PCNT3	3	2.55
PCNT5	5	4.27
PCNT7	7	5.99

Table 4.1: Sample codes and compositions of PLD deposited PVDF/MWCNT nanocomposites.

4.2.3 Nanocomposite Characterization

4.2.3.1 Morphology

The morphology of thin films was studied on Leica-440 Scanning Electron Microscopy (SEM). Thin layer of gold was sputtered on the samples to avoid charging effects. The FEI, TECNAI G^2 f30 was used for High Resolution Transmission Electron Microscopy (HRTEM) imaging and was operated at 300 KV. The samples for HRTEM were prepared by directly depositing PVDF/MWCNT on carbon coated copper grids by PLD. The thickness of the film for HRTEM imaging was kept around 60 nm during PLD deposition. The STM/STS measurements were carried out using variable temperature SPM system by RHK technologies, USA (SPM 100) in high vacuum conditions (better than 10^{-6} Torr).

4.2.3.2 Structural Characterization

The microstructure of the nanocomposites was evaluated by performing wide angle X-ray Diffraction experiments (WAXD) using Rigaku model Dmax 2500 X-ray diffractometer. The system consisted of X-ray source of Cu $K_{\alpha 1}$ (λ=0.154 nm) radiation operated at 40 kV and 150 mA. The Fourier transform infrared spectroscopy (ATR-FTIR) was performed using Spectrum GX Perkin Elmer spectrometer. The samples were and scanned from 4000 to 600 cm^{-1} and a total of ten scans were collected for signal averaging condition. Raman spectra of the nanocomposites were acquired using a Horiba Labram HR 800 Raman micro-spectrometer. The excitation source was He-Ne laser (632 nm) focused through a 50X objective to a spot size of approximately 2 μm, giving a power of 2 mW.

4.2.3.3 Dielectric Relaxation spectroscopy

Complex dielectric permittivity and ac conductivity measurements of PVDF and PVDF/MWCNT nanocomposites were done using Novocontrol broadband dielectric spectrometer with ZGS sample cell equipped with temperature controller and WinFit software for data analysis. The dielectric response of material was measured in the frequency range from 10 MHz to 100 Hz at 30 ± 0.01 °C by placing sample between two 20 mm gold plated electrodes. Conducting silver paste was applied on both sides to ensure good electric contacts.

4.2.4 Fabrication of PVDF/MWCNT Nanocomposite FET

The FET devices in a bottom contact configuration were fabricated on glass coated ITO substrates which also served as the gate electrodes. The gate dielectric comprising of HfO_2 was deposited by PLD process. The HfO_2 layer was grown at 300 °C by PLD and thickness was around 50 nm. The PLD deposited PVDF/MWCNT nanocomposites film was used as a channel layer in FET device configuration. The source and drain electrodes were provided by Au contacts which were deposited through shadow mask using pulsed laser deposition. The w/l ratio of the device was around 10. The schematic of the device is shown in figure 4.1.

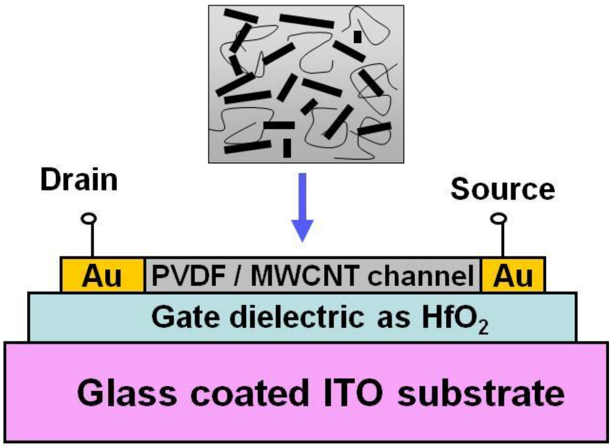

Figure 4.1: Schematic of the FET with PVDF/MWCNT nanocomposite as a channel layer.

FET device Characterization

The I-V characteristics were measured at room temperature using Keithley 2400 source meter and Keithley 6514 electrometer. The source electrode was grounded during the measurement.

4.3 Results and Discussion

4.3.1 Morphology

The SEM morphology of PLD deposited PVDF/MWCNT nanocomposites are shown in Figure 4.2. The SEM image clearly shows homogenous dispersion of MWCNTs throughout the PVDF matrix and no obvious agglomeration is observed. Dispersion of MWCNT in the polymer matrix is a critical factor for realizing the potential applications of MWCNT based polymer nanocomposites. It may be noted that, the uniform dispersion of MWCNTs is achieved without any chemical pretreatment or processing. The polar nature of the PVDF matrix possibly helps in rendering such a uniform dispersion of MWCNTs in addition to the basic homogenizing character of the PLD growth process. Moreover, a synergistic interaction between MWCNT and polymer is known to facilitate good dispersion [23]. Further, PVDF morphology in SEM shows a typical spherical nature which evidences the formation of β phase in PVDF [33].

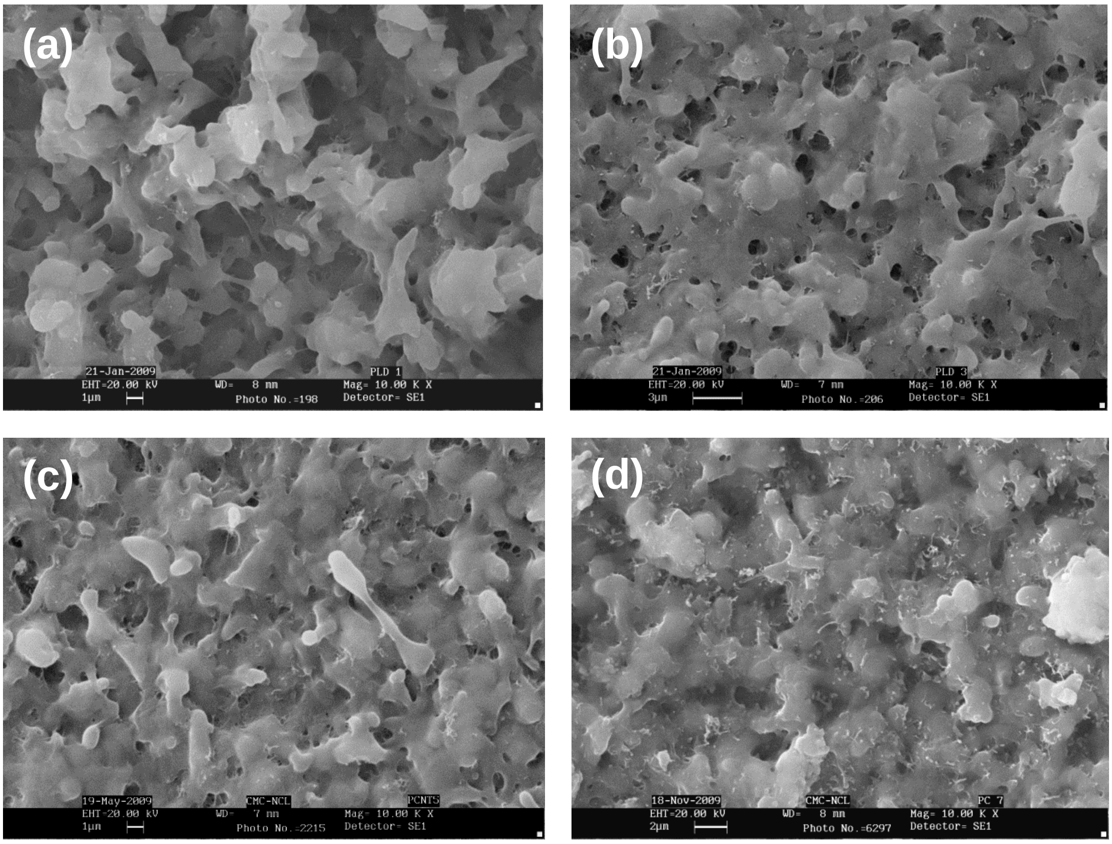

Figure 4.2: SEM micrographs of PLD deposited (a) PCNT1 (b) PCNT3 (c) PCNT5 and (d) PCNT7 nanocomposites at 10 KX magnification.

4.3.2 Structural Analysis

The effect of MWCNT on the phase structure of the PVDF was examined using XRD technique. Figure 4.3 shows the XRD patterns for the PVDF and PVDF/MWCNT nanocomposite thin films along with that for bulk PVDF. The XRD pattern of PVDF and PVDF/MWCNT nanocomposites in the bulk phase shows three characteristic diffraction peaks at $2\theta = 17.7°$, $18.4°$, and $19.9°$ which correspond to the non-polar α phase of PVDF [34]. The XRD result indicates that our target material is in non-polar α phase. The XRD pattern for PVDF thin film shows no strong peaks indicating amorphous nature of the PLD deposited PVDF thin film. Indeed this is in conformity with the earlier work that reports amorphous PVDF formation by PLD [35]. However, a fairly strong diffraction peak at $2\theta = 20.9°$ is observed in the case of PLD-PCNT7 nanocomposites film which corresponds to the unresolved (110) and (200) reflections of the polar all trans, *TTTT* sequence, corresponding to the β phase of PVDF. The XRD peaks are clearly broadened as compared to the bulk case, as expected. The XRD results suggest that MWCNT incorporation not only leads to crystallization of the PVDF film but also induces the piezoelectric β phase in PVDF.

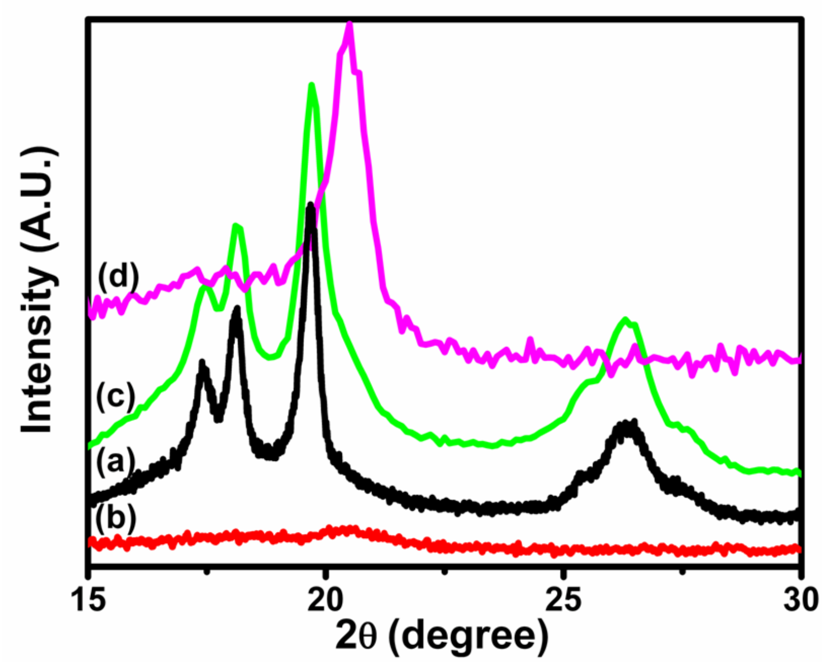

Figure 4.3: XRD patterns of (a) Bulk PLD, (b) PLD PVDF, (c) Bulk PCNT7, and (d) PLD PCNT7.

To further ascertain the phase changes in the nanocomposites, we studied the ATR-FTIR spectra of the PVDF/MWCNT thin films and the corresponding results are shown in Figure 4.4. The spectra of the bulk phase PVDF and PVDF/MWCNT nanocomposites are also shown for comparison purpose.

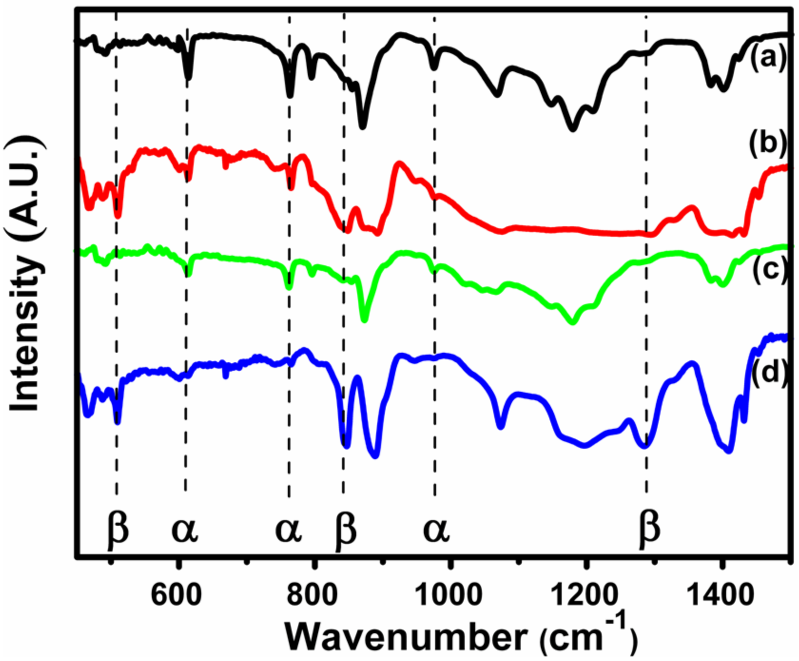

Figure 4.4: ATR-FTIR spectra of (a) Bulk PVDF (b) PLD PVDF (c) Bulk PCNT7 (d) PLD PCNT7.

Pristine PVDF shows all peaks corresponding to the α phase of PVDF. The FTIR spectra for PLD PVDF thin films show peaks at 510, 840 and 1275 cm^{-1} which correspond to the β phase of PVDF whereas the peak at 762 cm^{-1} corresponds to the α phase [36]. The peak at 840 cm^{-1} is due to the CH_2, CF_2 rocking and asymmetric stretching in β phase of PVDF. Therefore, FTIR spectra of PLD PVDF indicate that both α and β phase coexist in PLD thin film without MWCNT. It may be recalled that XRD data reflected an amorphous phase, which together with the FTIR data implies the presence of only a short range order. However, certain noticeable changes are observed in the case of PVDF/MWCNT nanocomposite thin films. First, the intensity of the peak at 1275 cm^{-1}, which is characteristic of the β phase, has increased significantly in the nanocomposite case. Secondly, the intensity of peaks at 765 cm^{-1} and 610 cm^{-1} corresponding to the α phase of PVDF, has negligible intensity in the nanocomposite case. The absence of a peak at 1233 cm^{-1}, which corresponds to the γ form, also confirms that γ phase is not present in the nanocomposites [37]. This result substantiates the presence of highly enhanced β phase component in the PVDF/MWCNT nanocomposites. The fraction of the β phase, $F(\beta)$ was calculated using the following equation,

$$F(\beta) = \frac{A_\beta}{1.26\,A_\alpha + A_\beta}$$

Where, A_α is the intensity of peak at 840 cm^{-1} in the FTIR spectrum and A_β is intensity of the peak at 765 cm^{-1} in the FTIR spectrum. The fraction of β phase, i.e. $F(\beta)$ increases to 0.7 at 1wt % loading of MWCNT to 0.81% at 7wt% loading of MWCNT. Thus the structural and morphology study shows that PLD process effectively transfer the PVDF/MWCNT onto substrate in thin film form. Further, XRD and FTIR results together indicate existence of synergic interaction between MWCNT and PVDF matrix which not only give rise to good dispersion through PLD process but helps in inducing the ferroelectric β phase in PVDF.

To further study the stability of the ferroelectric β phases, we have carried out thermal annealing studies of the PLD deposited nanocomposites. In these experiments, samples are annealed at 125 °C (below melting temperature (172 °C) but well above the glass transition temperature (−40 °C of PVDF). The XRD and FTIR spectra of samples before and after annealing are recorded. The XRD and FTIR results for PLD PCNT5 are shown in Figure 4.5 respectively.

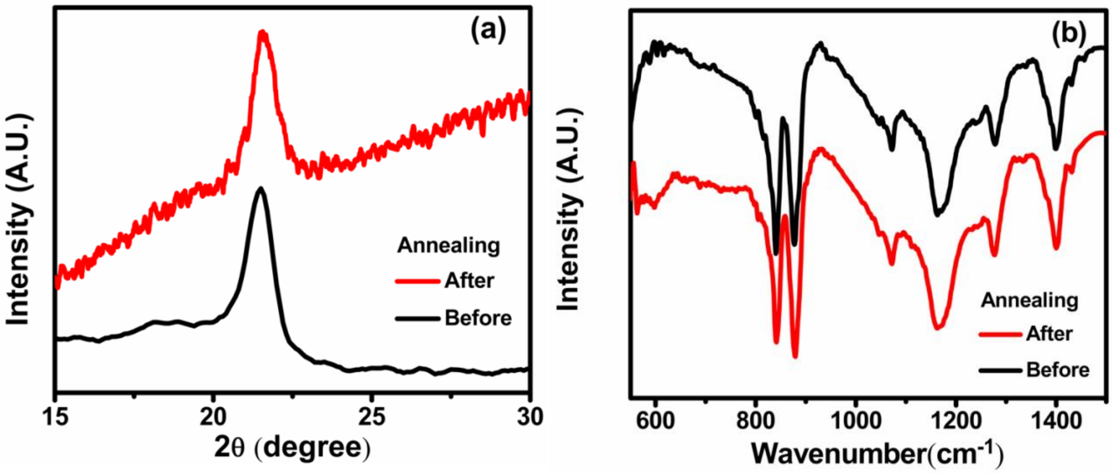

Figure 4.5: (a) XRD pattern and (b) ATR-FTIR spectra of PLD deposited PCNT5 nanocomposites before and after annealing at 172 °C.

The results of XRD and FTIR indicate that the characteristic peak positions for PLD deposited samples remain unaffected before and after annealing. This confirms that the crystalline phases are stable in the nanocomposites.

Raman Spectroscopy

Raman spectroscopy is a very sensitive tool to study the possible interactions between polymer and the MWCNT. Raman spectra of nanocomposites thin films along with pristine MWCNT were shown in Figure 4.6. The Raman spectra of both pure MWCNT and thin films of PVDF/MWCNT are similar indicating that PLD does not affects the basic structure of MWCNT. The Raman spectra show two bands at 1350 cm^{-1} (D-band) and 1580 cm^{-1} (G- band). The D band is associated with the disordered or amorphous carbon material while the G band is associated with the in-plane vibration of the sp^2-bonded carbon atoms. The peak intensity of D-band is higher than G-band which indicates great deal of amorphous carbon and impurities in the pure MWCNT. In PVDF/MWNT thin films, G-band is slightly red shifted towards higher wave number indicating interfacial interaction between MWCNT and PVDF nanocomposites [38]. The ratio of intensity of D-band to G-band is normally used to express the amount of graphitization in carbon nanotubes. In thin film PVDF/MWCNT nanocomposite films the ratio is decreased from 1.40 to 1.14. The reduction in the intensity ratio of I_d/I_g indicates that amorphous carbon material has been removed and the graphitization content of CNT has been increased during PLD process.

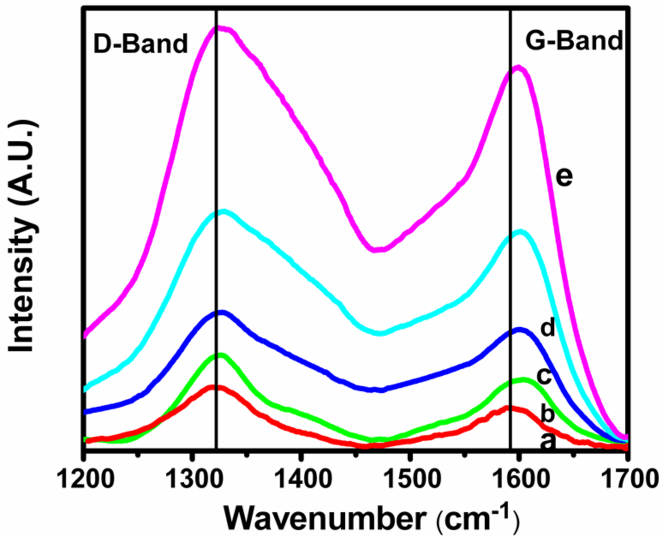

Figure 4.6: Raman spectra of (a) pristine MWCNT and PLD films of (b) PCNT1 (c) PCNT3 (d) PCNT5 and (e) PCNT7 nanocomposites.

4.3.3 TEM Analysis

The high resolution transmission electron microscopy (HRTEM) images of pristine MWCNT and MWCNT embedded in the PVDF matrix as obtained by the PLD process are shown in Figure 4.7. To obtain the latter the film was directly deposited on the TEM grid.

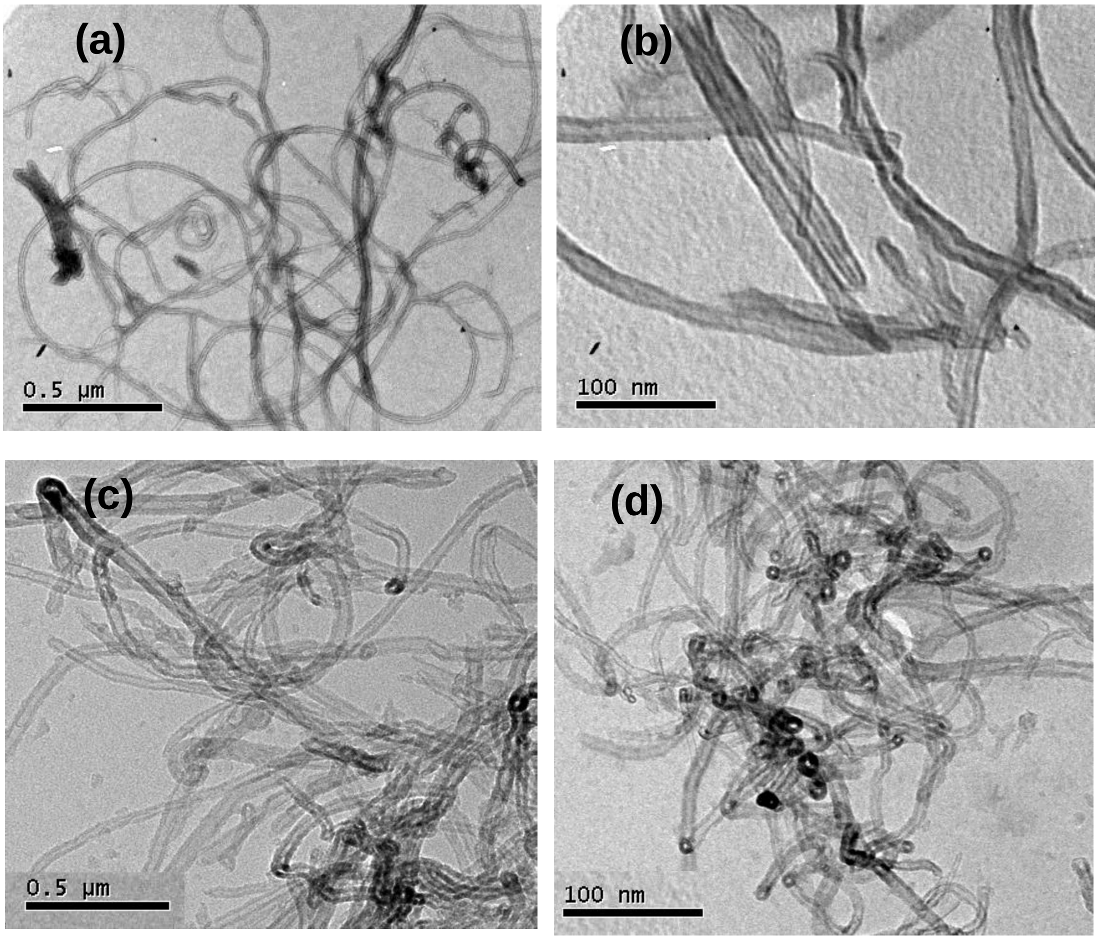

Figure 4.7: HRTEM images of (a) & (b) Pristine MWCNT and (c) & (d) PLD deposited PCNT5 nanocomposite.

The TEM morphology of pure MWCNT shows that the tubes are randomly coiled and the tube ends are not visible over the observation area whereas the tube ends are clearly visible in the case of PLD-PCNT5 nanocomposite film. Thus the HRTEM images confirm that the basic nature of MWCNT remain intact in the PLD process. However, the presence of tube ends indicates the possible breakage of MWCNTs in the PLD process which results decrease in the aspect ratio of MWCNT. It is well known that in case of MWCNT polymer nanocomposites lower aspect ratio gives rise to higher percolation threshold [39].

4.3.4 Dielectric Relaxation Spectroscopy (DRS)

The dielectric properties of nanocomposites were examined by fabricating a capacitor type of configuration. The PVDF/MWCNT thin films were deposited on copper substrate which also serves as a bottom electrode and the top contact is provided with platinum. The thickness of the film was measured using profilometer and used in the measurement of the dielectric permittivity. Figure 4.8 shows the frequency dependence of dielectric permittivity for different loading of MWCNT. The dielectric permittivity shows a composition dependent systematic increase in permittivity over the entire frequency range. The permittivity variation of PVDF/MWCNT nanocomposite films shows a behavior characteristically similar to PVDF. However, as compared to pristine PVDF, the dielectric permittivity for PCNT7 nanocomposite increases to about 560 at a frequency of 10^{+02} Hz. Importantly, dielectric permittivity of PVDF/MWCNT nanocomposite film is found to be almost independent of frequency for each composition. The observed increase in the dielectric permittivity can be ascribed to either Maxwell-Wagner-Sillars (MWS) polarization or formation of large number of minicapacitors network in nanocomposites [33, 40]. In the case of MWS polarization, charges are trapped at the interface having material with different relaxation time τ ($\tau=\varepsilon/\sigma$) arising due to difference in the dielectric permittivity and conductivity [40, 41]. This leads to enormous increase in the permittivity and strong dependence of dielectric permittivity in the low frequency region. However, in the present case the possibility of MWS polarization can be neglected due to the frequency independent nature of dielectric permittivity. It is well reported that the distribution of MWCNT within the insulating polymer matrix forms lots of minicapacitors connected in series and parallel combinations [42]. Initially, when low amount of MWCNT is added into PVDF matrix, some minicapacitors are formed resulting into slight increase in the dielectric permittivity. With the increasing loading of MWCNT, the dielectric permittivity gradually increases. As the percolation threshold approaches, there are many conducting MWCNTs wrapped with the thin layer of insulating polymer matrix forming lots of minicapacitors network. This minicapacitor network formation significantly improves the dielectric permittivity of the nanocomposites [43-45]. Thus, in the present case the significant increase in the dielectric permittivity of the PVDF/MWCNT nanocomposites can be mainly attributed to the homogenous distribution of MWCNT in the PVDF matrix and gradual formation of large number of mini-capacitor network as the MWCNT content increases.

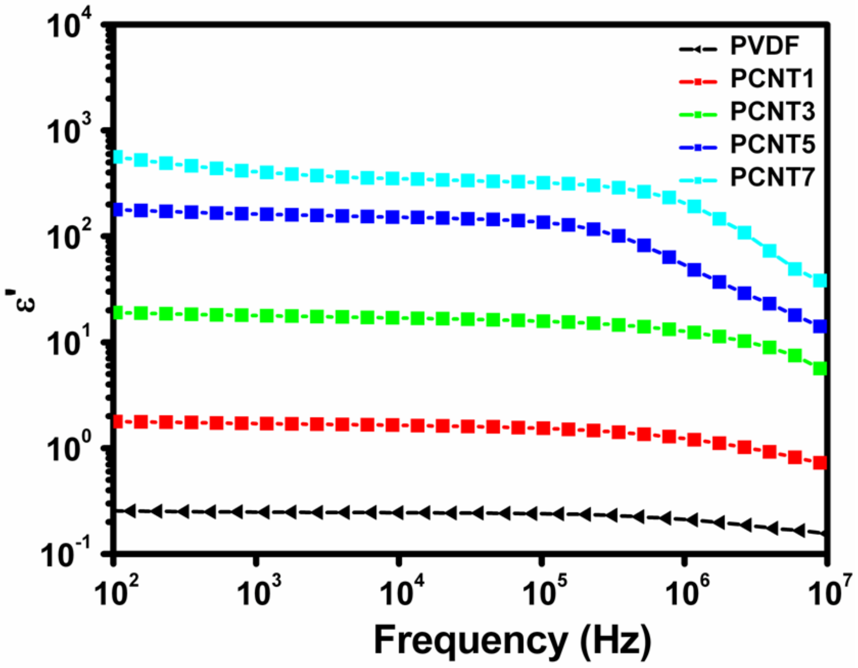

Figure 4.8: Dielectric permittivity spectra of PLD deposited PVDF and PVDF/MWCNT nanocomposites.

Figure 4.9 presents the dielectric loss (tan δ) as a function of frequency for PVDF/MWCNT nanocomposites with different loading of MWCNT. The dielectric loss spectrum shows broad relaxation around 1×10^7 Hz which corresponds to the glass transition relaxation of PVDF. The high frequency limit of the instrument constrains the full view of glass transition relaxation. From the figure 4.9 it can be also seen that dielectric loss increases with increasing filler loading. For lower loading of MWCNT, the dielectric loss spectrum is similar to PVDF and the dielectric loss values are well below 0.4 over the entire frequency range. However, a dramatic increase in the dielectric loss is observed for PCNT7 nanocomposite. The increase in the dielectric loss may be due to the increase in the electrical conductivity of nanocomposites which can be ascribed to the onset of percolation threshold in nanocomposites [46]. It has reported that, in the percolation region, the dielectric loss increases significantly with increasing filler loading [8]. The percolation threshold in bulk phase PVDF/MWCNT nanocomposites is reported to be less than 1.6 vol% loading of MWCNT [47]. In our case the percolation threshold appears at about 5.9 vol% loading of MWCNT. In case of MWCNT based nanocomposites, percolation threshold mainly depends on the aspect ratio, chirality and dispersion of MWCNT in the polymer matrix. In the present case, aspect ratio of MWCNT plays important role in the observed higher level of percolation threshold. Based on HRTEM results, it may be recalled that the MWCNT undergo scission during PLD process. Thus aspect ratio of MWCNT is reduced in the nanocomposites. This reduction in aspect ratio indeed allows higher loading of MWCNT and thus increasing dielectric permittivity at relatively lower losses. A good dispersion of MWCNT and high percolation threshold ensures control of the dielectric properties in the nanocomposites thin films. Thus PVDF/MWCNT films fabricated by PLD process exhibits remarkably enhanced dielectric permittivity and low dielectric losses.

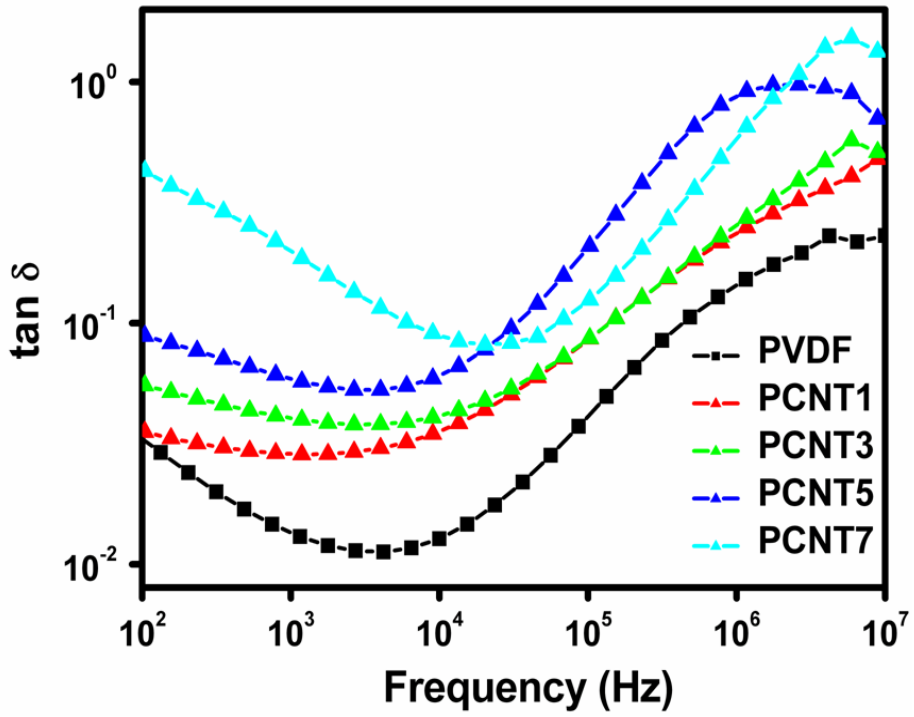

Figure 4.9: Dielectric loss spectra of PLD deposited PVDF and PVDF/MWCNT nanocomposites.

4.3.5 AC Conductivity

Figure 4.10 shows the ac conductivity of PVDF/MWCNT nanocomposite films as a function of frequency for different MWCNT loading.

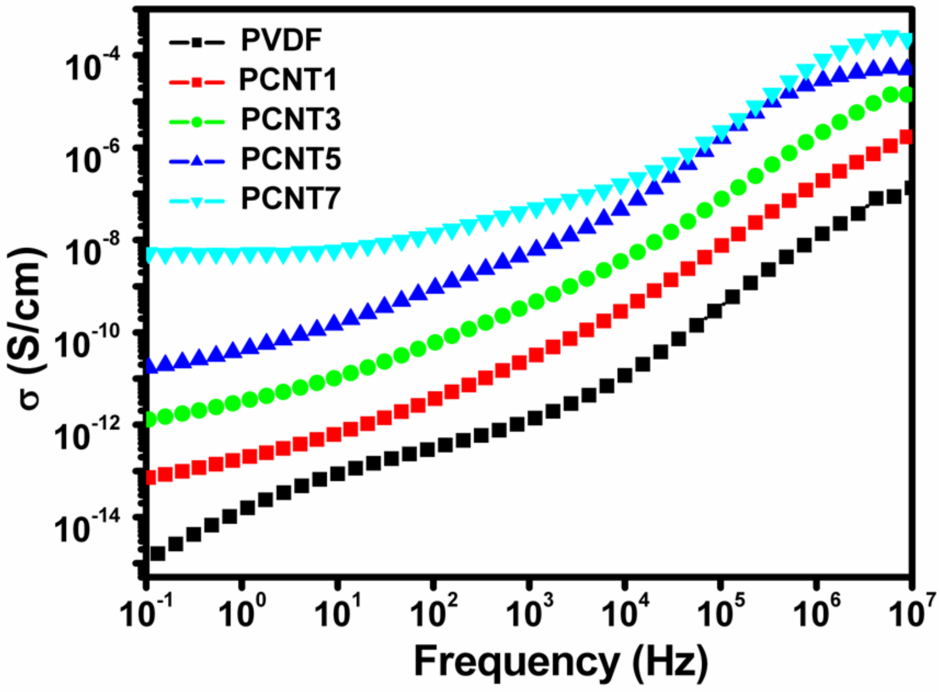

Figure 4.10: ac conductivity spectra of PLD deposited PVDF and PVDF/MWCNT nanocomposites at 10^{-01} *Hz.*

The ac conductivity spectra shows that conductivity increase with increasing loading of MWCNT. For example at 10^{-01} Hz the conductivity is 1.5×10^{-15} S/cm for PVDF which increases to 5.2×10^{-09} S/cm for PCNT7 nanocomposite. For lower loading of MWCNT (up to PCNT3) conductivity of composites increases with increasing frequency, this indicates that nanocomposites behave like electric insulators. At this loading, MWCNTs do not form electrically conductive network and they are still below the percolation threshold. However, with further increase in MWCNT loading, the conductivity shows a tendency towards frequency independent behavior in the low frequency regime indicating typical non-dielectric behavior. Particularly for PCNT7 nanocomposite, a plateau or frequency independent conductivity behavior over low frequency regime and frequency dependent conductivity at higher frequencies is clearly observed. For PCNT7 conductivity increases from 5.2×10^{-09} S/cm to 3.5×10^{-04} S/cm indicating occurrence of percolation threshold.

The frequency dependence of the real part of the conductivity near the percolation threshold is predicted to have a power-law form [48].

This behavior is generally explained by Jonscher's Universal power law,

$$\sigma\,(f) = \sigma_0 + A\,f^n$$

Where σ_0 is the dc conductivity, *A* is the pre-exponential factor and *n* is the fractional exponent between 0 and 1.This law introduces a critical frequency, f_{C} , below which the real part of conductivity is independent of frequency and identical to the dc conductivity, the conductivity mechanism being termed as "diffusive". Above fc, the conductivity increases with increasing frequency, following the power law given above, and leads to a frequency-dependent "subdiffusive" motion of mobile charges [49]. Figure 4.11 shows that the experimental data for PCNT7 nanocomposite fits fairly well to power law equation, and the value of the exponent about 0.8 which is close to the normal value of percolation theory [50].

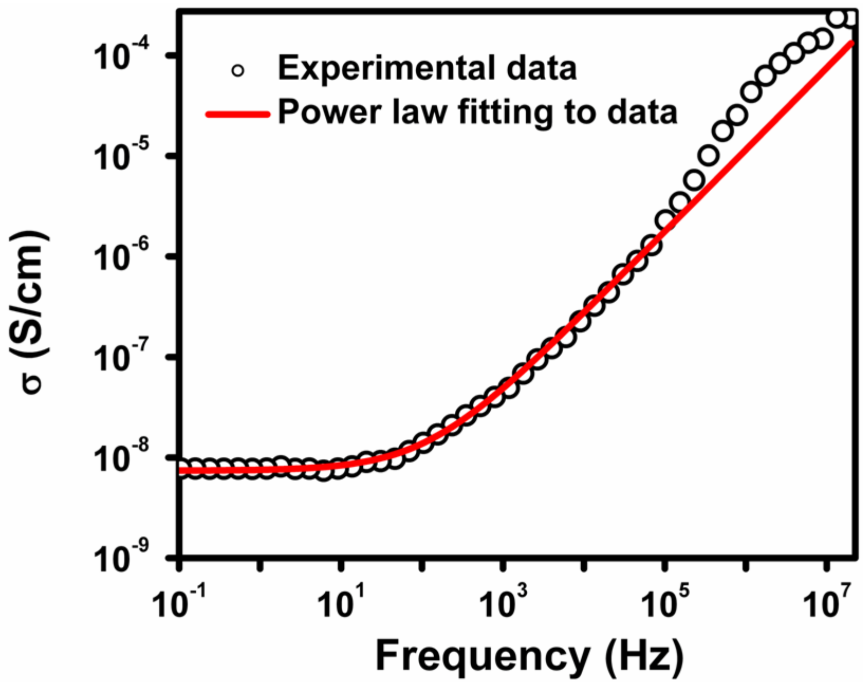

Figure 4.11: Power law fit to conductivity spectra of PLD PCNT7 nanocomposite.

Thus, the dielectric studies of PVDF/MWCNT nanocomposites shows that the enhanced value of permittivity is achieved at relatively low dielectric loss and moderate conductivity level. These results can be attributed to the increase in the percolation threshold due to the lower aspect ratio of MWCNTs in the nanocomposites [51]. The possible breakage of MWCNTs obstructs the direct physical contact between MWCNTs and therefore it is possible to have high filler loading without reaching the percolation. The results also suggest that, the ferroelectric β phase and enhanced dielectric permittivity of PVDF/MWCNT nanocomposites can be achieved without any chemical functionalization of MWCNTs. Additionally, the fabrication of the nanocomposites into thin film phase, using PLD technique, gives an excellent opportunity of exploring potential applications of nanocomposites in the field micro-electromechanical systems.

Figure 4.12 shows the variation of dielectric permittivity and loss as a function of filler loading at a frequency of 10^{+02} Hz.

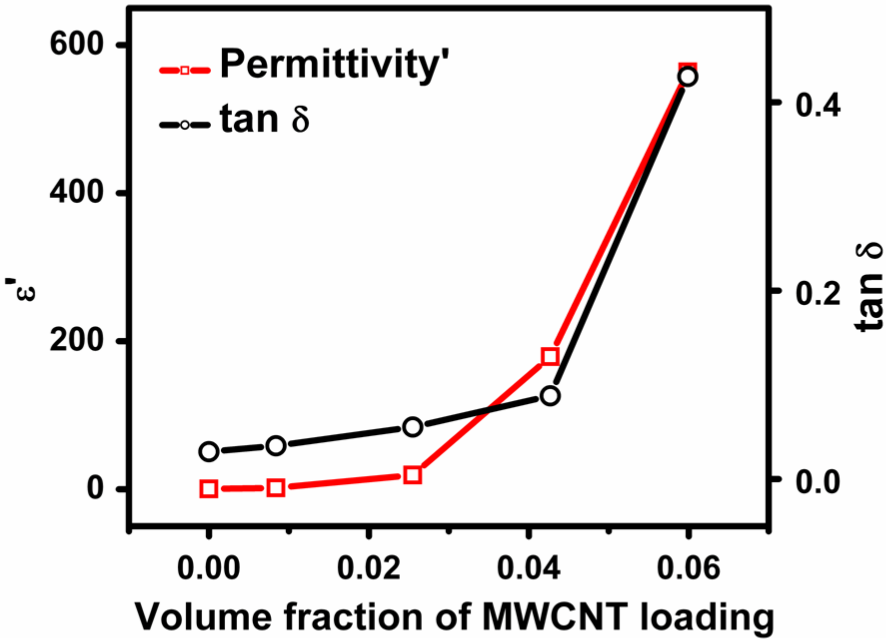

Figure 4.12: Variation in the dielectric permittivity and tanδ as a function of MWCNT loading at 10^{+02} Hz.

The dielectric permittivity is found to increase with increasing filler loading. As can be seen from the figure, a remarkable increase in the dielectric permittivity is observed for PCNT7 nanocomposites. The dielectric permittivity reaches to around 560 at this loading with loss of 0.4 and conductivity value of 3×10^{-8} S/cm, at 10^{+02} Hz.

4.3.6 I-V Characteristics

The samples for I-V measurements were prepared by fabricating capacitor type of structure with nanocomposite film embedded between two metallic electrodes. The voltage across metal electrodes is varied and current is recorded. Figure 4.13 shows the I-V characteristics of PVDF/MWCNT nanocomposites for various MWCNT concentrations. As expected, the magnitude of current increases with increasing MWCNT loading. For 3% loading of MWCNT the nanocomposite film shows a very small current whereas for 7% loading it exhibits a significant (by orders of magnitude) increase in the current. The 5% loading of MWCNT shows a moderate but definitive increase in the magnitude of current. This implies the key role of inter-MWCNT tunneling process in the PVDF matrix to be responsible for the modulation. The observed behavior can be explained using the schematic shown in the inset of Figure 4.13. At 3% MWCNT loading, the inter-MWCNT separation may be too much for tunneling to occur, while there could be conduction (or semiconduction depending on the state of MWCNT) in the 7% MWCNT content due to substantial MWCNT proximity and overlap.

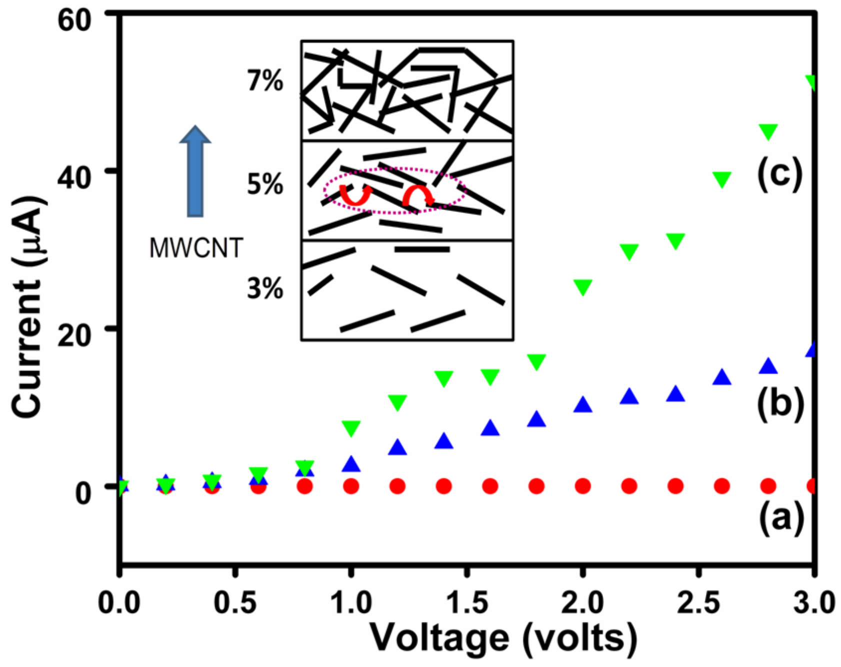

Figure 4.13: I-V characteristics of PLD deposited (a) PCNT3 (b) PCNT5 (c) PCNT7 nanocomposites.

4.3.7 Scanning Tunneling Microscopy (STM)

Scanning tunneling microscopy is important tool to study the electronic properties of materials at atomic resolution. Before discussing the corresponding device fabrication and testing, we present data on scanning tunneling microscopy and spectroscopy (STM/STS) to examine the channel in electrical terms.

The interesting MWCNT loading dependent dielectric / electrical properties of PLD PCNT5 thin films obtained in the present work were clearly judged to be promising for use as an active channel material in field-effect transistor devices. Figure 4.14(a) show the I-V curves acquired at distinct 64 equally spaced points in a scan area of 500nm × 500nm and the corresponding STM image is shown in the inset. Interestingly, all I-V curves at different points are fairly close to one another implying a fair degree of electrical homogeneity in this nanocomposite film.

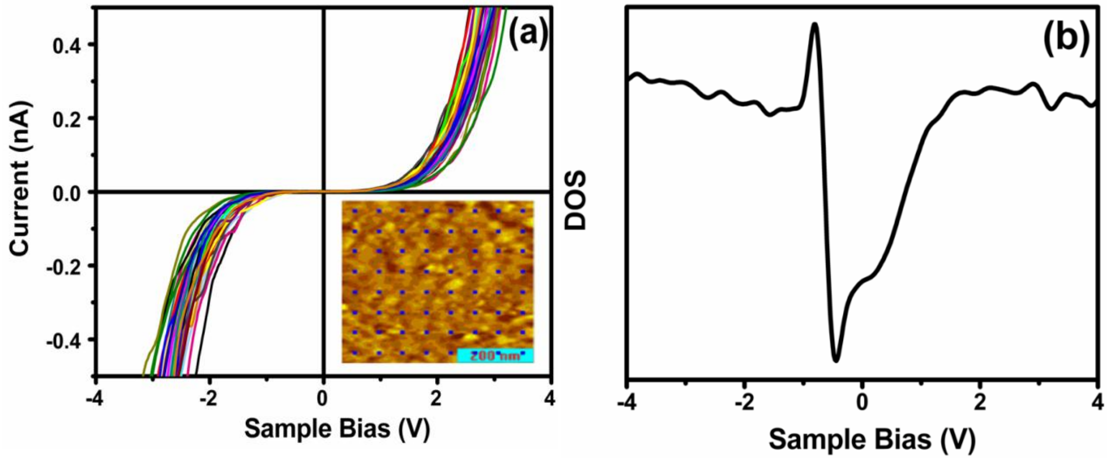

Figure 4.14: (a) I-V curves of PLD-PCNT5 thin films at 64 distinct locations obtained from STM. Inset shows the STM image with blue dots showing locations of I-V measurement (b) Localized Density of states (DOS) of PLD-PCNT5 determined from STM.

In STM, current I is recorded as a function of bias voltage V applied to the sample. The differential conductance (dI/dV) can then considered to be proportional to the Density of states (DOS) of the sample examined. Normally on semiconductor samples, $(dI/dV)/(I/V)$ is used to represent the DOS rather than the direct derivative dI/dV which is called normalization. This also accounts for the voltage dependence of the tunnel barrier at high bias. The spatial averaged density of states (DOS) shown in figure 4.14 (b) was calculated numerically from the I-V curves. The DOS data give a gap ($\Delta = V_+ - V_-$) of ~ 1.8 eV that closely matches with the gap value extracted from STM/STS techniques on single SWCNT [52, 53]. However, the gap on PVDF/MWCNT is not very sharp as seen in single CNTs and shows a band tailing in the unoccupied states, which could possibly suggest interface states at the CNT/polymer interface.

4.3.8 Field Effect Device using Nanocomposites Channel Layer

From the I-V Characteristics (shown in figure 4.13), it is clear that 5 wt% loading of MWCNT shows the moderate increase in the current. On the other hand, 3 wt% loading shows no appreciable increase in the current and 7% loading shows large increase in the current value. When the nanocomposites was used as a channel layer in field effect device, we observed that only 5% loading shows the effective modulation in the drain current whereas the 3% and 7 % loading shows less or no modulation in the current. This can be related to the conductivity level at different loading of MWCNTs. The critical level of conductivity and non-percolative network of MWCNTs at 5% loading was responsible for this observation.

The device was fabricated with PCNT5 nanocomposite as an active channel layer. The output and transfer characteristics of the PCNT5-FET are shown in Fig. 4.15 (a) and Fig. 4.15 (b), respectively. The results clearly show that the gate voltage of 4V can modulate the source-drain current by almost more than two orders of magnitude with ON/OFF ratio of around 32. In the basic I_{DS}-V_{DS} characteristic the drain current (I_{DS}) increases non-linearly with the source-drain voltage, a behavior similar to that reported in single CNT based devices [54-57]. This non-linearity in I-V characteristics is generally observed in field effect devices and has been attributed to the space charge limited current (SCLC) and electrode effects [58, 59]. In output characteristics, application of a negative gate bias (which injects holes) enhances I_{DS}, while a positive gate bias (electron injection) suppresses it. For negative gate bias, holes are accumulated at semiconductor and dielectric interface leading to an increase in the conductance, whereas for positive bias holes are depleted and conductance decreases. This implies that the majority carriers in our channel layer are holes. This can also be seen from the transfer characteristics of the device measured at V_{DS}= 5V and 10V wherein at a given V_{DS}, I_{DS} decreases with increasing gate voltage (V_G), a sign of a p-type material [60, 61].

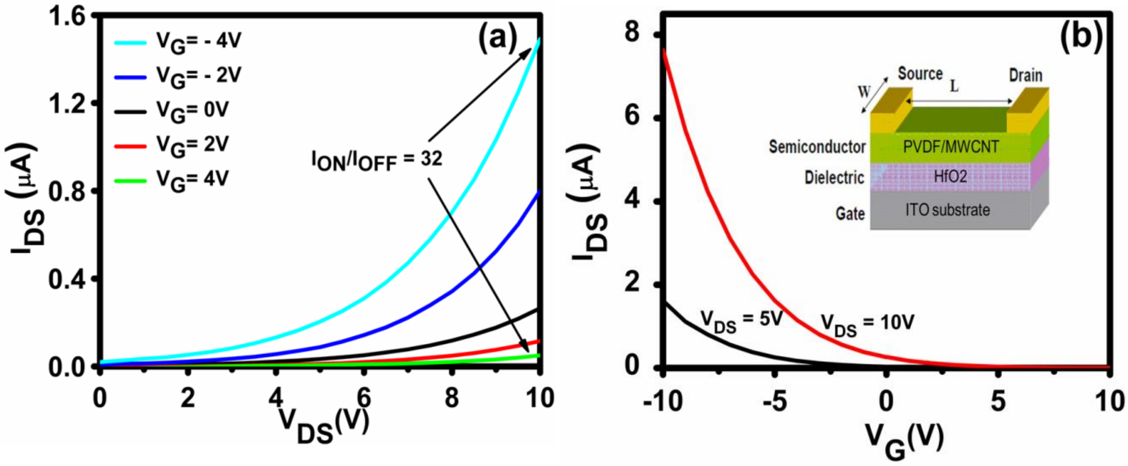

Figure 4.15: (a) Output Characteristics and (b) transfer characteristics of PCNT5 nanocomposites FET device.

A non-percolating network of nanotubes embedded in the PVDF matrix represents an interesting and unique channel layer in many ways in so far as an FET device action is concerned. A schematic of such assembly in an FET configuration is shown in inset of Figure 4.16. The intertwined yet electronically separated conducting or semiconducting nanotubes provide the transport channel within the PVDF matrix. The external field applied at electrodes is responsible for the injection of charge carriers in the channel and the inter-MWCNT tunneling process in the PVDF matrix (with enhanced piezoelectric β-phase contribution) are responsible for observed modulation.

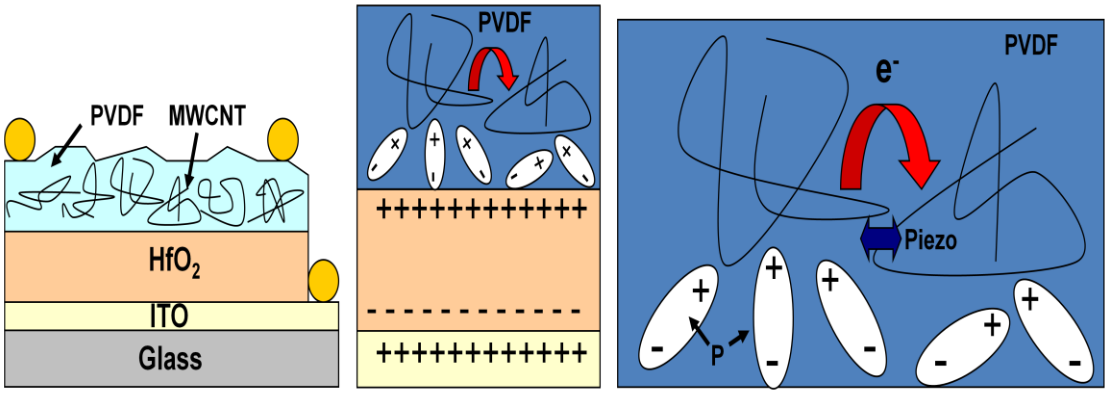

Figure 4.16: Schematic showing of FET device action in PVDF/MWCNT nanocomposite as a channel layer.

4.4 Conclusions

In conclusion, we have fabricated thin films of PVDF/MWCNT nanocomposite by pulsed laser deposition. Interestingly the addition of MWCNTs renders crystallinity to the polymeric film and also induces the ferroelectric β phase of PVDF. The dielectric permittivity of nanocomposites increases with increasing loading of MWCNT at relatively low dielectric losses. The enhanced dielectric permittivity was explained on the basis of formation minicapacitor network in nanocomposites. The control over the dielectric properties obtained through higher percolation threshold offers use of these nanocomposites in various applications. The fabricated PVDF/MWCNT nanocomposite films were used in an electric field modulation device. When used as a channel layer in a field effect transistor configuration, a strong electric field modulation of the transport was realized just below the percolation threshold. The nanocomposite film with MWCNT content just below the percolation threshold shows strong modulation of drain current with gate voltage. The output and transfer characteristics show that the PVDF/MWCNT nanocomposite channel exhibits p-type behavior. We believe that, the idea of the use of nanocomposite non-percolating channel concept can provide several opportunities for FET devices for organic electronics.

4.5 References

1. L. Qi, B. I. Lee, S. Chen, W. D. Samuels, G. J. Exarhos, *Adv. Mater.,* **2005**, 17, 1777-1781.
2. P. Kim, N. M. Doss, J. P. Tillotson, P. J. Hotchkiss, M. J. Pan, S. R. Marder, J. Li, J. P. Calame, J. W. Perry, *ACS Nano*, **2009**, 3, 2581-2592.
3. S. Han, X. liu, J.P. Han, C. Zhou, *Appl. Phys. A*, **2003**, 77, 873–875.
4. C. V. Chanmal, J.P. Jog, *eXpress polymer letters*, **2008**, 2, 294-301.
5. P.Kim, N.M. Doss, J.P.Tillotson, P. J. Hotchkiss, M.J.Pan, S.R. Marder, J. Li, J.P. Calame, J.W. Perry, *ACS Nano*, **2009**, 3, 2581-2592.
6. Maheswar Panda, V. Srinivas, A. K. Thakur, *Appl. Phys. Lett.,* **2008,** 93, 242908.
7. Yun-Jia Li, Man Xu, Jun-Qiang Feng, Zhi-Min Dang, *Appl. Phys. Lett.*, **2006**, 89, 072902.
8. C.W. Nan, Y. Shen, Jing Ma, *Annu. Rev. Mater. Res.*, **2010**, 40, 131–151.

9. Michele T. Byrne, Yurii K. Gun'ko, *Adv. Mater.*, **2010**, 22, 1672–1688.
10. S. Manna, A. K. Nandi, *J. Phys. Chem. C.*, **2007**, 111, 14670-14680.
11. Z.M. Dang, S. H. Yao, H. P. Xu, *Appl. Phys. Lett.*, **2007**, 90,012907.
12. R. H. Schmidt, I. A. Kinloch, A. N. Burgess, A. H. Windle, *Langmuir*, **2007**, 23, 5707-5712.
13. D. Chen, M. Wang, W.D. Zhang, T. Liu, *J. Applied Polymer Science*, **2009**, 113, 644-650.
14. D.B.Chrisey, A. Pique, R.A. McGill, J.S. Horwitz, B.R. Ringeisen, D.M. Bubb, P.K.Wu, *Chem. Rev.*, **2003**, 103, 553-576.
15. J. Faupel, C. Fuhse, A. Meschede, C. Herweg, H.U. Krebs, S. Vitta, *Appl. Phys. A*, **2004**, 79, 1233-1235.
16. R. Gregorio Jr., M. Cestari, *J. Polym. Sci.: Part B: Polym. Phys.*, **1994**, 32, 859-870.
17. A. J. Lovinger, *Science*, **1983**, 220, 1115–1121.
18. L. Priya, J.P. Jog, *J. Polym. Sci.: Part B: Polym. Phys.*, **2002**, 40, 1682-1689.
19. R. P. Vijayakumar, D. V. Khakhar, A. Misra, *J. Appl. Polym. Sci.*, **2010**, 117, 3491-3497.
20. S. L. Hsu, F. J. Lu, D. A. Waldman, M. Muthukumar, *Macromolecules*, **1985**, 18, 2583-2587.
21. V. Sencadas, S. L. Mendez, J. F. Mano, *Thermochimica Acta*, **2004**, 424, 201–207.
22. S. Yu, W. Zheng, W. Yu, Y. Zhang, Q. Jiang, Z. Zhao, *Macromolecules*, **2009**, 42, 8870-8874.
23. S. Huang, W.A. Yee, W.C. Tjiu, Y. Liu, M. Kotaki, Y.C.F. Boey, J. Ma, T. Liu, X.Lu, *Langmuir*, **2008**, 24, 13621-13626.
24. M. Muccini, *Nature Mater.*, **2006**, 5, 605.
25. E. Menard, V. Podzorov, S.H. Hur, A. Gaur, M.E. Gershenson, J.A. Ogers, *Adv. Mater.*, **2004**, 16, 2097.
26. S. B. Ogale, V. Talyansky, C. H. Chen, R. Ramesh, R. L. Greene, T. Venkatesan, *Phys. Rev. Lett.*, **1996**, 77 1159.
27. Q. Cao, J.A. Rogers, *Adv. Mater.*, **2009**, 21, 29.
28. Q. Cao, S. Hur, Z. Zhu, Y. Sun, C. Wang, M.A. Meitl, M. Shim, J.A. Rogers, *Adv. Mater.*, **2006**, 18, 304.

29. C.F. Sung, D. Kekuda, L.F. Chu, Y.Z. Lee, F.C. Chen, M.C. Wu, C.W. Chu, *Adv. Mater.,* **2009**, 21, 1.
30. R.T. Weitz, U.Zchieschang, F. Effenberger, H. Klauk, M.Burghard, K.Kern, *Nano Lett.,* **2007**, 7, 22.
31. G. Eda , M.Chhowalla, *Nano lett.,* **2009**, 9, 814.
32. Y. Jang, W.H. Lee, Y.D. Park, D. Kwak, J.H. Cho, K. Cho, *Appl. Phys. Lett.,* **2009**, 94, 183301.
33. Q. Chen, P. Du, L. Jin, W. Weng, G. Han, *Appl. Phys. Lett.,* **2007**, 91, 022912.
34. W.A. Yee, M. Kotaki, Y. Liu, X. Lu, *Polymer,* **2007**, 48, 512-521.
35. M.G. Norton, W. Jiang, J. T. Dickinson, K.W. Hipps, *Appl. Surf. Sci.,* **1996**, 96, 617-620.
36. M. Kobayashi, K. Tashiro, H. Tadokoro, *Macromolecules,* **1975**, 8, 158-171.
37. M.Benz, W.B.Euler, *J. App. Polym.Sci.,* **2003**, 89, 1093-1100.
38. Guang Xin Chen, Yongjin Li, Hiroshi Shimizu, *Carbon*, **2007**, 45, 2334-2340.
39. S.H. Yao, Z.M. Dang, M.J. Jiang, H.P. Xu, J. Bai, *Appl. Phys. Lett.,* **2007**, 91, 212901.
40. F. He, S. Lau, H. L. Chan, J. Fan, *Adv. Mater.,* **2009**, 21, 710-715.
41. R. Tamura, E. Lim, T. Manaka, M. Iwamoto, *J. Appl. Phys.,* **2006**, 100, 114515.
42. Qun Li, Qingzhong Xue, Lanzhong Hao, Xili Gao, Qingbin Zheng, *Composites Science and Technology*, **2008**, 68, 2290–2296.
43. R. Simoes, J. Silva, R. Vaia, V. Sencadas, P. Costa, J. Gomes, S. L. Mendez, *Nanotechnology,* **2009**, 20, 035703.
44. S. H. Yao, Z.M. Dang, H.P. Xu, M.J. Jiang, J. Bai, *Appl. Phys. Lett.,* **2008**, 92, 082902.
45. J.K. Yuan, S.H. Yao, Z.M. Dang, A. Sylvestre, M. Genestoux, J Bai, *J. Phys. Chem. C.,* **2011**, 115, 5515-5521.
46. Z.M. Dang, L. Wang, V. Yin, Q. Zhang, Q. Lei, *Adv. Mater.,* **2007**, 19, 852-857.
47. L. Wang, Z.M. Dang, *Appl. Phys. Lett.,* **2005**, 87, 042903.
48. A. Linares, J. C. Canalda, M. E. Cagiao, M. C. G. Gutierrez, A. Nogales, I. M. Gullon, J. Vera, T. A. Ezquerra, *Macromolecules,* **2008**, 41, 7090-7097.
49. B. Roling, *Dielectrics Newsletter,* **2002**, Issue 17, 1.
50. Jin-Kai Yuan, Zhi-Min Dang, Sheng-Hong Yao, Jun-Wei Zha, Tao Zhou, Sheng-Tao Lib and Jinbo Bai, *J. Mater. Chem.*, **2010**, 20, 2441–2447.

51. P. Costa, J. Silva, V. Sencadas, C. M. Costa, F. W. J. hattum, J. G. Rocha, S.L. Mendez, *Carbon*, **2009**, 47, 2590-2599.
52. J.W.G. Wildoer, L.C. Venema, A.G. Rinzler, R.E. Smalley, C. Dekker, *Nature,* **1998**, 391, 59.
53. T. W. Odom, J. Huang, P.Kim, C.M. Lieber, *Nature,* **1998**, 391, 62.
54. J. Vaillancourt, H. Zhang, P. Vasinajindakaw, H. Xia, X. Lu, X. Han, D. C. Janzen, W.S. Shih, C.S. Jones, M. Stroder, M. Y. Chen, H. Subbaraman, R. T. Chen, U. Berger, M. Renn, *Appl. Phys. Lett.*, **2008**, 93, 243301.
55. S.J. Tans, A. Verschueren, C. Dekker, *Nature*, **1998**, 393, 49.
56. K. Maehashi, T. Katsura, K. Kerman, Y. Takamura, K. Matsumoto, E. Tamiya, *Anal. Chem.*, **2007**, 79, 782.
57. E. G. Espino, G. Sala, F. Pino, N. Halonen, J. Luomahaara, J, Maklin, G. Toth, K. Kordas, H. Jantunen, M. Terrones, P. Helisto, H. Seppa, P.M. Ajayan, R. Vajtai, *Nano*, **2010**, 6 ,3318.
58. T. Hirose, T. Nagase, T. Kobayashi, R. Ueda, A. Otomo, H. Naito, *Appl. Phys. Lett.*, **2010**, 97, 083301.
59. T. Hou, J. Han, T. Yamda, P. Nguyen, Y. P. Chen, M. Meyyappan, *Nano Lett.*, **2004**, 4 1247.
60. E. Artukovic, M. Kaempgen, D.S. Hecht, S. Roth, G. Gruner, *Nano Lett.*, **2005**, 5, 75.
61. J. Zhang, P.C. Chen, G. Shen, J. He, A. Kumbhar, C. Zhou, J. Fang, *Angew. Chem. Int. Ed.*, **2008**, 47, 9469.

Chapter 5

Nonvolatile Memory and Infrared (IR) Sensor based on PVDF/Clay Nanocomposites

This chapter presents the dielectric characterization of PVDF/Clay nanocomposites and demonstrate its application as a gate dielectric material in field effect transistor. The nanocomposites exhibit significant enhancement in the dielectric permittivity which is attributed to the strong interfacial interaction between polymer matrix and clay platelets. The nanocomposite material was directly integrated in FET device architecture. The nanocomposite gate dielectric FET shows excellent transistor performance along with excellent memory retention characteristics and infrared (IR) sensing capability due to the ferroelectric and pyroelectric properties of gate dielectric.

Part of the work presented in this chapter has been published in following journals:

1. C. V. Chanmal, J. P. Jog, *e-Polymers*,2009, no. 112.

Section I: Dielectric Studies of PVDF/Clay Nanocomposites

5.I.1 Introduction

Electroactive polymers play an important role in many fields like micro-electronic-mechanical systems (MEMs), gate dielectric material, embedded capacitor application and energy storage. For such applications, materials with high electric energy storage density are required which can be achieved by increasing the dielectric permittivity of material [1]. Polymer based nanocomposite materials with high dielectric permittivity were been studied extensively as a potential candidate for such applications [2-4]. The most popular approach to increase the dielectric permittivity of the polymer is by incorporating inorganic ferroelectric metal oxides such as Lead Zirconium Titanate (PZT), Barium Titanate ($BaTiO_3$) etc. [5-7]. However, a very high loading up to 50% by volume were generally required to achieve desired enhancement in permittivity. Also, the large difference between the two phases can give rise to highly inhomogenous electric fields. Till date, nanofillers such as $BaTiO_3$ and multiwalled carbon nanotubes (MWCNT) are reported to result in improved dielectric permittivity without compromising the flexibility of the polymer [8, 9]. Another approach which recently gained significant research interest is the effect of clay addition on the dielectric properties of polymer. Polymer clay nanocomposites represent a new class of materials based on reinforcement of polymer chain by dispersion of nano-scale clay particles [10]. Thus from fundamental point of view, polymer/clay nanocomposites serve as model systems to study the confinement effect on various properties of polymers [11]. Dielectric spectroscopy is indeed found to be an excellent tool to understand the confinement effects in these systems.

In this chapter we discuss the effect of different content of clay on the dielectric permittivity and relaxation dynamics of PVDF. As reported by Priya and Jog, it was observed that presence of clay transforms the PVDF into ferroelectric β phase [12]. They observed that melt processing of PVDF/clay nanocomposites results into the formation of β phase instead of α phase. It was suggested that, the close matching of crystal lattice of clay with that of the β phase of PVDF is probably responsible for the crystallization and stabilization of β phase. The earlier studies on PVDF/Clay nanocomposites showed increase in the melting temperature (6 °C to 8 °C) and crystallization (10 °C to 12 °C) temperature of PVDF. The storage modulus was also found to increase significantly with the addition of clay. In this context it is interesting to study the effect of clay on the dielectric properties of PVDF.

5.I.2 Experimental

5.I.2.1 Materials and Processing of Nanocomposites

Polyvinylidene fluoride (PVDF) grade Solef 1008, supplied by Solvay (Belgium) is used for the present study. The organically modified bentonite clay sample used in the present study is Cloisite 20A procured from southern clay products (United States). Nanocomposites of PVDF with 20A were prepared with 1.5, 3, 5, 7, and 10% of clay loading on twin-screw extruder. The films of polymer/clay nanocomposites for dielectric spectroscopy analysis were prepared by compression molding at a temperature of 200 °C using Carver press model F-15181.

5.I.2.2 Nanocomposite Characterization

X-ray diffraction (XRD)

The structure of PVDF/Clay nanocomposite is investigated using Rigaku X-ray diffractometer with Cu $K_{\alpha 1}$ (λ=0.154nm) radiation operated at 40 kV and 150 mA. The samples are scanned in the 2θ range of 10 to 60 degrees with scan rate at 4 degrees per minute.

Dielectric Relaxation Spectroscopy (DRS)

Dielectric measurements of PVDF and PVDF/clay nanocomposites were carried out over broad frequency range (i.e.1×10^{-02} - $2 \times 10^{+07}$ Hz) at different constant temperatures using Novocontrol broadband dielectric spectrometer equipped with ZGS active sample cell. The temperature sweep is carried out in the range of 30 °C to 150 °C by placing sample between two 20 mm gold plated electrodes. The sample temperature was stable within less than ±0.1 °K. Quick drying silver paste is used to ensure good electrical contact.

Scanning Electron microscopy (SEM)

The morphology of thin films was studied on Leica-440 Scanning Electron Microscopy (SEM). Thin layer of gold was sputtered on the samples to avoid charging effects.

5.I.3 Results and Discussion

5.I.3.1 Structural Analysis

Figure 5.1 (a) shows XRD results of PVDF/Clay nanocomposites. The XRD pattern of pristine PVDF shows characteristic peaks at 18.1°, 18.7°, 20.1° and 26.8° which corresponds to the (100), (020), (110), and (021) of α phase PVDF [13]. On the other hand, for PVDF/clay nanocomposites only a single peak at 20.6° corresponding to the (110) / (200) planes of β phase crystallization of PVDF can be observed. The XRD pattern for 1.5 wt% of clay content shows a shoulder of α phase PVDF with strong peak of β phase. With increasing content of clay increases the β content while depressing the α phase substantially. Moreover, the full width at half maximum of characteristic peaks increases with increasing clay loading which indicates the decrease in crystallite size with clay loading. Thus, XRD analysis clearly reveals the enhancement of β phase PVDF in nanocomposites. Figure 5.1 (b) shows FTIR spectra of PVDF/Clay nanocomposites. The FTIR spectra also show the β phase enhancement in nanocomposites.

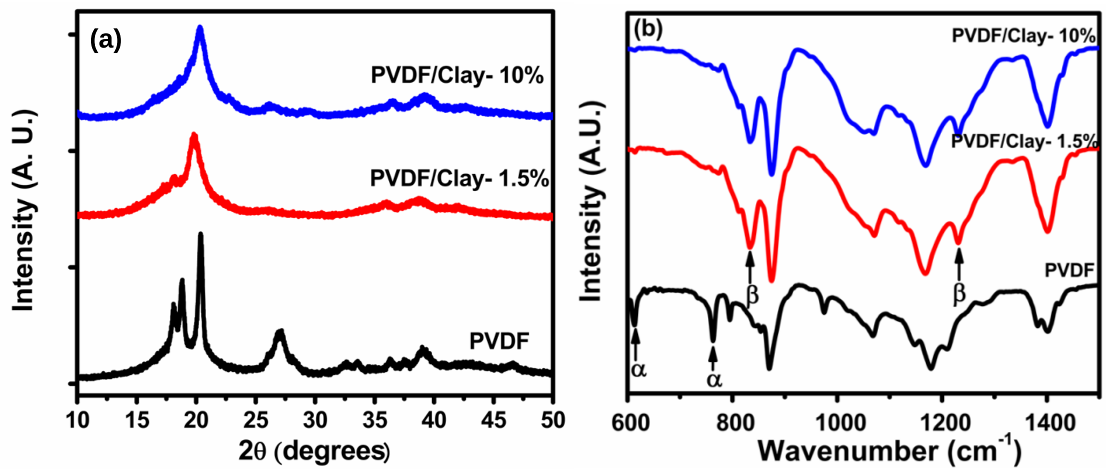

Figure 5.1: (a) XRD and (b) ATR-FTIR pattern of PVDF and PVDF/Clay nanocomposites.

The fraction of the β phase, $F(\beta)$ was calculated using the following equation,

$$F(\beta) = \frac{A_\beta}{1.26\, A_\alpha + A_\beta}$$

Where, A_α is the intensity of peak at 840 cm^{-1} in the FTIR spectrum and A_β is intensity of the peak at 765 cm^{-1} in the FTIR spectrum. The fraction of β phase, i.e.$F(\beta)$, for different clay loading is presented in table 5.1.

Sample	Clay content (%)	F(β)
PVDF	0	0.03
PVDF/Clay-1.5%	1.5	0.84
PVDF/Clay-5%	5	0.85
PVDF/Clay-7%	7	0.88
PVDF/Clay-10%	10	0.90

Table 5.1: Fraction of β phase i.e. F(β) for PVDF and PVDF/Clay nanocomposites.

5.I.3.2 Dielectric Studies

Figure 5.2 shows a plot of frequency dependence of dielectric permittivity (ε') for PVDF/Clay nanocomposites at 30 °C. The dielectric permittivity increases with increasing clay loading over the entire frequency range of measurement. For example, the dielectric permittivity at a frequency of 10^{-02} Hz increased from 12 for pristine PVDF to about 165 for 10% clay content in the nanocomposites. The dielectric permittivity at lower frequency is always greater than the higher frequency, which indicates the higher electric polarization at lower frequency, because at lower frequency dipoles get enough time to get oriented in the direction of applied field. The increase in the permittivity with increasing clay loading, particularly in the low frequency region, can be attributed to the interfacial polarization operative in low frequency end of spectrum. In polymers and composites, interfacial polarization is present due to the difference in the permittivity values of the filler and polymer matrix and such interface can lead to increase in dielectric permittivity, particularly in low frequency region.

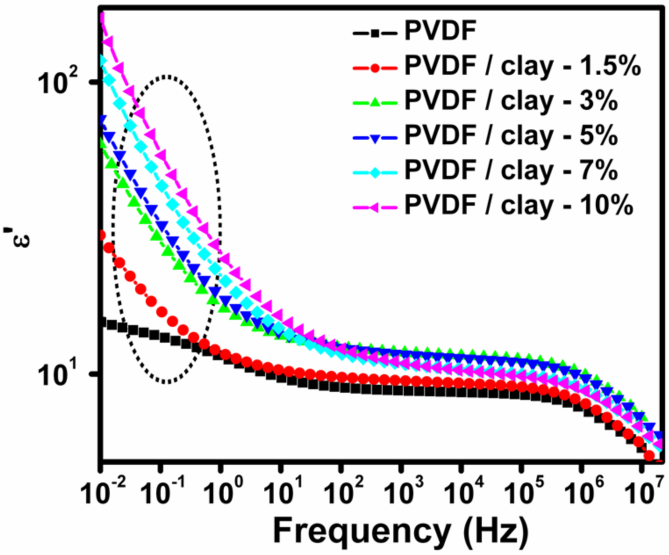

Figure 5.2: Frequency dependence of dielectric permittivity (ε') curves for PVDF and PVDF/clay nanocomposites.

The dielectric permittivity of the composites can be predicted using logarithmic model based on effective medium theory [14-16]. According to the logarithmic model, effective dielectric permittivity of the composite can be calculated by using the following equation,

$$\log \varepsilon'_{composite} = \emptyset_{filler} \ \log \left[\frac{\varepsilon'_{filler}}{\varepsilon'_{polymer}} \right] + \log \varepsilon'_{polymer}$$

This model predicts that in the absence of interfacial polarization, the dielectric permittivity of composites ($\varepsilon'_{composite}$) is linearly proportional to volume fraction of filler (ϕ_{filler}) [17, 18]. The dielectric permittivity of organically modified clay pellet is measured over the frequency range and the value of dielectric permittivity (40000) at a frequency of 0.01 Hz is used for the calculations. Figure 5.3 compares the dielectric permittivity PVDF/clay nanocomposites as a function of clay loading at 0.01 Hz. As shown in figure 5.3, the calculated values of permittivity using the logarithmic model increased from 12 (for PVDF) to 20 (for 10 wt% of clay loading) in PVDF/clay nanocomposites. However, the experimental values of the dielectric permittivity in PVDF/clay nanocomposites are found to increase from 12 (for PVDF) to 165 (for 10 wt% of clay loading). This result indicates that PVDF/clay nanocomposites does not obey simple logarithmic relation and higher values of permittivity in nanocomposites could be attributed to the presence of interfacial interaction between PVDF/clay nanocomposites.

In order to account for the contribution of the interface towards the permittivity of the nanocomposites, the data was further analyzed using a three phase model developed by Vo and Shi [19]. According to Vo and Shi model, the effective dielectric permittivity in nanocomposites can be given by following equation,

$$\varepsilon_c = \frac{h+2l}{h-l}$$

Where,

$$h = 1 + 2\frac{(\varepsilon_3 - \varepsilon_2)(\varepsilon_2 - \varepsilon_1)}{(2\varepsilon_3 + \varepsilon_2)(2\varepsilon_2 + \varepsilon_1)}\frac{a^3}{b^3} - 2\frac{(\varepsilon_3 - 1)(\varepsilon_3 - \varepsilon_2)}{(\varepsilon_3 + 2)(2\varepsilon_3 + \varepsilon_2)}\frac{b^3}{c^3} - 2\frac{(\varepsilon_3 - 1)(\varepsilon_3 + 2\varepsilon_2)(\varepsilon_2 - \varepsilon_1)}{(\varepsilon_3 + 2)(2\varepsilon_3 + \varepsilon_2)(2\varepsilon_2 + \varepsilon_1)}\frac{a^3}{c^3}$$

$$l = \frac{(\varepsilon_3 - 1)}{(\varepsilon_3 + 2)} j - \frac{(2\varepsilon_3 + 1)m}{(\varepsilon_3 + 2)(2\varepsilon_3 + \varepsilon_2)}\frac{b^3}{c^3} \quad , \quad j = \left[1 + 2\frac{(\varepsilon_3 - \varepsilon_2)(\varepsilon_2 - \varepsilon_1)}{(2\varepsilon_3 + \varepsilon_2)(2\varepsilon_2 + \varepsilon_1)}\frac{a^3}{b^3} \right]$$

and, $$m = (\varepsilon_3 - \varepsilon_2) + \frac{(\varepsilon_3 + 2\varepsilon_2)(\varepsilon_2 - \varepsilon_1)}{(2\varepsilon_2 + \varepsilon_1)} \frac{a^3}{b^3}$$

In above equation, parameters ε_c, ε_1, ε_2, and ε_3 are the dielectric constants of the composite, particles, interphase and polymer matrix, respectively. The parameter *a* is the radius of the filler, *b–a* is the thickness of the interphase region and *c* is the radius of the equivalent composite. The solid line in figure 5.3 represents the values calculated using the Vo and Shi model.

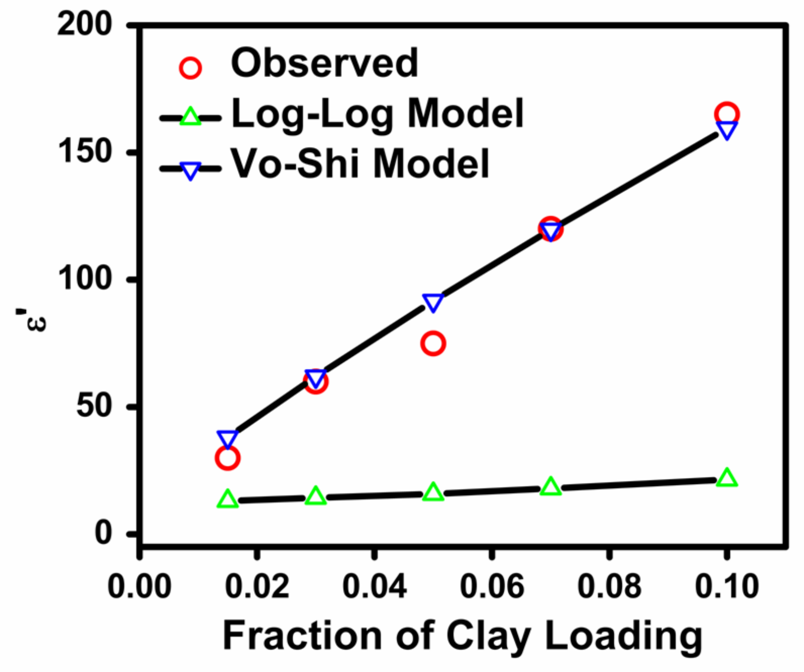

Figure 5.3: Model predicted and observed values of dielectric permittivity in PVDF/Clay nanocomposites.

In Vo-Shi model, they have systematically formulated a theory by considering the existence of interphase which takes the polymer filler interaction into account. As can be seen from the Figure 5.3, experimentally obtained permittivity values of PVDF/clay nanocomposites are in good agreement with the values predicted by the Vo and Shi model where interface constant K of 55 and permittivity of the interface of 400 provided the best fit. The value of K represents a relative volume of the interphase region influenced by the surface area of the dispersed phase [15, 20]. The high value of interface constant suggests high surface area and presence of strong interfacial interactions between PVDF and clay.

Role of Interface in Dielectric Permittivity

The frequency dependence of dielectric permittivity and fitting of the permittivity data by Vo-Shi model suggest the presence interfacial interactions in the PVDF/Clay nanocomposites. The strong interfacial interactions could be due to the interfacial polarization originating from remarkable difference between the dielectric permittivity of clay and PVDF. This interfacial polarization contributes to the increase in the dielectric permittivity of PVDF/clay nanocomposites.

Cole-Cole plot was used elucidate interfacial interaction in the nanocomposites. In polymer composites, both bulk and surface effects of charge carriers contribute to the dielectric permittivity [21, 22]. To distinguish bulk and interface effects the dielectric data was analyzed using Cole-Cole plots in impedance formalism as shown in figure 5.4.

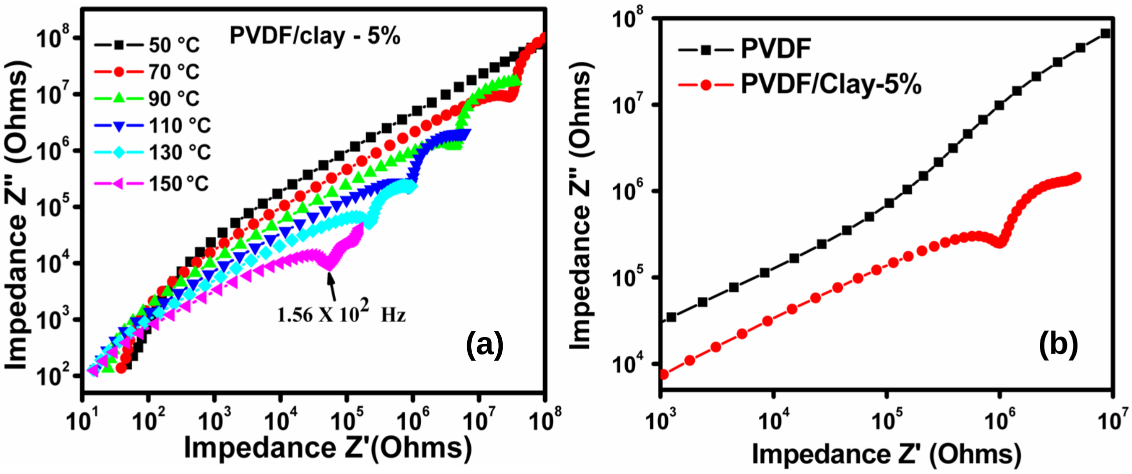

Figure 5.4: (a) Cole-Cole plot of PVDF nanocomposites loaded with 5% clay and (b) comparative Cole-Cole plot of PVDF and PVDF/clay-5% nanocomposite.

Two incomplete arches are observed above 70 °C as can be seen from the Figure 5.4 (a). However, at lower temperature (50 °C) only one arch is evident in the frequency range of our measurements. The presence of two semicircles at high temperature corresponds to the charge transport within the bulk and interface [23]. From figure 5.4 (b) it can be seen that, two incomplete arches are seen for nanocomposites. Since this kind of behavior is not observed in pristine PVDF, it can be ascribed to the presence of active interface between polymer and clay layers. This corroborates the contention that the interfacial effects become more evident and contribute towards the charge transport in nanocomposites.

Dielectric Relaxation Dynamics

Figure 5.5 shows the frequency dependence of dielectric loss (ε") curves for PVDF and PVDF/clay nanocomposites at 30 °C. Two relaxations are clearly discernible from the dielectric permittivity loss spectra of pristine PVDF. The faster segmental relaxation seen at frequency 10^{+07} Hz is attributed to glass transition relaxation and is denoted as α_a relaxation. It is well reported that the peak at 10^{+07} Hz is related to the micro-Brownian cooperative motions of the main chain backbone and is dielectric manifestation of the glass transition temperature of PVDF. In clay nanocomposites, the presence of clay, even up to 10%, does not affect the segmental process (glass transition relaxation- α_a process) confirming that the time scale and length scale of α_a process are unaffected at 30 °C. The slower relaxation peak at about 10^{+00} Hz is denoted as α_c relaxation and is associated with the molecular motions in crystalline region of PVDF and is ascribed to the non-polar i.e. α phase of PVDF. However, the crystalline relaxation peak completely disappears in PVDF/clay nanocomposites. It is well documented that absence of crystalline relaxation peak is attributed to the β phase crystallization of PVDF. The absence of crystalline relaxation peak in PVDF/clay nanocomposites thus can be recognized as a dielectric manifestation for formation of β phase in PVDF. Our XRD result already confirms the β phase crystallization of PVDF in the presence of clay.

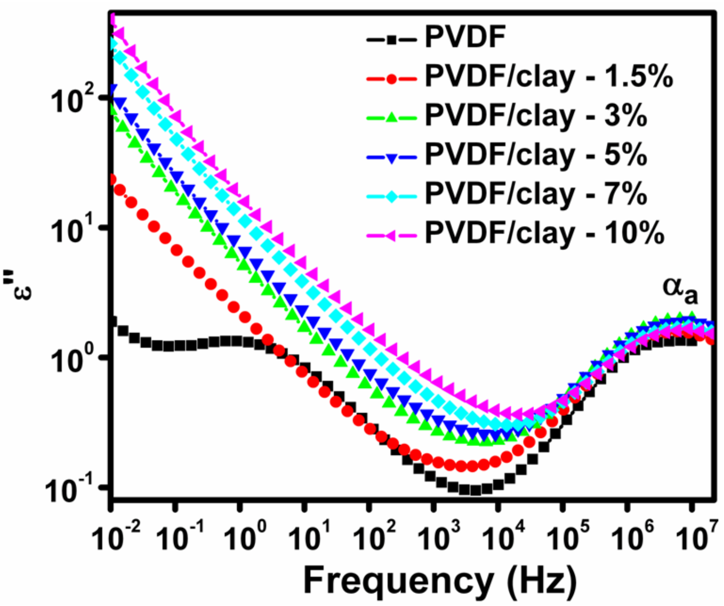

Figure 5.5: Frequency dependence of dielectric loss (ε") curves for PVDF and PVDF/clay nanocomposites.

Glass Transition Relaxation

The glass transition relaxation (α_a) in PVDF, was further studied the dielectric properties in the low temperature region, below 0 °C. Figure 5.6 (a) shows the α_a relaxation at different temperature for PVDF. The magnitude of the dielectric loss peak and frequency maximum position increases with increasing temperature. The broadening of relaxation peak also decreases with increasing temperature. Similar process is observed in PVDF/Clay nanocomposites.

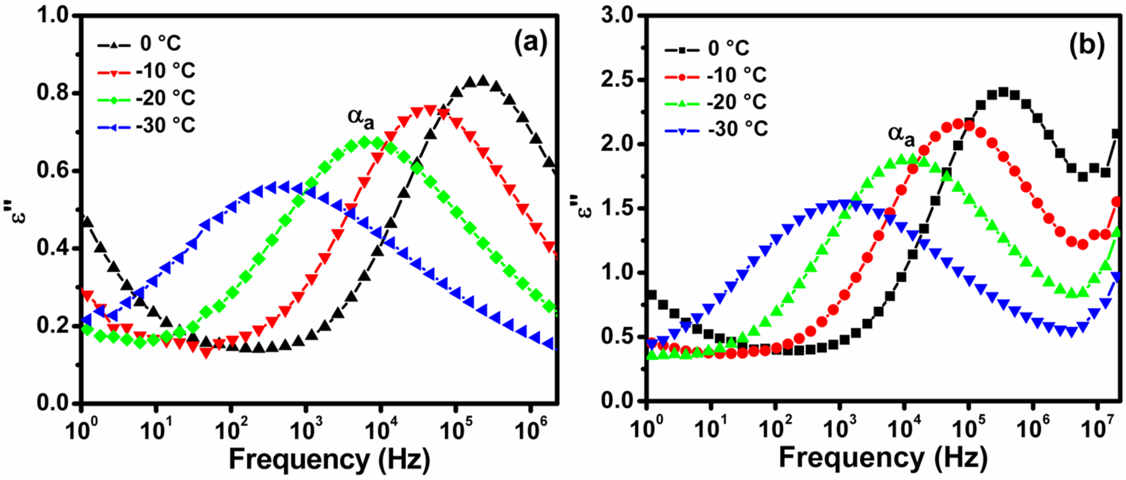

Figure 5.6: Glass transition relaxation (α_a) for (a) PVDF and (b) PVDF/Clay-5% at different temperatures.

Activation Energy

For glass transition (α_a) relaxation, the relation between relaxation time (τ_{max}) and the corresponding temperature can be described by the Vogel-Fulcher-Tamman (VFT) equation,

$$\log\tau\,(T) = \log\tau_0 - \frac{A}{(T - T_V)}$$

Where, $\log\tau\,(T)$ and A are constants, and T_V is the Vogel temperature, which is loosely related to the glass transition temperature and typically 50 °C below the glass transition temperature. Relaxation time τ(T) is obtained from the inverse of frequency.

Figure 5.7 shows the plot of relaxation time log (τ) versus reciprocal temperature (1000/T) and the curves are fitted to the VFT equation. All the fittted parameters are given in table 5.2 and are in good agreement with reported values in the literature [24].

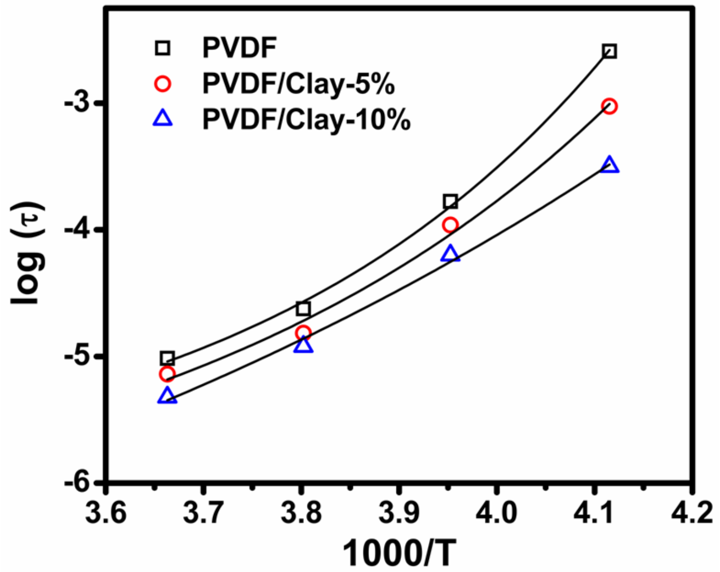

Figure 5.7: Characteristic relaxation time log (τ) versus reciprocal temperature (1000/T) for glass transition relaxation.

Sample	*log τ (sec)*	*E_a (eV)*	*T_o (K)*
PVDF	1.03×10^{-12}	0.098	188.9
PVDF/Clay-5%	4.47×10^{-12}	0.11	172.1
PVDF/Clay-10%	3.16×10^{-13}	0.10	181.2
Bello et al.[24]	5.2×10^{-12}	0.09	185.2

Table 5.2: VFT fitting parameters for glass transition relaxation (α_a) in PVDF and PVDF/Clay nanocomposites.

Figure 5.8 shows the α_a relaxation of PVDF and PVDF/Clay nanocomposites with different clay content at − *30 °C*. From figure 5.8 it can be seen that, with the increasing clay loading, the frequency at maximum dielectric loss shifts upward indicating the amorphous phase relaxation is affected due to addition of clay. In addition, relaxation strength significantly increases in the nanocomposites when compared to PVDF. This indicates that the nanocomposites are less crystalline or amorphous content increases in the nanocomposites. This is in consistent with our earlier work of Priya and Jog, suggesting the decrease in crystallinity in nanocomposites [25].

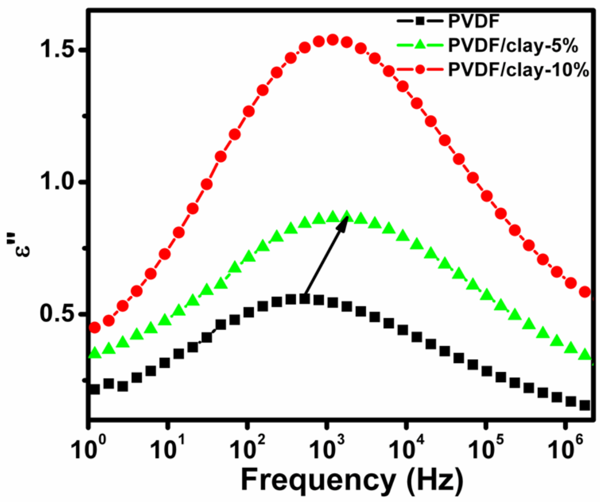

Figure 5.8: Dielectric loss (ε'') versus frequency of PVDF and PVDF/Clay nanocomposites for α_a *relaxation at −30 °C.*

AC Conductivity

Conductivity contribution to polymer has two contributions viz. dc and ac conductivity. The measured conductivity will be $\sigma = \sigma_{dc} + \sigma_{ac}$. Figure 5.9(a) shows the conductivity spectra for PVDF and PVDF/Clay nanocomposites at 30 °C.

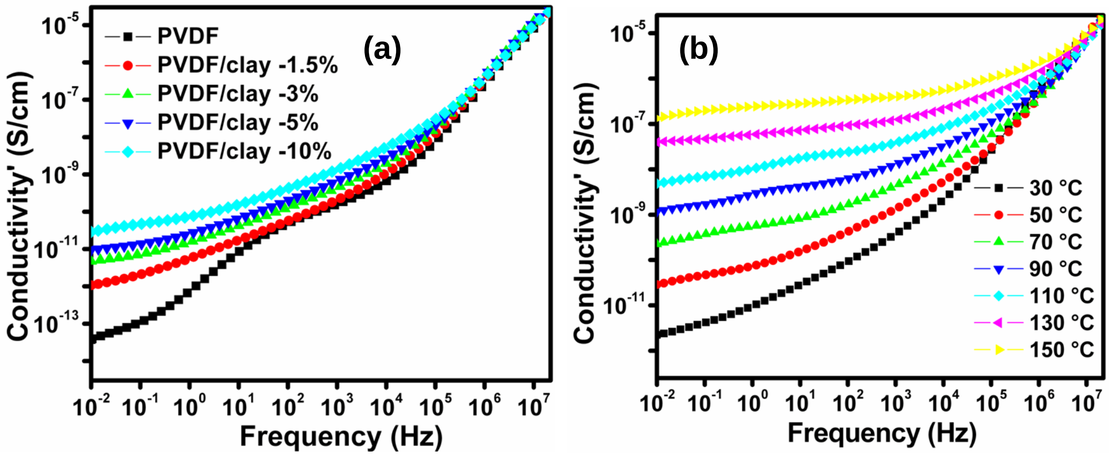

Figure 5.9: (a) ac conductivity spectra of PVDF and PVDF/clay nanocomposites at 30°C (b) Temperature dependence of ac conductivity for PVDF/Clay-10% nanocomposites.

The increase of conductivity with the increasing clay loading is observed. In the low frequency region, dc conductivity dominates and conductivity increases with increasing clay loading. At 10 wt% clay loading, dc conductivity increases upto three orders of magnitude when compared to PVDF. In case of PVDF, the dc conductivity increases with the increasing frequency, whereas for nanocomposites the slope of increase in conductivity becomes smaller and for 10 wt % loading almost conductivity plateau is observed in the low frequency region. At higher frequencies, where ac conductivity dominates, conductivity becomes frequency dependent and the slope of increase becomes similar to PVDF.

The temperature dependence of ac conductivity is shown in figure 5.9(b). The ac conductivity of the composites increases with increasing temperature and the convergence of conductivity at high frequency is observed. As the frequency decreases more and more charge carriers accumulate at the interface between the sample surface and the electrodes, which leads to drop in ac conductivity at low frequency. At high temperature conductivity is almost constant in the low frequency region but after certain critical frequency (f_c) is reached, conductivity increases with increasing frequency. The transition region from dc (frequency- independent) to ac (frequency dependent) conductivity shifts to higher frequencies with increasing temperature.

5.I.4 Conclusions

In conclusion, we have studied the structure and dielectric properties of melt blended PVDF/clay nanocomposites. X-ray diffraction (XRD) and FTIR studies indicated the formation of β phase in the PVDF/clay nanocomposites. The dielectric study of PVDF/Clay nanocomposites shows composition dependent enhancement in permittivity. The absence of crystalline relaxation peak in dielectric loss curve for nanocomposites also confirms the formation of β phase in PVDF/Clay nanocomposites. The analysis of dielectric permittivity data using logarithmic model based on effective medium theory predicted permittivity values which were lower than the experimental values. However, the experimental values of permittivity could be well fitted to the Vo and Shi model indicating the presence of interfacial interaction between PVDF and clay. The complex impedance formalism analysis further supported the presence of interfacial effects. Thus the observed increase in the dielectric permittivity could be attributed to the presence of strong interfacial interaction.

Section II: PVDF/Clay Nanocomposites as a Gate Dielectric in Organic FET

5.II.1 Introduction

Over the past twenty years, research in the field of organic field effect transistors (OFET) has attracted significant research interest due to their wide range of applications such as organic integrated circuit board, low cost radio frequency identification tags (RFID), organic active matrix display, gas sensors, and infra red (IR) sensor [26-28]. OFET also offer advantage in terms of low cost, ease of process, flexibility and light weight [29]. Current research in this field is aimed towards design of OFET having multifunctional applications in single device architecture.

One of the prominent applications of OFET is in the field of memory devices. In memory devices the information is stored using physical property that displays hysteresis in response to an applied electric field. Ferroelectric polymers such as Poly (vinylidene fluoride) PVDF and its copolymer have been widely studied as a gate dielectric material in OFET [30-32]. The ferroelectricity in PVDF is found to originate from bistable dipole polarization between hydrogen and fluorine atoms and making the material suitable for potential memory devices. PVDF is well known polymer which exhibits ferroelectric and pyroelectric properties. Apart from this, PVDF has several other advantages like high Curie temperature, short switching time and good thermal stability. Another important factor for PVDF based device is to achieve ferroelectric β phase of PVDF having polarization better than other crystalline forms α and γ of PVDF. In the first section of this chapter we have seen that addition of Clay induces β phase in PVDF. Although OFET based on PVDF were studied in details in the past, OFETs based on the nanocomposites of PVDF are not studied so far. In this section we will discuss the use of PVDF/clay nanocomposite in OFET device. We also discuss the applications of the OFET as a non-volatile memory and Infra red (IR) sensing device.

Also, the performance of OFET depends critically on the gate dielectric and semiconductor interface. Dielectric constant of the gate dielectric is one of the crucial parameter in the performance of OFET. The conventional inorganic gate dielectric material such as SiO_2 suffers from the low dielectric constant. Polymer gate dielectric with high dielectric constant offers advantage over the inorganic gate dielectric.

Further, the non-interacting nature of organic- organic interface is also found to be favorable in performance of OFET.

In this context we have studied use PVDF/Clay nanocomposites as a gate dielectric material in OFET device architecture. The nanocomposite layer used in present study offer several advantages: i) it has high dielectric constant which increases the gate capacitance and hence charge carrier density at the semiconductor dielectric interface, ii) it has high dielectric strength which effectively reduces the gate leakage current, iii) it exhibits desirable ferroelectric and pyroelectric properties, and iv) it is solution processable.

5.II.2 Experimental

In this work, bottom gate top contact of FET configuration is fabricated. Cleaned Indium doped tin oxide (ITO) coated glass slide (Aldrich) is used as a gate electrode. Gate dielectric was prepared by spin coating PVDF/Clay nanocomposite solution onto ITO substrate. The PVDF nanocomposite with 5wt% clay loading was used as a gate dielectric in OFET configuration. For this, solution of 5wt% PVDF/Clay nanocomposite in DMF: Acetone (1:1) is prepared and spin coated at 1500 rpm for 1 min. The film is then annealed at 140 °C for 2 hr to enhance the crystallinity of the films. The film thickness was around 2 μm, measured using Dektak profilometer. An additional layer of poly (4-vinyl phenol) (PVP-crosslinker) solution is deposited onto PVDF layer. The PVP layer helps to increase electric breakdown strength of dielectric layer and also allows the controlled growth of Pentacene by the reduction of the substrate roughness. The PVP cross linker solution was prepared by taking PVP (11%) and Polymelamine co-Formaldehyde (4%) in propylene glycol monomethyl ether. The PVP Cross linker was spin coated at 1500 rpm for 1 min. The films were annealed at 100 °C for 20 min and 175 °C for 1 hr. The thickness of PVP layer was around 1 μm. Before carrying out the FET measurement, a capacitor structure of gate dielectric was fabricated to study the leakage current. In all devices leakage current was found to be less than 10^{-09} A.

Pentacene was used as a semiconducting channel layer in the OFET configuration. Pentacene was deposited by thermal evaporation process (at pressure of 10^{-06} Torr). The thickness of the semiconductor channel layer is around 50-70 nm. Finally, pure gold was deposited by PLD process through shadow masking to form the top drain source contact. The thickness of the gold contacts was around 100 nm. The transistor has dimensions of channel length 150 μm and width 1500 μm. The schematic of device architecture is shown in figure 5.10 (a). The device also shows high optical transparency as shown in figure 5.10 (b). The I-V characteristics were performed on Agilent make semiconductor analyzer. For comparison OFET using only PVDF as dielectric is also prepared. Ferroelectric properties of metal/PVDF/metal capacitors with Au bottom and Al top electrodes were obtained using Radiant Technologies PE loop analyzer.

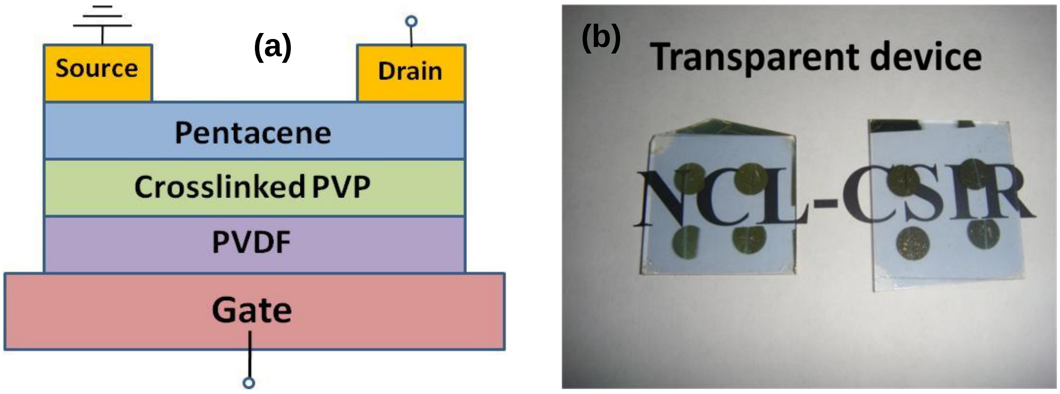

Figure 5.10 (a) shows the schematic of device architecture (b) photographs of actual FET device showing high optical transparency.

5.II.3 Results and Discussion

5.II.3.1 Structural Analysis

The crystalline structure of spin casted PVDF/Clay nanocomposites is studied using ATR-FTIR spectroscopy. Figure 5.11(a) compares FTIR pattern of melt process and spin coated PVDF/Clay nanocomposite. It may be recalled that, melt compounded PVDF/Clay nanocomposites crystallizes into β phase. From the figure 5.11 (a), it can be seen that FTIR spectra corresponding to melt press film and spin coated samples are almost similar. This indicates that spin coated PVDF/Clay thin film also crystallizes into β phase of PVDF.

MFM structure was fabricated for ferroelectric loop analysis. Polarization hysteresis data of spin coated PVDF/Clay nanocomposites is presented in the figure 5.11 (b). The polarization curve shows typical hysteresis loop indicating the ferroelectric nature of gate dielectric layer. The nanocomposite film shows remanent polarization (P_r) of 1.2 μC/cm^2 with the coercive voltage (V_c) of 9 V. The remanent polarization (Pr) is less than the reported value of 7 μC/cm^2 [29]. It is to be noted that these measurements were carried out on the as deposited films of PVDF/Clay nanocomposites and the films were not poled.

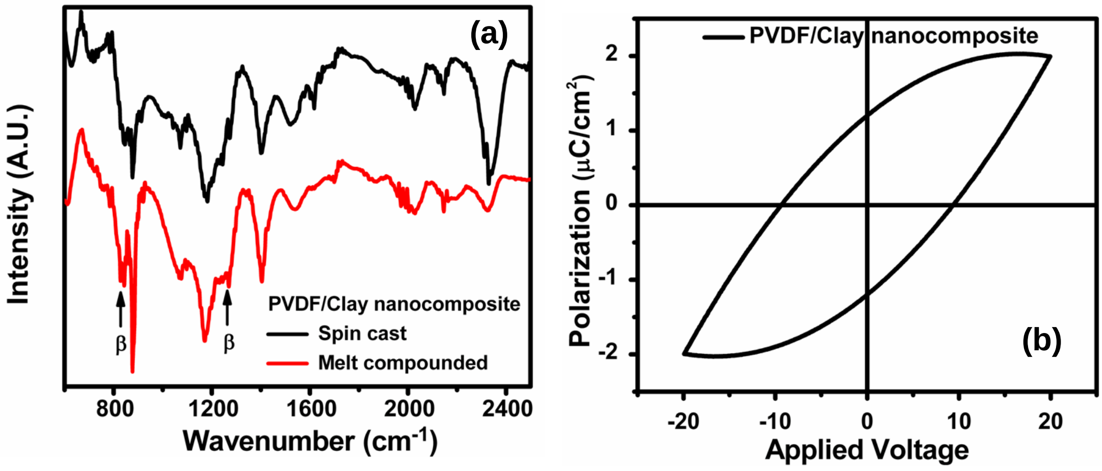

Figure 5.11: (a) ATR-FTIR spectra of spin coated and melt compounded PVDF/clay nanocomposite and (b) polarization hysteresis (P-E curve) of metal-insulator-metal (MIM) capacitor structure of PVDF/clay nanocomposite.

5.II.3.2 Transistor Characteristics of PVDF/Clay OFET

The output characteristic of PVDF/clay nanocomposite FET is shown in the figure 5.12 (a). The FET exhibits good linear and saturation behavior. The device operates in accumulation enhancement mode and shows p-type characteristics. Figure 5.12 (b) shows the typical transfer curve for bottom gated PVDF/Clay nanocomposite FET. In the transfer curve, the gate bias (V_{GS}) was swept from + 90 V to – 90 V and back with the constant drain voltage (V_{DS}) of – 30 V. A sharp increase in the drain current (I_{DS}) with negative gate bias was observed due to the holes accumulating at the semiconductor dielectric interface. When the gate voltage is returned to zero, I_{DS} almost retained its value indicating polarization of dipoles in PVDF. The drain current has bistability at zero gate bias due to ferroelectric polarization of gate dielectric material. The transfer curve shows the hysteresis loop in the clockwise direction. Hysteresis in the OFET is normally related to the bistability in the operational transistor current and its origin can be attributed to different mechanisms. Typically, charge trapping process at the semiconductor dielectric interface induces anticlockwise hysteresis in the p channel FET. Whereas, the presence of dipolar groups in the dielectric causes the clockwise hysteresis in the p-channel FET attributing to the ferroelectric nature of the gate dielectric layer. Thus the observed hysteresis in the present study is due to ferroelectric polarization of the gate dielectric material rather than the charge trapping mechanism.

For comparison, we also fabricated the Pentacene FET with pristine PVDF as a gate dielectric. Figure 5.12(c) & (d) shows output and transfer characteristics of PVDF based device. The output and transfer characteristics show that device exhibit p-type characteristics operating in accumulation mode. On comparing the transfer characteristics with the PVDF/clay FET, it clearly shows that hysteresis loop is not prominent in PVDF based FET device. This is expected as the spin casting of PVDF film forms predominately non-polar α phase and therefore significant hysteresis is not observed in the transfer characteristics.

The field effect mobility (μ_{FE}) was calculated from the slope of the square root of the drain current versus gate voltage in the saturation regime using following equation.

$$I_{DS}= (W/2L)\ \mu_{FE}\ C\ (V_G - V_{th})^{2}$$

Where, I_{DS} is drain source current, μ_{FE} is the field effect mobility, V_{th} is threshold voltage and C is the capacitance of the gate dielectric. Table 5.3 shows the device parameters of FET device. From table 5.3, it is clear that both the mobility and on/off ratio has been improved in the case PVDF/Clay nanocomposite OFET compared PVDF OFET.

Dielectric layer	Mobility ($cm^2V^{-1}s^{-1}$)	On/Off Ratio	Threshold Voltage
PVDF FET	0.004	$6.69 \times 10^{+01}$	25
PVDF/Clay FET	0.030	$1.39 \times 10^{+03}$	– 5

Table 5.3: Device parameters of PVDF and PVDF/Clay FET.

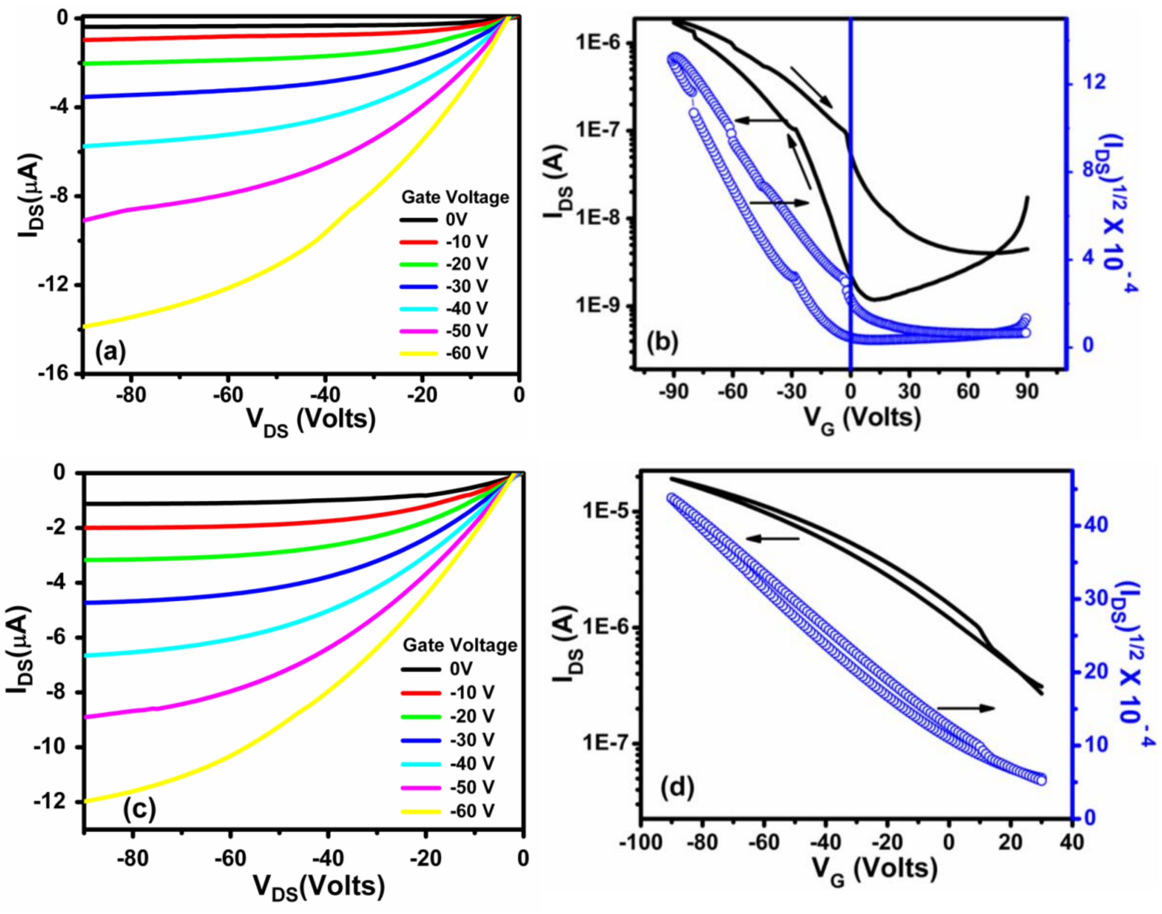

Figure 5.12: (a) Output and (b) transfer characteristics of PVDF/Clay nanocomposite FET, (c) Output and (d) transfer characteristics of PVDF FET.

5.II.3.3 Nonvolatile Memory OFET

In memory OFET, transistor can be established into ON or OFF state by means of voltage applied to gate electrode. Memory retention of our device is studied by applying writing voltage to the gate with respect to short circuited drain source electrodes. Memory retention properties of PVDF/Clay nanocomposite device is studied by measuring I_{DS} in the ON and OFF state under zero gate bias with a constant V_{DS} of – 50 V. In the memory retention studies, for OFF state measurement a gate voltage pulse of + 90 V is applied for 10 s to drive the device into OFF state and the drain source (I_{DS}) current is measurement as a function of time. Similarly, for ON state measurement a gate voltage pulse of – 90 V was applied for 10 seconds to make the device into ON state and drain source current (I_{DS}) is measurement as a function of time. Figure 5.13 shows the results of memory retention measurement. Drain source current (I_{DS}) current does not show any significant drop in ON current over a long time period inspite of small decrease in the ON current at the beginning whereas OFF current seems to be even more stable. An asymptotic nature of ON and OFF behavior is also similar to earlier work presented in the literature [28, 31].

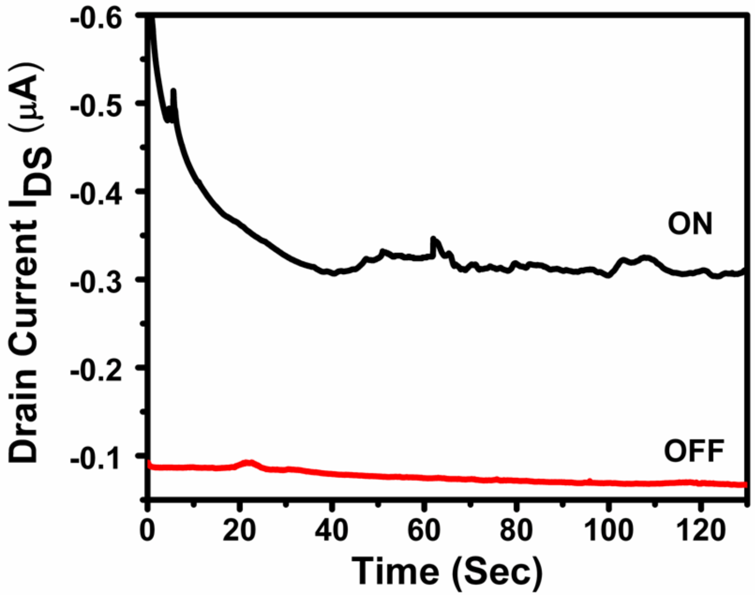

Figure 5.13: Both ON and OFF state currents were measured at zero gate voltage with the continuous drain voltage (V_{DS}) of – 50 V after single gate voltage pulse of – 90 V and +90 V for ON and OFF current, respectively.

5.II.3.4 Infrared (IR) Response of the Device

Infrared (IR) response of the device is determined by illuminating the device by IR lamp and monitoring drain source (I_{DS}) current. The drain source current (I_{DS}) is recorded at a constant drain source voltage (V_{DS} = – 30 V) and gate voltage (V_{GS} = – 30 V). The response of the device is shown in figure 5.14. Upon the illumination of the device with IR radiation, an increase in I_{DS} is observed and with the removal of IR radiation, drain current was found to decrease immediately. It is noteworthy that nanocomposite OFET device shows significant response to IR radiations, compared to neat PVDF OFET. The increase in the drain current by IR illumination can be understood by considering the change in effective mobility of pentacene and due to the positive pyroelectric coefficient of PVDF dielectric layer. When the device is illuminated with IR radiation, thermally activated hopping transport in pentacene is also expected to be enhanced which effectively increases the drain current. In addition to this, positive pyroelectric coefficient of gate dielectric increases effective gate voltage bias which helps in the increase of drain current. The pyroelectric nature of gate dielectric is discussed in the next section.

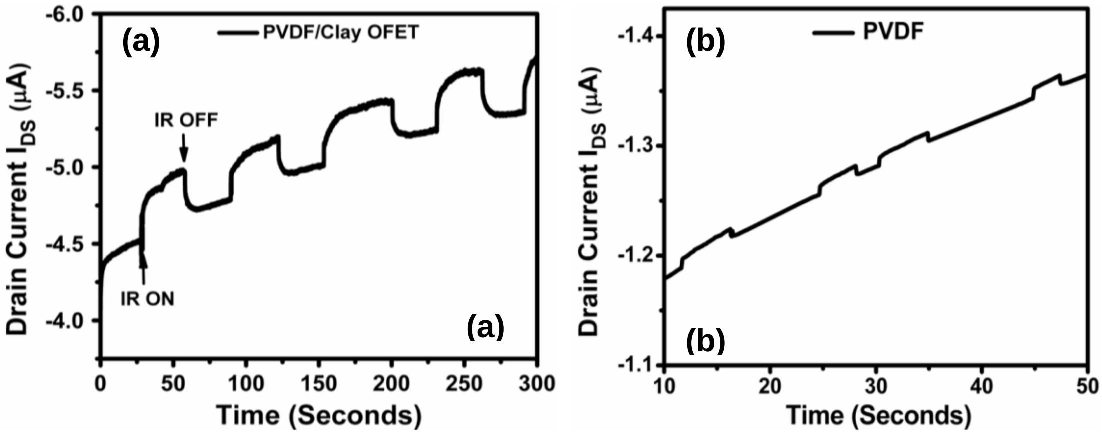

Figure 5.14: IR response of (a) PVDF/Clay nanocomposite OFET (b) PVDF OFET device.

5.II.3.5 Temperature Sensing of OFET

The temperature response of the device was studied to examine the pyroelectric behavior of the gate dielectric material. For this measurement, the temperature of the device is slowly increased by controlled heating and drain current is monitored at constant drain source voltage (V_{DS} = –30 V) and gate voltage (V_G = –30 V). The drain current is also monitored as the temperature is reduced. Figure 5.15 (a) shows the temperature response of PVDF/clay nanocomposites OFET as a function of time. The drain current increase with the increasing temperature was observed and vice a versa. This indicates the positive pyroelectric coefficient of the gate dielectric material. Figure 5.15 (b) shows the same temperature response of PVDF/clay nanocomposite OFET plotted as a function of temperature. Figure 5.15 (b) shows that, the drain current (I_{DS}) values differ in the forward and backward directions. The backward current is less than the forward current, due to the decrease in the remnant polarization of gate dielectric. In the present case, the temperature response of the FET device is non-linear. This result is similar to the reported work by Lee et al. for non poled devices. However a linear response with temperature was reported for poled devices [28]. It may be noted that the samples are not poled in our studies.

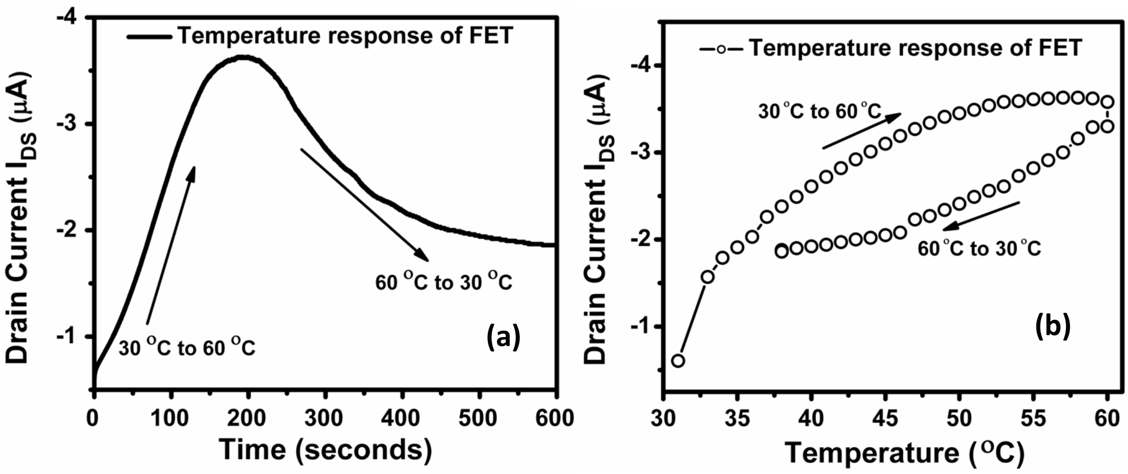

Figure 5.15: Temperature response of FET measured as a change in drain source current when the temperature is increased from 30 °C to 60 °C and cooled back from 60 °C to 30 °C as a function of (a) time and (b)temperature.

5.II.4 Conclusions

In conclusion, the dielectric studies show the composition dependent enhancement in permittivity of PVDF/Clay nanocomposites. The absence of crystalline relaxation peak in permittivity loss curve for nanocomposites confirms the formation of β phase in PVDF/Clay nanocomposites. The X-ray diffraction study of PVDF/clay nanocomposites also confirms the formation of ferroelectric β phase crystallization of PVDF in the nanocomposites. The analysis of dielectric permittivity data using logarithmic model based on effective medium theory predicted permittivity values which were lower than the experimental values. However, the experimental values of permittivity could be well fitted to the Vo and Shi model indicating the presence of interfacial interaction between PVDF and clay. The complex impedance formalism analysis further supported the presence of interfacial effects. Thus the observed increase in the dielectric permittivity could be attributed to the presence of strong interfacial interaction.

We have also demonstrated the feasibility of using PVDF/Clay nanocomposite as gate dielectric layer in the FET device. The device exhibit excellent transistor performance with p-type operation. The device shows a good response to the IR radiation. The successful operation of FET device provides a promising route for realizing both memory storage and IR sensing applications in a single device.

5.II.5 References

1. J. Lu, K. Moon, C.P. Wong, *Electronic Components and Technology Conference,Proceedings. 57th*, **2007**.
2. Y. Bai, Z.Y. Cheng, V. Bharti, H.S. Xu, Q. M. Zhang, *Appl. Phys. Lett.*, **2000**, 76, 3804**.**
3. A. Maliakal, H. Katz, P.M. Cotts, S. Subramoney, P. Mirau, *J. Am. Chem. Soc.,* **2005**, 127, 14655.
4. Z.M. Dang, H.P. Xu, D. Xie, L. Li, *Mater. Lett.,* **2000,** 61, 511-515.
5. C.V. Chanmal, J.P. Jog, *eXpress Polymer Letters,* **2008**, 2, 294.
6. D. H. Kuo, C. C. Chang, T. Y. Su, W. K. Wang, B. Y. Lin, *J. Eur. Cera. Soc.,* **2001** 21**,** 1171.
7. M. Arbatti, X. Shan, Z. Cheng, *Adv. Mater.,* **2007**, 19, 1369-1372.

8. Z. M. Dang, L.Z. Fan, Y. Shen, C.W. Nan, *Mater. Sci. Eng. B.*, **2003,**103, 140**.**
9. B. Hilczer, J. Kulek, E. Markiewicz, M. Kosec, B. Malic, *J. Non-Crystalline Solids,* **2002,** 305 167.
10. Suprakas Sinha Ray, Masami Okamoto, *Prog. Polym. Sci.*, **2003**, 28, 1539–1641.
11. R.J. Sengwa, Shobhna Choudhary, Sonu Sankhla, *Composites Sci. and tech.,* **2010**, 70, 1621-1627.
12. Priya L, J. P. Jog, *J. Polym Sci, Polym Phys.*, **2002**, 40, 1682.
13. Lei Yu, Peggy Cebe, *Journal of Polymer Science Part B: Polymer Physics***,** **2009**, 47, 2520-2532.
14. Y. Rao, J. Qu, T. Marinis, C.P. Wong, *IEEE transactions on components and packaging technologies,* **2000**, 23, 680**.**
15. M.G. Todd, F. G. Shi, *Microelectronics Journal,* **2002**, 33, 627-632.
16. K. Wakino, T. Okada, N. Yoshida, K. Tomono, *J. Amer. Cera. Soc.*, **1993,** 76, 2588-94.
17. Y. Wang, J. Wang, F. Wang, S. Li, J. Xiao, *Polymer Bulletin,* **2008**, 60, 5.
18. R. Popielarz, C.K. Chiang, R. Nozaki, J. Obrzut, *Macromolecules*, **2001**, 34, 5910-5915.
19. H.T. Vo, F. G. Shi, *Microelectronics Journal,* **2002**, 33, 409.
20. P. Murugaraj, D. Mainwaring, N. Mora-Huertas, *J. Appl. Phys.*, **2005**, 98, 054304.
21. S. De, A. Dey, S.K. De, *Eur. Phys. Journal B*, **2005**, 46, 355.
22. G. Liu, C. Wang, C. Wang, J. Qui, M. He, J. Xing, K. Jin, H. Lu, G. Yang, *Appl. Phys. Lett.,* **2008**, 92, 122903.
23. H. Lu, X. Zhang, H. Zhang, *J. Appl. Phys.*, **2006,**100, 054104.
24. A. Bello, E. Laredo, M. Grimau, *Physical review B*, **1999**, 60, 12764.
25. Priya L., J. P. Jog, *J Polym Sci, Polym Phys,***2002**,40,1682.
26. B. Crone, A. Dodabalapur, A. Gelperin, L. Torsi, H. E. Katz, *Appl. Phys. Lett.*, **2001**, 78, 15.
27. Tran Quang Trung, Nguyen Thanh Tien, Young Gug Seol, Nae-Eung Lee, *Organic Electronics,* **2012**, 13, 533-540.
28. Nguyen Thanh Tien, Young Gug Seol, Le Huynh Anh Dao, Hwa Young Noh, Nae-Eung Lee, *Adv. Mater.*, **2009**, 21, 910–915.

29. Ronald C. G. Naber, Kamal Asadi, Paul W. M. Blom, Dago M. de Leeuw, Bert de Boer, *Adv. Mater.*, **2009**, 21, 1-13.

30. Seok Ju Kang, Youn Jung Park, Jinwoo Sung, Pil Sung Jo, Cheolmin Park, Kap Jin Kim, Beong Ok Cho, *Appl. Phys. Lett.*, **2008**, 92, 012921.

31. Sun Kak Hwang, Sung-Yong Min, Insung Bae, Suk Man Cho, Kang Lib Kim,Tae-Woo Lee, Cheolmin Park, *Organic Electronics*, **2012**, 13, 491–497.

32. K. N. Narayanan Unni, Remi de Bettignies, Sylvie Dabos-Seignon, Jean-Michel Nunzi *Appl. Phys. Lett.*, **2004**, 85, 10.

Chapter 6

Conclusions and Future Scope

This chapter describes the salient features of the results presented in this thesis and the scope for future work.

6.1 Summary of the Thesis

The main objective of the thesis was to fabricate nanocomposites based on PVDF using three different types of nanofillers viz. $BaTiO_3$, MWCNT and Clay. The nanocomposites were fabricated using melt compounding technique, pulsed laser deposition, and electrospinning technique. The effect of nanofillers on the dielectric properties were studied in detail and the applications of nanocomposites in low thermal emissivity and organic field effect device (OFET) were explored.

The major results of the work carried in the thesis can be summarized as following

1. PVDF/$BaTiO_3$ bulk nanocomposites were prepared by melt mixing technique. The frequency and temperature dependence of dielectric properties were studied in detail. Permittivity of PVDF increased with increasing loading of $BaTiO_3$. The nanofibers of PVDF/$BaTiO_3$ nanocomposites were prepared by electrospinning technique. The thermal emissivity of electrospun nanofibers were measured using a prototype instrument based on thermopile. The measurement showed that electrospun nanofibers showed lower thermal emissivity compared to the melt pressed PVDF/$BaTiO_3$ nanocomposites. The reduction in the thermal emissivity was attributed to the porous and non-woven morphology of the electrospun fibers. The low thermal emissivity of electrospun fibers makes it a suitable material for camouflaging in defense related applications.
2. PVDF/MWCNT nanocomposites thin films were prepared by pulsed laser deposition (PLD). The addition of MWCNT showed enhancement in the ferroelectric β phase of PVDF. The dielectric studies showed significant enhancement in the permittivity when MWCNT loading was near to percolation threshold. The percolation threshold was found to be higher than for the bulk sample due to reduction in aspect ratio of MWCNT during PLD process. This increase in percolation threshold allowed higher loading of MWCNT (upto 7 wt%) into polymer matrix. Figure 6.1 compares the dielectric permittivity of PVDF/MWCNT nanocomposites with PVDF/$BaTiO_3$ and PVDF/clay nanocomposites. It can be seen that, significant increase in the permittivity is observed in PVDF/MWCNT nanocomposites at relatively lower filler loading. Comparatively, very small increase is observed in the PVDF/$BaTiO_3$

nanocomposites. Thus, percolative composites system is found to be superior compared to the polymer/ceramic nanocomposites.

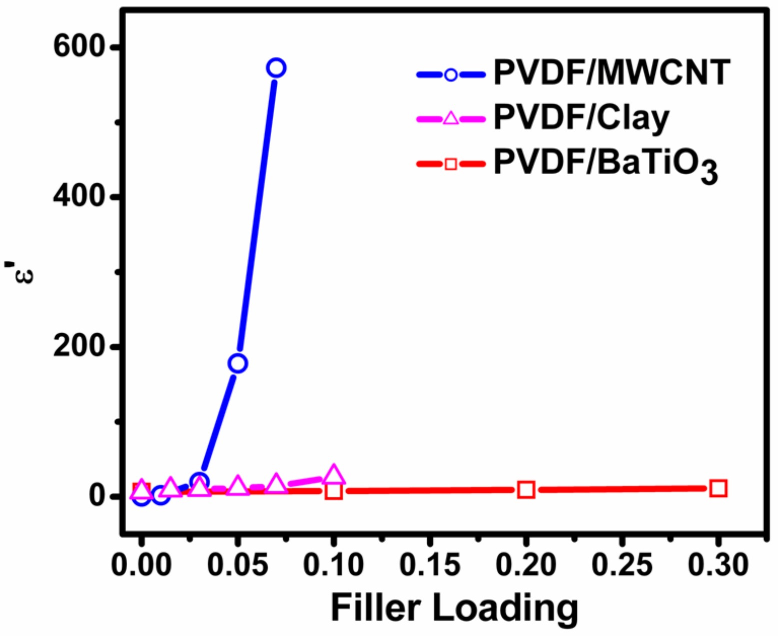

Figure 6.1: Comparison of dielectric permittivity of PVDF/MWCNT with different loading of MWCNT at 10^{+02} *Hz frequency. For comparison, data for* $PVDF/BaTiO_3$ *and PVDF/Clay nanocomposites were also shown.*

The conductivity of PVDF/MWCNT nanocomposites also found increase with the MWCNT loading. The PVDF/MWCNT nanocomposite layer was studied as an active channel layer in OFET configuration. The device showed strong field modulation of drain current when MWCNT loading was near to percolation threshold (5 wt %). Thus the nanocomposite route offers a unique way of realizing organic transistor.

3. PVDF/Clay nanocomposites were prepared by melt blending technique. Dielectric studies showed enhancement in the dielectric permittivity in nanocomposites which was attributed to the interfacial interactions between filler and polymer matrix. The dielectric permittivity increased to 165 with 10 wt% loading of clay. The fitting experimental data was fitted to Vo-Shi model which confirm the interface contribution to dielectric permittivity.

The organic field effect transistor (OFET) was fabricated using thin films of spin coated PVDF/Clay nanocomposites as a gate dielectric material. The device showed excellent transistor characteristics with p-type operation. Due to the ferroelectric property of PVDF/Clay nanocomposites, OFET device showed excellent memory retention characteristics. Moreover, the device also showed response to IR signal due to the pyroelectric property by PVDF. Thus, the direct integration of PVDF/clay nanocomposites as gate dielectric layer demonstrated the efficiency of device for IR sensing and non-volatile memory applications.

6.2 Scope for Future Work

1. All Organic FET

With electrospinning technique it is possible to fabricate indium tin oxide (ITO) nanofibers on a given substrate. The electrospun ITO nanofibers show good conductivity level making an alternative candidate for gate electrode material in OFET. It will be interesting to study the fabrication of OFET with electrospun ITO nanofibers as gate electrodes. In our studies, we have independently used PVDF/MWCNT nanocomposites as channel layer and PVDF/Clay nanocomposites as ferroelectric gate dielectric layer. The integration of all these components into single device can bring unique approach of fabricating OFET with multifunctional properties. Moreover, flexible substrate can be also used for device fabrication. This flexible all organic FET can have potential applications in electronic devices like handheld portable sensors or detectors.

2. Electromagnetic Interference (EMI) Shielding Material

In recent years, electronics field in the area of wireless communication systems, high speed devices, cellular phones etc. has gained rapid development. Due to the increasing use of high frequency and high bandwidth in this technology, there are chances of deterioration in the incoming radio signals which is known as Electromagnetic interference (EMI). This interference has an adverse effect on the communication systems. Hence there is need of material which acts as a microwave absorber. Typically, metals and metallic composites are used as a shielding material due to their good electrical conductivity. However, these metals suffer from corrosion, poor chemical resistance, difficult processing and high density. Hence, polymer based composites were increasingly investigated as an alternative for EMI shielding material [1-3]. In this context, PVDF/MWCNT nanocomposites can offer potential application in EMI shielding applications.

3. Multiferroic Nanocomposites

Multiferroic materials are the one which simultaneously exhibit ferroelectricity and ferromagnetism. Recently, multiferroic materials stimulated an increasing attention as prospective candidate for potential applications in emerging fields like spintronics and sensor devices. The key performance of a multiferroic material relies on strong magnetoelectric coupling which control magnetization *via* polarization and *vice versa*. Typically, magnetoelectric coupling refers to the magnetic induction by an electric field or electrical polarization by a magnetic field. However, natural single phase multiferroic materials are rare or their performance is rather very weak at room temperature. This difficulty can be solved by fabricating composite material or hybrid materials having diverse properties [4, 5].

Polymer based multiferroic materials has inherent advantage of ease of processing, mechanical flexibility, and light weight. PVDF can offer unique advantage as polymer based multiferroic as it is known for its ferroelectric, piezoelectric and pyroelectric properties. The composite of PVDF with magnetoelectric materials like Fe_3O_4, $CoFe_2O_4$, and ferrites can be interesting system for multiferroic materials applications.

6.3 References

1. Young-In Lee, Kun-Jae Lee, Ki Do Kim, Hee Taik Kim, Young-Wook Chang, Shin-Choon Kang, and Yong-Ho Choa, *J. Nanosci. Nanotechnol.*, **2007**, 7, 11.
2. Feng-Yu Yang, Kuo-Jui Chang, Meei-Yu Hsu, Cheng-Chin Liu, *J. Mater. Chem.*, **2008**, 18, 5927–593.
3. Chun-Sheng Zhang, Qing-Qing Ni, Shao-Yun Fu , Ken Kurashiki, *Composites Science and Technology* , **2007**, 67, 2973–2980.
4. Ce-Wen Nan, M. I. Bichurin, Shuxiang Dong, D. Viehland, G. Srinivasan, *J. Appl. Phys.*, **2008**, 103, 031101.
5. O. D. Jayakumar, B. P. Mandal, J. Majeed, G. Lawes, R. Naik, A. K. Tyagi, *J. Mater. Chem. C*, **2013**, 1, 3710–3715.

Appendix-I

Magneto-Dielectric Properties of PVDF/Fe_3O_4 Nanocomposites

The magneto dielectric properties of PVDF/Fe_3O_4 nanocomposites fabricated by melt processing are presented here. The dielectric relaxation spectroscopy (DRS) technique is used to investigate the dielectric relaxation and molecular mobility in PVDF/Fe_3O_4 nanocomposites. Dielectric spectroscopy showed an increase in the permittivity of nanocomposites in the whole frequency range studied. The magnetic properties show a ferromagnetic behavior in polymer nanocomposites. The fabricated nanocomposites have potential for use in electronics packaging substrate as an alternative substrate owing to their good thermal, mechanical and dielectric properties.

A.1 Introduction

Magnetic particles embedded in ferroelectric polymer matrix can have excellent potential application such as magneto-optical storage devices, flexible electronic devices etc. Hybrid inorganic–organic nanocomposite materials are of current interest because of their multifunctionality, ease of processability, and potential for large-scale manufacturing. Many attractive properties of polymers like non-corrosiveness, light weight, mechanical strength, and dielectric tunability can be utilized along with magnetic and optical properties of nanoparticles to make multifunctional materials [1-3]. The advantages of these materials in electromagnetic interference (EMI) reduction are due to desirable properties like frequency agility, light weight, and non-corrosive nature.

Inclusion of ferromagnetic nanoparticles in polymers is especially important as magnetic nanoparticles have shown promise in various potential applications like spin-polarized devices, carriers for drug delivery, magnetic recording media, high-frequency applications, etc.[4,5] However, for most of these highly specialized applications, there is a practical need to disperse the nanoparticles in non-magnetic media that can be easily processed. Polymer materials are very well suited for this purpose. Magnetic nanoparticles embedded in polymer matrices have excellent potential for electromagnetic device applications like electromagnetic interference suppression.

Advances made to prepare the multifunctional nanocomposites have led great improvement in this field. Several approaches have been developed to synthesize these composites in bulk as well as thin-film forms like sol gel, vacuum evaporation from powders, layer-by-layer self assembly, etc. In the present work, we have synthesized polymer nanocomposites of Poly (vinylidene fluoride) doped with varying concentrations of Fe_3O_4 nanoparticles (~30-50 nm in size). These nanocomposites were processed using simple melt blending technique. The polymer processing conditions were optimized to achieve good uniform dispersion of the nanoparticles in the polymer matrix.

A.2 Experimental

Materials

PVDF Grade, Solef 1008 procured by Solvay Belgium is used for this study. Fe_3O_4 nanoparticles were procured from Aldrich Chemicals. The Fe_3O_4 were used as received for the experiments without any chemical treatment for surface modification. Figure A.1 shows the TEM and XRD of Fe_3O_4 nanoparticles. TEM micrograph shows the spherical particle shape of Fe_3O_4 nanoparticles. The particle size of Fe_3O_4 was estimated to be 30–50 nm. The XRD of the nanopowder exhibits the characteristic peaks of Fe_3O_4. The peaks at 30.2°, 35.4°, 43.3°, 53°, 57.2° and 62.9° corresponding to the (220), (311), (400), (422), (511) and (440) planes of Fe_3O_4 confirming the cubic spinel structure [6].

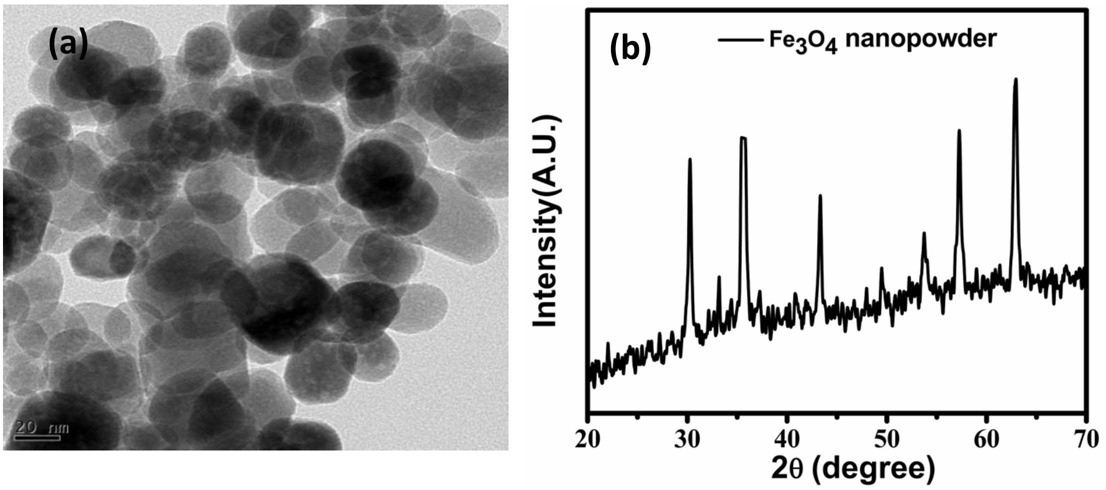

Figure A.1: (a) TEM micrograph and (b) X-ray diffraction pattern of Fe_3O_4 nanoparticles.

Fabrication of PVDF /Fe_3O_4 nanocomposites:

The nanocomposites of PVDF with various weight percent of Fe_3O_4 (10, 20, 30, 40 % wt/wt) were prepared by melt mixing in Thermo Haake Polylab batch mixer at 200 ^{o}C, with 60 rpm and residence time of 5 minutes. Prior to melt processing, all the materials were dried in an air circulatory oven at 70 °C for 24 hr. The films of uniform thickness were compression molded at 200 ^{o}C under 5-ton pressure using Carver Press (Germany). The thickness of the films was around 0.4 to 0.5 mm.

A.3 Results & Discussion

A.3.1 Dielectric Studies

The frequency dependence of the dielectric properties of PVDF/Fe_3O_4 nanocomposites with various volume fraction of the Fe_3O_4 is shown in Figure A.2 (a) and (b). It can be seen that the dielectric permittivity depends on both frequency and filler loading. The dielectric permittivity for neat PVDF is around 7 and it increases to 38 for 40 wt% of Fe_3O_4 nanoparticles loading. With increasing frequency dielectric permittivity decreases in PVDF and similar trend is followed in nanocomposites. It is worth to note that the dielectric permittivity is increased in the whole frequency range of measurement. The increment in the permittivity in the high frequency region brings the interest of these materials for application in high frequency electronic devices. The high values of permittivity observed in the nanocomposites may be due to the interfacial effects in polymer nanocomposites. For PVDF and nanocomposites up to 30% filler loading, dielectric constant is less dependent on frequency and whereas for 40% loading a strong frequency dependence is seen in the dielectric spectra.

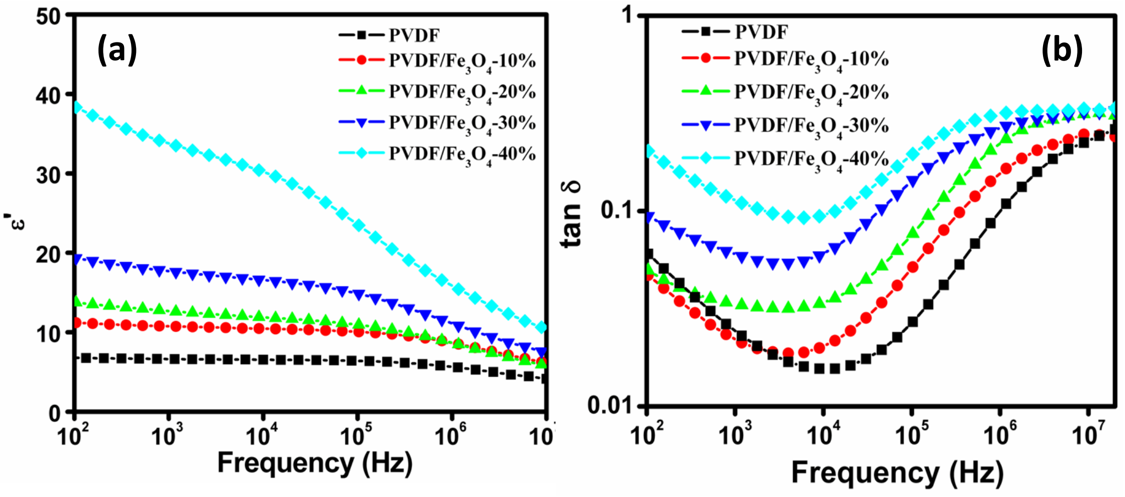

Figure A.2: Frequency dependence of (a) dielectric permittivity (ε') (b) loss (tan δ) of PVDF and PVDF/Fe_3O_4 nanocomposites.

In dielectric permittivity spectra, strong frequency dispersion regions are observed above frequency 10^{+06} Hz and a frequency independent region in between. Hence the dispersion observed in the permittivity originates from the dielectric relaxation processes in polymer nanocomposites. The dielectric dispersion located at $2 \times 10^{+07}$ Hz is attributed to glass transition relaxation.

Figure A.2 (b) shows the variation of loss tangent (tan δ) with frequency for PVDF/Fe_3O_4 nanocomposites at room temperatures. Dielectric loss curve shows broad relaxations corresponding to the glass transition temperature. In PVDF/Fe_3O_4 nanocomposites, glass transition relaxation systematic shifts to lower frequency with increasing filler loading. Moreover, the maximum value of tan δ is less than 0.2 for the entire range of frequencies studied, which is very important for most of dielectric applications.

The variation of the permittivity with filler can be studied using various equations. Log law model is often used to predict the dielectric permittivity of composite systems and is given by following equation,

$$\log \varepsilon'_{composite} = \log \varepsilon'_{matrix} + \varphi_{filler} \log \left(\frac{\varepsilon'_{filler}}{\varepsilon'_{matrix}}\right)$$

This model takes the filler content and the permittivity of constituent materials into account. Figure A.3 shows the variation of dielectric permittivity with filler loading. The solid line is fitting line to the observed data which shows that the data can be best fitted using log law model.

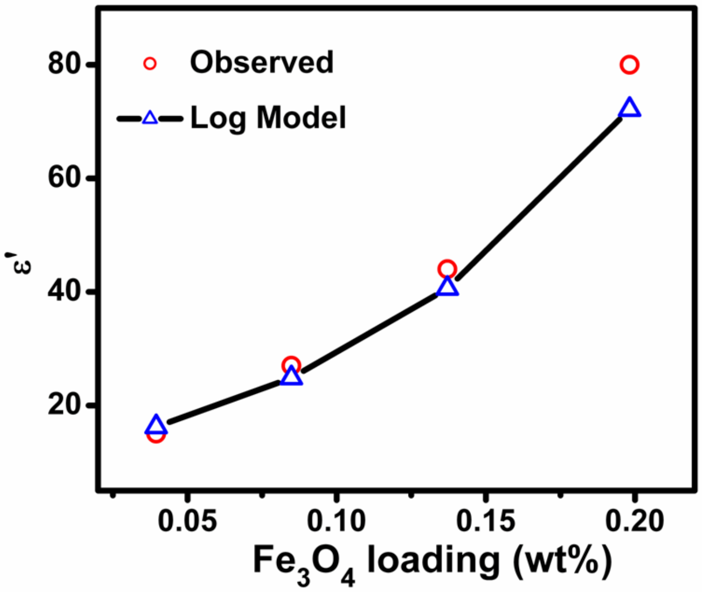

Figure A.3: Fitting of dielectric permittivity data to log model.

A.3.2. Magnetic Properties

Figure A.4 shows the field dependent magnetic properties of PVDF/Fe_3O_4 nanocomposites at 300 °K. The hysteresis loop provides the important information relating to the magnetic properties of the materials viz. saturation magnetization, remnant magnetization and coercivity. M-H hysteresis loop measurements done at 300 °K with the magnetic field swept back and forth between 10 kOe and -10 kOe is shown in figure A.4. The magnetic behavior of PVDF/Fe_3O_4 nanocomposites with different content of Fe_3O_4 nanoparticles shows a clear magnetic hysteresis loops at 300 °K. The observance of hysteresis loop tells that the blocking temperature (T_B) of the sample was higher than the room temperature. The magnetic measurement shows that nanocomposites exhibit ferromagnetic nature of nanoparticles. The variation of the ferromagnetic response was consistent with the varying volume concentration of the nanoparticles. It is observed that the saturation magnetization increases linearly with increasing filler loading which is consistent with the mean field dependence of the magnetization of iron oxide nanoparticles. It can be seen that the coercive field (*Hc*) at 300 °K for different concentrations of Fe_3O_4 in PVDF remains roughly the same as 76 Oe. The saturation magnetization in polymer loaded nanoparticles system is generally expected to be lower than that of the bulk materials.

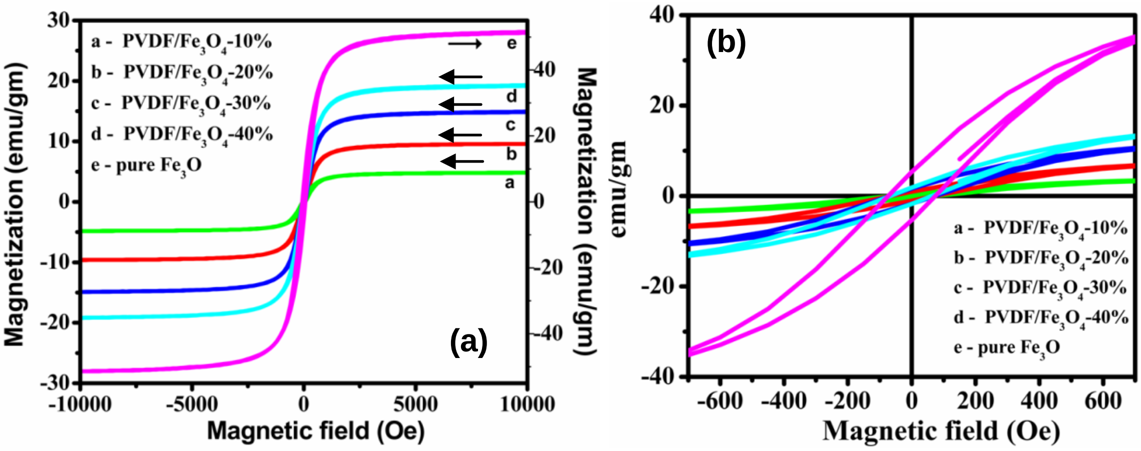

Figure A.4: (a) M-H curves at 300 °K for Fe_3O_4 and PVDF/Fe_3O_4 nanocomposites (arrows indicates towards corresponding Y-axis) (b) Same graph with magnified image.

The magnetic properties can be influenced by the size, structure, and morphologies of the materials. The magnetic parameters extracted from the measurements are summarized in Table I.1. Remnant magnetization also increases with increasing filler content. However this increase observed is non-linear. Unlike saturation magnetization, remenance magnetization is influenced by particle-particle interaction which is governed by the particle concentration inside the polymer matrix.

Composition	Ms (emu/gm)	Coercive field (Hc) (Oe)	Remnant magnetization(M_R) (emu/gm)
Fe_3O_4	50.3	74	5.3
PVDF/Fe_3O_4-10%	4.7	76	0.42
PVDF/Fe_3O_4-20%	9.5	76	1.06
PVDF/Fe_3O_4-30%	14.6	76	1.65
PVDF/Fe_3O_4-40%	18.9	76	1.75

Table I.1: Magnetic measurement results of PVDF/Fe_3O_4 nanocomposites.

A.4 Conclusions

In conclusion, we have studied the dielectric and magnetic properties of melt compounded PVDF/Fe_3O_4 nanocomposites. The nanocomposite shows composition dependent dielectric permittivity and magnetic properties. The dielectric permittivity was found to increase with increasing loading of Fe_3O_4 nanoparticles. The variation of dielectric permittivity with filler loading can be fitted very well using log law model. The magnetic measurement studies show that nanocomposites exhibit ferromagnetic nature of nanoparticles. Thus, the nanocomposites material can be suitable material for electromagnetic shielding (EMI) material application.

A.5 References

1. Jeffrey Pyun, *Polymer Reviews*, **2007**, 47, 231–263.
2. Natalia Frickel, Anna Gutina Greenbaum, Moshe Gottlieb, Annette M. Schmidt, *J. Phys. Chem. C*. **2011**, 115, 10946–10954.
3. K. Devi Chandrasekhar, A. K. Das, A. Venimadhav, *Applied Physics Letters*, **2011**, 98**,** 122908.
4. Masoumeh Bayat, Heejae Yang, Frank Ko, *Polymer,* **2011**, 52, 1645-1653.
5. P. Martins, C.M. Costa, S. Lanceros-Mendez, *Appl. Phys. A.,* **2011**, 103, 233–237.
6. G. H. Qiu, Q. Wang, M. Nie, *Macromol. Mater. Eng.* **2006**, 291, 68.

List of Publications

1. "Enhanced dielectric permittivity in poly (vinylidene) fluoride/multiwalled carbon nanotubes nanocomposite thin films fabricated by pulsed laser deposition", **Chetan Chanmal**, Meenal Deo, Jyoti Jog, *Applied Surface Science,* 2011, 258, 1256– 1260.
2. "Strong electric field modulation of transport in PVDF/MWCNT nanocomposite near the percolation threshold", **Chetan Chanmal**, Meenal Deo, Abhimanyu Rana, Jyoti Jog, Satishchandra Ogale, *Solid State Communications*, 2011, 151, 1612-1615.
3. "Catalyst free novel synthesis of single layer graphene (SLG) and its application in high current O-FET and phototransistor based on P3HT / SLG composite", Prasad Yadav, **Chetan Chanmal**, Aniruddha Basu, Lily Mandal, Jyoti Jog, Satishchandra Ogale, *RSC Advances,*2013,3,18049-18054.
4. "Study of dielectric behavior in PVDF/Clay nanocomposites", **Chetan Chanmal**, Jyoti Jog, *e-Polymers, 2009, no. 112.*
5. "Electrospun PVDF/$BaTiO_3$ nanocomposites: polymorphism and thermal emissivity studies", **Chetan Chanmal**, Jyoti Jog, *Int J Plast .Technol,* 2011, 15, 1-9.
6. "Dielectric relaxations in PVDF/$BaTiO_3$ nanocomposites", **Chetan Chanmal**, Jyoti Jog, *eXPRESS Polymer Letters,* 2008, 2, 294-301.
7. "Magnetic and dielectric properties of polymer-ceramic composites synthesized using a melt compound technique", Rajshree Jotania, **Chetan Chanmal**, Jyoti Jog, *International Journal of Modern Physics: Conference Series,*2013, 22, 552–557.

Invited Book Chapter

1. Chapter title: "Dielectric Relaxation Spectroscopy for Polymer Nanocomposites", **Chetan Chanmal**, Jyoti Jog.
   Book Title: "Characterization Techniques for Polymer Nanocomposites" Publisher- WILEY-VCH. Chapter 7, Page 167-185, 2012.